LBNL-48994

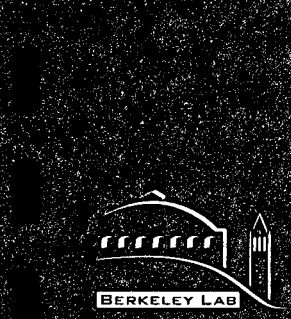

ERNEST ORLANDO LAWRENCE
BERKELEY NATIONAL LABORATORY

Ultra-Low Field Magnetic Resonance Using Optically Pumped Noble Gases and SQUID Detection

Annjoe G. Wong-Foy

Materials Sciences Division

May 2001

Ph.D. Thesis

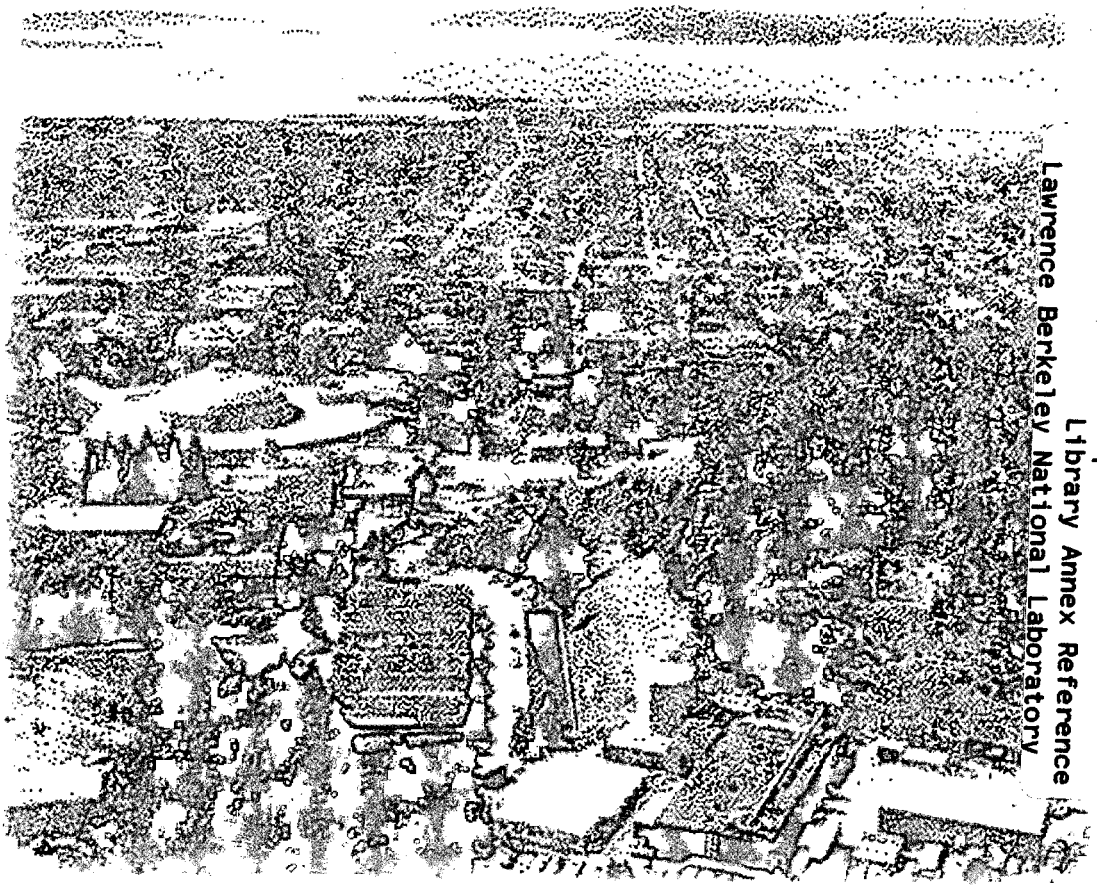

LBNL-48994

Ultra-Low Field Magnetic Resonance Using Optically Pumped Noble Gases and SQUID Detection

Annjoe Golangco Wong-Foy
Ph.D. Thesis

Department of Chemistry
University of California, Berkeley

and

Materials Sciences Division
Ernest Orlando Lawrence Berkeley National Laboratory
University of California
Berkeley, CA 94720

May 2001

This work was supported by the Director, Office of Science, Office of Basic Energy Sciences, Materials Sciences Division, of the U.S. Department of Energy under Contract No. DE-AC03-76SF00098.

Ultra-Low Field Magnetic Resonance using Optically Pumped Noble Gases and SQUID Detection

by

Annjoe Golangco Wong-Foy

A.B. (Harvard University) 1996

A dissertation submitted in partial satisfaction of the
requirements for the degree of
Doctor of Philosophy

in

Chemistry

in the

GRADUATE DIVISION
of the
UNIVERSITY OF CALIFORNIA, BERKELEY

Committee in charge:

Professor Alexander Pines, Chair
Professor Paul A. Alivisatos
Professor Jeffrey A. Reimer

Spring 2001

Ultra-Low Field Magnetic Resonance Using Optically Pumped Noble Gases and SQUID Detection

by

Annjoe Golangco Wong-Foy

Abstract

Ultra-Low Field Magnetic Resonance using Optically Pumped Noble Gases and SQUID Detection

by

Annjoe Golangco Wong-Foy
Doctor of Philosophy in Chemistry

University of California, Berkeley

Professor Alexander Pines, Chair

The focus of the research reported in this dissertation has been the development of instrumentation and techniques for low field, low frequency magnetic resonance. The nuclei in these experiments were subjected to magnetic fields no greater than 25 *Gauss* (2.5 mT). Superconducting magnet technology continually improves, and nuclear magnetic resonance (NMR) moves inexorably from a radiofrequency (*megaHertz*) spectroscopy to a microwave (*gigaHertz*) spectroscopy, but in this body of work, NMR is an audiofrequency (*kiloHertz*) technique.

The main difficulty with low field NMR is the lack of sensitivity, in other words, lack of signal. To combat this situation we have built equipment utilizing *femto-Tesla*-sensitive superconducting quantum interference device (SQUID) magnetic flux detectors, both the higher sensitivity low transition temperature (liquid helium) devices as well as the new cutting edge high transition temperature (liquid nitrogen) SQUIDs. We have exploited the large, non-equilibrium polarizations of optically pumped noble gases, using helium and especially xenon as contrast agents for magnetic resonance imaging (MRI). Our new circular flow optical pumping system provides an effectively *unlimited* source of laser polarized xenon which we have utilized for both MRI and NMR spectroscopy at ultra-low fields. We have achieved mm resolution in the xenon MRI of materials and the first observation at 2.5 mT of the chemical shifts of xenon in different chemical environments.

An appropriate question to ask is why bother with weak magnet NMR? There are strong and very practical reasons why low field NMR, especially low field MRI, is useful and important, and I discuss them in Section 4.2. I will not repeat them here. What I would like to say, since this may be the only chance I will ever have to say it due to the constant pressure on researchers to prove utility of their work in order to gain funding, "We are scientists; we do it because we can."

For my Parents.

Contents

List of Figures

Acknowledgements

I would first like to thank my advisor Professor Alexander Pines for taking me into his group and trusting me with all of his expensive equipment. Alex is not only one of the most brilliant persons I know, he is also one of the most inspiring. I will be lucky if I can take with me from my time in the Pines Group (besides a supercon magnet if it will fit in my car) even a glimmer of Alex's ability to look at a piece of science, distinguish what makes it exciting, and convince others why it is so.

I need to thank our research collaborator Professor John Clarke whose up-to-date technical knowledge regarding SQUIDs has always impressed me; he is one of the only tenured professors I would still trust in a lab. I further want to acknowledge my coworkers from the past five years, starting with the host of post-docs who challenged, motivated, and instructed me when I first started graduate school: Roberto Seydoux, Matt Augustine, Jeff Yarger, and Marco Tomaselli; as well as the graduate students who were the first to "show me the ropes:" Dinh TonThat and Beth Chen; the researchers who I worked with to get the high-T_c SQUID operational: Ricardo de Souza, Klaus Schlenga, and Robert McDermott; and finally the scientists who have helped me with the last leg of the race and get to the finish line: Hans-Marcus Bitter, Adam Moulé, Julie Seeley, and especially the post-doc Sunil Saxena whose friendship and greater wisdom made it easier to get through some of the more trying times. I need to thank all Pinenuts, past and present, whose previous hard work has directly and indirectly made my research successful and my time in Berkeley memorable. I wish to single out Boyd Goodson, David Laws, Fred Salsbury, and Seth Bush who actively recruited me into the group and helped me adjust to my new home two levels below ground. My memories of the group will also always include: Lana Kaiser, Yi-Qiao Song, Eike Brunner, Tom De Swiet, Thomas Meersman, Yung-Ya Lin, David de Graw, Jamie Walls, Maggie Marjanska, Bob Havlin, Bo Blanton, Megan Spence, and John Logan. For the successfulness of the SQUID projects, I am grateful to Tom Lawhead in the glass shop and to Eric Granlund in the machine shop.

I owe a tremendous debt to Dione Carmichael, our group's administrative assistant. Without her facilitation and support, I certainly would not be graduating this May 2001.

The road to graduate school started long before I arrived in Berkeley, and I am indebted to my previous professors and teachers, especially my undergraduate advisor Professor Cynthia Friend who motivated me to pursue a doctoral degree and a career in science. In the Friend group my appreciation goes to James Batteas and Katie Queeney who took a wide-eyed undergrad under their wings. I would be remiss not to mention my secondary school teachers, science as well as non-science, who ignited my enjoyment of learning: Mrs. Peinemann, Mrs. Wisehart, Mr. Teachworth, Mr. Shelburne, and Mr. Vigilante. I blame them for my protracted stay in school.

I owe much gratitude to all of my friends—I would be a hermit without them. Warmest "Thank You's" go to my fellow grad students who encouraged and commiserated with me these past five years: Edward Byrd (who also proofread this dissertation), Brandon Weldon, Liz Juang-Laws, Amy Prieto, Juanita Wickham, Phil Geissler, and Jo Chen. I cannot forget the five who survived Littlejohn's class with me: Joe "Crusher" Walrath, Aaron Burstein, Louis Gascoigne, Jon Sorenson, and again Edward Byrd. Regards are also due to my college chum Greg Ku who, being in an M.D./Ph.D. program, always made me feel better with the knowledge that he would be a student longer than I would. And special thanks go to Kenia Whitehead, my best friend from high school. She is in no small part responsible for my being a research scientist today.

I want to thank my brother for looking out for me all of my life and for all of the advice he has given to me. When I was younger I didn't like that he always "got to do things first," but I appreciate now that his pioneering experiences have made my life better. Finally, my deepest thanks and affection go to my parents for their love, encouragement, and tolerance throughout the years. Any successes that I might claim can be traced back to the care and guidance that they have given to me and to the examples that they have set.

This work was supported by the Director, Office of Science, Office of Basic Energy Sciences, Materials Sciences Division, of the U.S. Department of Energy under Contract No. DE-AC03-76SF00098.

Chapter 1

Basic NMR Theory

1.1 Introduction

This thesis is a record of most of the scientific or engineering accomplishments that I was involved with while in the Pines Group at UC Berkeley. The unifying thread throughout this work was the implementation of Superconducting QUantum Interference Devices (SQUIDs) for low field nuclear magnetic resonance (NMR) and magnetic resonance imaging (MRI). A majority of the work also involved the application of optically pumped xenon to new techniques of low field magnetic resonance.

This first chapter is a short primer on NMR theory for the modern day pulsed nuclear magnetic resonance experiment. Information on continuous wave (CW) procedures will not be found here. My favorite NMR reference is Fukushima's "**Nuts and Bolts**" [1], but other theoretical and in depth texts are also suggested [2, 3, 4, 5, 6, 7, 8]. The second chapter is an introduction to the ideas behind spin-exchange optical pumping. Chapter 3 covers some of the theory that governs SQUID sensors. Finally Chapters 4 and 5 give experimental details and results from the work including the first experiments with low transition temperature SQUIDs up to the most recent work with high transition temperature SQUIDs.

1.2 The NMR Experiment

The idea behind NMR spectroscopy is to "tickle" the nuclear spins of a sample and gain information on parameters such as electronic or molecular structure and dynamics by watching the spin reactions. In the NMR experiment, the sample is placed into a very powerful magnetic field and is allowed to equilibrate. The system is then perturbed by pulsing a second magnetic field oriented perpendicular to the equilibration field. The signal that one detects is the magnetic motion of the nuclear spins as they relax back to equilibrium. Pulsed Electron Spin Resonance (ESR), also called Electron Paramagnetic Resonance (EPR), is studied in exactly the same fashion as pulsed NMR, the difference being the detection of electron spins as opposed to nuclear spins.

1.2.1 The Static Field

A magnetic field will break the isotropy of space and introduce a preferred orientation. NMR active (non-zero spin) nuclei will align in that magnetic field. For the simplest case of spin-1/2 nuclei, the spins can orient parallel to or antiparallel to the magnetic field, and are said to be "spin up" or "spin down." The difference in energy between these two states is known as the Zeeman energy, see Figure 1.1.

$$E_{Zeeman} = |E_{par} - E_{antipar}| = |\mu B_\circ - (-\mu B_\circ)| \tag{1.1}$$

where $B_\circ$ is the static magnetic field, μ is the magnetic moment particular to the nucleus. Note the absolute value due to the fact that μ may be negative. The nuclear magnetic moment is also defined by:

$$\mu = \gamma \hat{I}_z \tag{1.2}$$

γ is the nuclear gyromagnetic ratio and $\hat{I}_z$ is the azimuthal spin angular momentum operator. γ is sometimes defined as:

$$\gamma = \frac{g_n \mu_N}{\hbar} \tag{1.3}$$

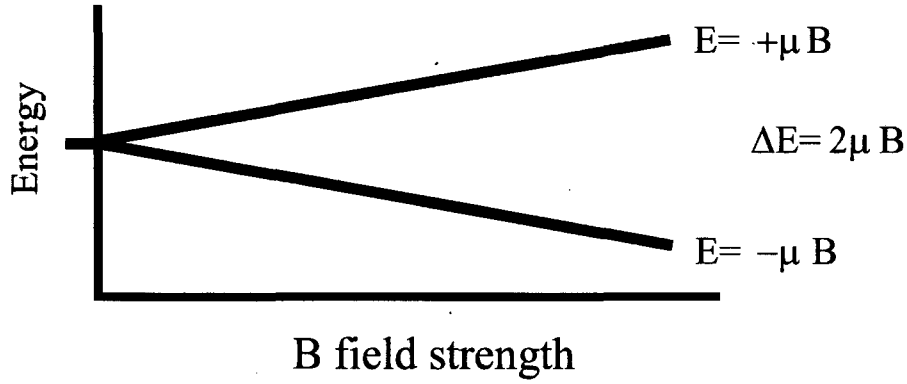

Figure 1.1. Zeeman splitting of the spin energy levels due to the static magnetic field.

where g_n is the g-factor for the particular nucleus and μ_N is the nuclear magneton defined as $\frac{e\hbar}{2m_n} = 5.05 \times 10^{-27}\ Am^2$ where m_n is the rest mass of the neutron. This is analogous to the definition of the electron gyromagnetic ratio from its g-factor and the Bohr magneton $\mu_B = \frac{e\hbar}{2m_e} = 9.27 \times 10^{-24} Am^2$ where m_e is the rest mass of the electron:

$$\gamma_e = \frac{g\mu_B}{\hbar} \tag{1.4}$$

The g-factor for electrons may be calculated from the Dirac Equation, but g_n or γ for all nuclei must be measured experimentally. The two most important nuclei for the work reported here are protons ^{1}H and xenon ^{129}Xe with gyromagnetic ratios $\gamma_H = 26.7520 \times 10^7 \frac{rad}{T \cdot s} = 4.267 \frac{kHz}{G}$ and $\gamma_{Xe} = -7.441 \times 10^7 \frac{rad}{T \cdot s} = -1.187 \frac{kHz}{G}$ respectively. The Larmor frequency is defined as the frequency corresponding to the Zeeman energy

$$\omega_L = \frac{E_{Zeeman}}{\hbar} = \frac{2\mu B_\circ}{\hbar} = \frac{2\gamma \hat{I}_z B_\circ}{\hbar} \tag{1.5}$$

which for spin-1/2 nuclei is simply

$$\omega_L = \frac{2\gamma(\frac{1}{2}\hbar)B_\circ}{\hbar} = \gamma B_\circ \tag{1.6}$$

Since one spin state is higher in energy than the other (for spin-1/2 nuclei), one would expect an unequal distribution of spins in the two states. Simple Boltzmann statistics determine the relative populations of the two energy levels. Assuming

that the spin parallel to the field is the lower energy state:

$$N_{anti} = N_{para} \cdot e^{-2\mu B_o/k_B T} \tag{1.7}$$

Polarization is then defined as the normalized differece in the spin populations:

$$P = \frac{N_{para} - N_{anti}}{N_{para} + N_{anti}} = tanh\left(\frac{\mu B_o}{k_B T}\right) \tag{1.8}$$

Due to the (albeit small) difference in populations, there is a net magnetic moment due to the nuclear spins. It is the sum of all the nuclear moments:

$$M = \mu P N_{Tot} \tag{1.9}$$

where μ is again the nuclear moment, P is defined above and N_{Tot} is the total number of nuclei. Polarizations and therefore magnetic moments are very small. The protons in water at room temperature in a magnetic field of 1 $Tesla$ (T) have a polarization of only 10^{-5}, so the induced magnetic moment is very tiny. One of the reasons why NMR spectroscopists continually try to get stronger and stronger magnets is to increase the polarization and therefore increase the NMR signal.

1.2.2 The Pulse Field

In the two level picture described above, it is easy to imagine performing spectroscopy by causing transitions between the two energy levels, and it is indeed this energy difference that NMR probes. Similar to most light absorption spectroscopies, continuous wave NMR measures the decrease in applied radiation due to absorption by the sample. Modern Fourier Transform (pulsed) NMR measures, instead, the nuclear spin relaxation subsequent to excitation by radiation. In terms of the two-level picture, the quantity that is detected in an experiment is the radiation of the excited spins as they relax from the higher energy level back to the lower energy level until equilibrium. Clearly the strength of the signal is dependent on the size of the magnetic moment induced by the static field.

In order to excite the nuclei in the first place, an oscillating magnetic field with a frequency corresponding to the energy splitting, in other words the Larmor frequency, must be applied to the sample. This is done with coils that create

a field perpendicular to the static field. For NMR experiments done in static fields upwards of 10 mT, which is the majority of NMR experiments, the Larmor frequencies are in the megahertz, so NMR is sometimes referred to as radiofrequency spectroscopy. Since I worked with static fields smaller than 10 mT, all of the experiments that I conducted employed much lower frequency audiofrequency (kilohertz) pulses. The excitation coil is usually part of a circuit that is tuned to the appropriate Larmor frequency. Using such a tuned resistor-inductor-capacitor (RLC) "tank" circuit improves the power deposition to the sample. It also increases the detection sensitivity since the excitation coil serves as the detection coil in most high field experiments.

1.2.3 The NMR Signal

The form of the NMR signal is a free induction decay (FID) typically shaped like a sine wave oscillating at the Larmor frequency and damped with an exponential decay envelope. It is easiest to explain the output in terms of a classical picture. This picture starts with the net nuclear magnetic moment induced by the static field; at equilibrium it is aligned parallel or antiparallel to the static field. Then the system is perturbed by an second magnetic field. In the quantum mechanical picture it is clear that the excitation field must oscillate, but to see why in the classical picture the field B_1 must oscillate at the Larmor frequency, first consider an excitation field B_1 that is static. Switching on the field B_1 aligned perpendicular to the static field $B_\circ$ will cause a torque $\mu_{net} \times \vec{B}_1$ and the moment will "tip" away from equilibrium. Immediately it will precess due to the torque $\mu_{net} \times (\vec{B}_\circ + \vec{B}_1)$. However unless the strength of $\vec{B}_1$ is of the same order as the strength of the static field, the tipping angle of μ_{net} away from the $\vec{B}_\circ$ axis will be small. To create large perturbations the field $\vec{B}_1$ must be on resonance with the precession of the moment; in other words, the field $\vec{B}_1$ should rotate at the same frequency as the precession frequency of the magnetic moment. From the perspective of the moment μ_{net} precessing at the Larmor frequency, the magnetic field $\vec{B}_1$ rotating at the same frequency looks static. So it efficiently tips the magnetization. The tipping angle

of the moment relative to B_o is dependent on the amplitude of B_1 and the length of the time that B_1 is turned on. A 90° or $\pi/2$ pulse will tip the magnetization from equilibrium (say the z direction) completely to the transverse (x-y) plane. This can be done with a hard pulse: high magnetic field amplitude and short duration or with a soft pulse: smaller field magnitude and longer duration. After the pulse, the net nuclear moment continues to precess (at the Larmor frequency) as it relaxes back to equilibrium. The damped, rotating magnetization induces a current in the detection coil by Faraday's law of induction.

The set of classical equations that describe the behavior of the magnetization in an NMR experiment during the pulse are the Bloch equations:

$$\frac{dM_x}{dt} = \gamma M_y B_o + \gamma M_z B_1 sin(\omega t) - \frac{M_x}{T_2} \quad (1.10)$$

$$\frac{dM_y}{dt} = -\gamma M_x B_o + \gamma M_z B_1 cos(\omega t) - \frac{M_y}{T_2} \quad (1.11)$$

$$\frac{dM_z}{dt} = -\gamma M_x B_1 sin\omega t - \gamma M_y B_1 cos(\omega t) - \frac{M_z - M_o}{T_1} \quad (1.12)$$

$M_{x,y,z}$ are the components of magnetization in each of the Cartesian directions, M_o is the initial magnetization, γ is the nuclear gyromagnetic ratio, and B_o and B_1 are the magnitudes of the static field and pulse field respectively. T_1 and T_2 are important time constants that describe the relaxation of the magnetization to equilibrium. T_1 is the longitudinal or spin-lattice relaxation time and is the characteristic time at which the z-component of the magnetization will return to its full (equilibrium) value. T_2 is the transverse or spin-spin relaxation time. It measures the time for the transverse (x-y) components of the magnetization to return to their equilibrium values of zero. In the free induction decay, T_2 determines the shape (time constant) of the exponential decay envelope. More accurately, the time constant of the exponential decay envelope gives T_2^*, which is the transverse relaxation time but also includes apparent shortening of the transverse magnetization due to dephasing of all the little nuclear moments caused by effects like field inhomogeneities. After the pulse is turned off the components of magnetization will follow these simpler equations:

$$\frac{dM_x}{dt} = -\frac{M_x}{T_2} \tag{1.13}$$

$$\frac{dM_y}{dt} = -\frac{M_y}{T_2} \tag{1.14}$$

$$\frac{dM_z}{dt} = -\frac{M_z - M_o}{T_1} \tag{1.15}$$

As was mentioned earlier, the signal detected in the coil takes the form of a damped sinusoid. The mathematical form of the FID is given by:

$$M_{x,y}(t) = M_o e^{i\omega_o t} e^{\frac{-t}{T_2}} \tag{1.16}$$

Note the decay constant T_2. The Fourier Transform of the free induction decay in the time domain will give the frequency domain NMR spectrum:

$$F(\omega) = \int M(t) e^{i\omega t} dt \tag{1.17}$$

To reconcile the two-level "spin up" versus "spin down" picture with the fact that the coils detect an actual macroscopic transverse magnetization, it is important to remember that "spin up" and "spin down" do not mean that the individual nuclear spin moments point straight up or straight down. It means that the projection of the spin angular momentum on the z-axis (up-down) is either $\hbar/2$ or $-\hbar/2$. We have no certain information about the x or y (transverse) directions. A density matrix calculation would be necessary to treat the system completely quantum mechanically and predict the FID.

1.3 Non-Applied Fields and Interactions

There are a number of interactions and local magnetic fields that nuclei may experience in addition to the fields that are externally applied. These interactions are in fact what make NMR such a powerful tool, and I will briefly desribe these interactions. The basic interactions that everyone should understand are the chemical shift, the dipolar coupling, the j-coupling, and the quadrupolar coupling.

1.3.1 Chemical Shift

The chemical shift is a small shift in the resonance frequency of nuclei due to the local magnetic fields generated by the interaction of the surrounding electrons with the applied magnetic field. By Lenz's law, applying a magnetic field to the electrons will cause them to move (circulate if possible) in such a way as to counteract the applied field. Since the electrons try to generate local fields opposite to the applied field, nuclei are typically shielded—they feel slightly less of the static field. Nuclei in the vicinity of high electron density are shielded more. However, it is possible that in certain molecular configurations, nuclei find themselves in regions where the electron movement has served to increase the magnetic field. In this case the nuclei are said to be deshielded. Chemical shifts are typically small, measured in parts per million (ppm) with respect to the Larmor frequency. They are generally non-isotropic, although in liquids the rapid motion of molecules averages the interactions, so that it appears isotropic. The most general mathematical form of the chemical shift Hamiltonian is:

$$\mathcal{H}_{CS} = \gamma \hat{I} \cdot \tilde{\sigma} \cdot \vec{B}_{\circ} \tag{1.18}$$

where $\hat{I}$ is the nuclear spin operator, $\tilde{\sigma}$ is the second-rank chemical shielding tensor, and $\vec{B}_{\circ}$ is the static magnetic field.

1.3.2 Dipolar Coupling

Dipolar coupling is the nucleus-nucleus interaction based on the magnetostatic case of one magnetic dipole directly interacting through-space with another dipole. The full Hamiltonian for dipolar coupling is:

$$\mathcal{H}_D = \frac{\gamma_1 \gamma_2 \hbar^2}{r_{12}^3} \left(\hat{I}_1 \cdot \hat{I}_2 - \frac{3(\hat{I}_1 \cdot \vec{r})(\hat{I}_2 \cdot \vec{r})}{r_{12}^2} \right) \tag{1.19}$$

where the subscripts refer to the nuclei, $\hat{I}$ are the spin operators, and $\vec{r}$ is the spatial vector joining the two nuclei. The Hamiltonian can also be expanded to give the famous dipolar alphabet:

$$\mathcal{H}_D = \frac{\gamma_1\gamma_2\hbar^2}{r_{12}^3}(A+B+C+D+E+F) \quad (1.20)$$

$$A = I_{1z}I_{2z}(1-3cos^2\theta) \quad (1.21)$$

$$B = -\frac{1}{4}(\hat{I}_1^+\hat{I}_2^- + \hat{I}_1^-\hat{I}_2^+)(1-3cos^2\theta) \quad (1.22)$$

$$C = -\frac{3}{2}(I_{1z}\hat{I}_2^+ + \hat{I}_1^+I_{2z})sin\theta cos\theta e^{-i\phi} \quad (1.23)$$

$$D = -\frac{3}{2}(I_{1z}\hat{I}_2^- + \hat{I}_1^-I_{2z})sin\theta cos\theta e^{i\phi} \quad (1.24)$$

$$E = -\frac{3}{4}\hat{I}_1^+\hat{I}_2^+ sin^2\theta e^{-2i\phi} \quad (1.25)$$

$$F = -\frac{3}{4}\hat{I}_1^-\hat{I}_2^- sin^2\theta e^{2i\phi} \quad (1.26)$$

Notice the dependence on the angle θ which corresponds to the angle between the internuclear vector and the static magnetic field vector. In liquids and gases the rapid tumbling of the atoms or molecules averages θ over all orientations and the dipolar coupling vanishes. In solids, however, this is usually not the case, but the averaging can be mimicked by a technique known as Magic Angle Spinning (MAS). I will not discuss MAS, but information on the theory and practice can be found in the references cited at the beginning of this chapter as well as any number of theses from the Pines Group.

1.3.3 J-Coupling

J-coupling is also a nucleus-nucleus interaction that is an electron-mediated through-bond coupling. The j-coupling is responsible for the well-known multiplets in liquid state NMR, e.g. proton lines split by other chemically distinct protons bonded nearby in the molecule. A simple physical picture of how one nucleus can "feel" another through the electrons in a bond is to consider a nucleus with a spin in the state $m_s = \frac{\hbar}{2}$. There are two electrons in each chemical bond, and the electron with the parallel spin moment is likely to spend more time at that nucleus since that is a lower energy configuration than for the antiparallel moment to stay nearby. This means that the other electron of the chemical bond will

spend more time at the second nucleus. If that nucleus is also in the $m_s = \frac{\hbar}{2}$ spin state like the first nucleus, its energy will be raised (relative to non j-coupled frequency) due to the interaction with the antiparallel electron. Accordingly, if the second nucleus was in the $m_s = -\frac{\hbar}{2}$ spin state, its energy would be lowered by the electron interaction.

1.3.4 Quadrupolar Coupling

Quadrupole coupling is the interaction of a quadrupolar nucleus with an electric field gradient (EFG). It can be shown from quantum mechanics that parity considerations require that quadrupoles are necessarily electric rather than magnetic in nature. Therefore their interactions are also electric. A nucleus with a spin ≥ 1 can have a quadrupole moment and will have one if its shape is non-spherical. The first example of a quadrupolar nucleus from the periodic table is deuterium. It has a nuclear spin I=1, and with one proton and one neutron is obviously non-spherical. An electric field gradient (non-uniform electric field) will interact with the non-spherically symmetric quadrupolar nucleus. The gradient can arise from electronic distributions within a molecule or crystal, and the resulting interaction can be very large—up to a couple hundred megaHertz. The best review on Nuclear Quadrupole Resonance (NQR) theory remains the Das and Hahn Solid State Physics Supplement from 1958 [3]. Using their notation below, the most general form of the quadrupole interaction Hamiltonian is:

$$\mathcal{H}_Q = \tilde{Q} \cdot \vec{\nabla} \tilde{E} \tag{1.27}$$

This is derived from the electrostatic Hamiltonian:

$$\mathcal{H} = \int \rho(\vec{x}) V(\vec{x}) d^3\vec{x} \tag{1.28}$$

where $\vec{x}$ = position vector, $\rho(\vec{x})$ = distribution of positive charge in the nucleus, and $V(\vec{x})$ = electrostatic potential. After a power series expansion:

$$\mathcal{H} = \int (d^3\vec{x})\rho(\vec{x}) \left[V(0) + \sum_j \left(\frac{\partial V}{\partial x_j} \right)_0 \cdot x_j + \frac{1}{2} \sum_{j,k} \left(\frac{\partial^2 V}{\partial x_j \partial x_k} \right)_0 \cdot x_j x_k + \ldots \right] \tag{1.29}$$

$$\mathcal{H} = \underbrace{\int (d^3\vec{x})\rho(\vec{x})}_{Ze:charge} \cdot V_0 + \Sigma_j \underbrace{\left[\int (d^3\vec{x})\rho(\vec{x}) x_j \right]}_{P_j:dipole\ moment} \cdot \left(\tfrac{\partial V}{\partial x_j} \right)_0 + \frac{1}{2} \Sigma_{j,k} \underbrace{\left[\int (d^3\vec{x})\rho(\vec{x}) x_j x_k \right]}_{Q_{jk}:quadrupole\ moment} \cdot \left(\tfrac{\partial^2 V}{\partial x_j \partial x_k} \right)_0 \tag{1.30}$$

The terms are arranged in Equation 1.30 to highlight the different electrostatic quantities: charge, dipole moment, and quadrupole moment. Remembering that $\vec{E} = -\vec{\nabla}V$ it is easy to see that the quadrupole moment interacts with an electric field gradient.

1.4 Applied Gradient Fields: Imaging Basics

In 1972 Lauterbur demonstrated the first use of NMR as an imaging tool [9]. In the same vein Mansfield and Grannell independently showed the relationship between NMR signal and nuclear density of samples in a field gradient [10]. The best reference on the theory and use of magnetic resonance imaging is probably Callaghan's book **Principles of Nuclear Magnetic Resonance Microscopy** [11]. Other good references, especially regarding the use of MRI in medicine, can be found in [12, 13, 14, 15, 16, 17, 18, 19, 20, 21, 22, 23] to name a handful.

The principle idea behind NMR imaging, dubbed magnetic resonance imaging (MRI), is that information on the spatial distribution of NMR active nuclei in a subject can be gained by applying different magnetic fields to different areas of the sample. The most obvious pattern of magnetic field is a simple linear gradient in one of the Cartesian directions. A gradient $G = \frac{dB_z}{dx}$ means that the z-component of the magnetic field (usually the static field $B_\circ$) varies in magnitude along the x direction. Armed with two pieces of knowledge: first, the resonance frequency

of a given type of nucleus depends on the static field that it feels (neglecting chemical shift and other interactions) and second, the amplitude of the NMR signal is directly proportional to the number of nuclei, it is easy to see that a linear magnetic field gradient will disperse the NMR spectrum (in frequency space) according to the nuclei concentrations distributed in that gradient. Figure 1.2 shows a number of examples of this 1-D imaging. On the left are the cross sections of various NMR tubes or samples. The right shows the corresponding MRI spectra for a linear gradient. The spectra are shaped like projections onto one dimension (or histograms) of the sample shapes.

The mathematical formulation of this effect begins with the now spatially dependent resonance frequency [11]:

$$\omega(\vec{r}) = \gamma \cdot (B_\circ + \vec{G} \cdot \vec{r}) \tag{1.31}$$

where γ is the gyromagnetic ratio, $B_\circ$ is the magnitude of the static field (assumed in the z directon), $\vec{r}$ is the spatial vector, and $\vec{G}$ is the generalized gradient of the static field:

$$\vec{G} = \vec{\nabla}(B_\circ) = \frac{dB_z}{dx}\hat{x} + \frac{dB_z}{dy}\hat{y} + \frac{dB_z}{dz}\hat{z} \tag{1.32}$$

Next we need to consider the now spatially dependent signal from a sample. Neglecting the relaxation, the normalized signal from a tiny volume element dV is

$$dS = \rho(\vec{r})e^{i\omega(\vec{r})t}dV = \rho(\vec{r})e^{i\gamma\cdot(B_\circ+\vec{G}\cdot\vec{r})t}dV \tag{1.33}$$

where $\rho(\vec{r})$ is the spatially dependent number density of nuclear spins. Integrating over all space and choosing $\gamma B_\circ$ as the reference frequency (in other words mixing down the signal at the Larmor frequency) we obtain:

$$S(\vec{G}, t) = \int \rho(\vec{r})e^{i\gamma(\vec{G}\cdot\vec{r})t}dV \tag{1.34}$$

This expression is reminiscent of a Fourier Transform, and we can in fact define a reciprocal vector $\vec{k}$:

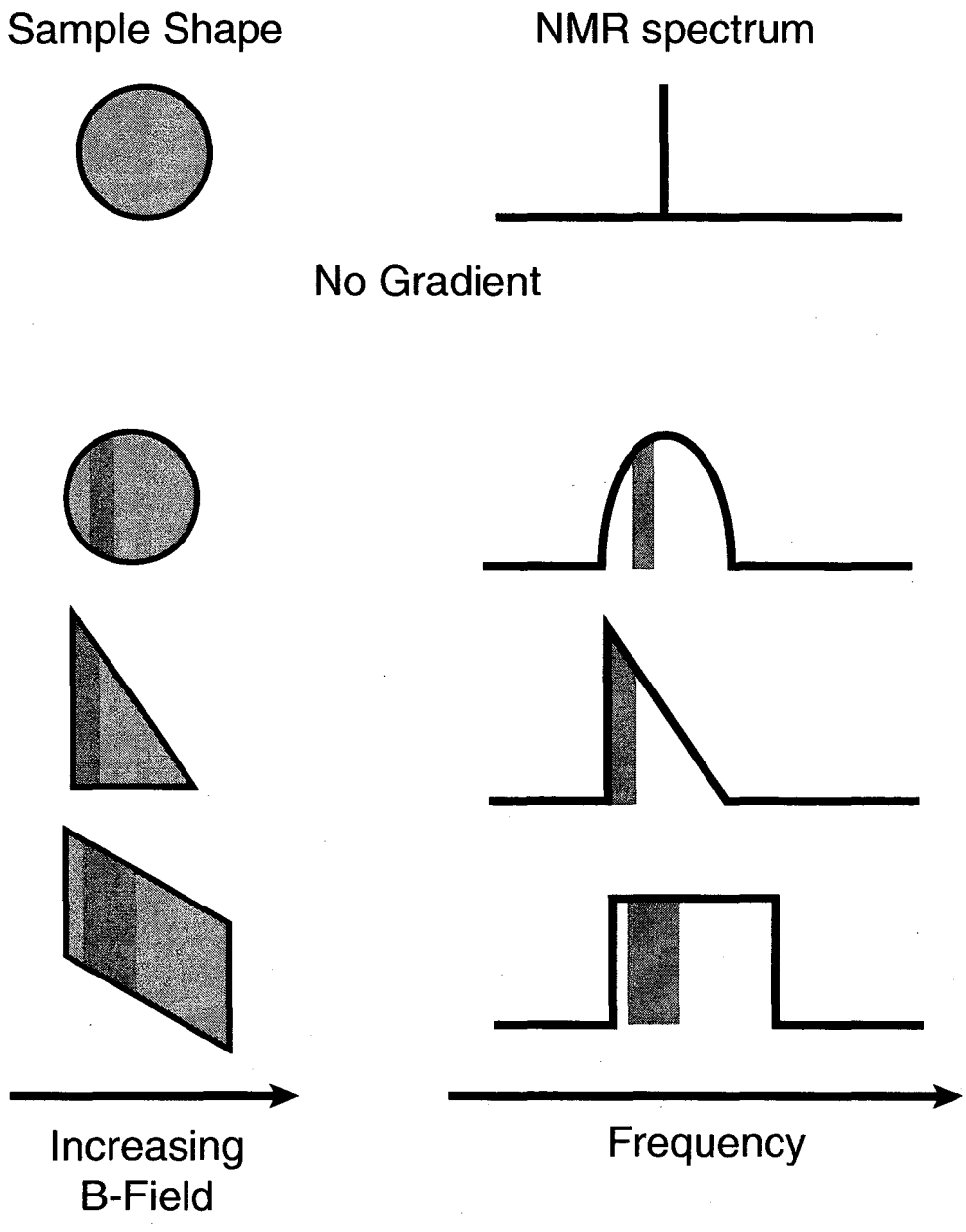

Figure 1.2. Shapes on the left are cross sections of sample tubes. Spectra on the right are the corresponding 1-D projections.

$$\vec{k} = \frac{\gamma \vec{G} t}{2\pi} \tag{1.35}$$

Our signal now becomes

$$S(\vec{k}) = \int \rho(\vec{r}) e^{i2\pi(\vec{k}\cdot\vec{r})t} dV \tag{1.36}$$

Which very conveniently means that we can recover the spatial spin density by a simple Fourier Transform of the signal

$$\rho(\vec{r}) = \int S(\vec{k}) e^{-i2\pi(\vec{k}\cdot\vec{r})t} d\vec{k} \tag{1.37}$$

In order to recover the spatial information of the spin density, it is necessary to traverse the k space. Consider only a single gradient, say $\vec{G} = \frac{dB_z}{dx}$. Referring to Equation 1.35, either the gradient amplitude or time can be incremented in order to step through the $\vec{k}$ space, which is one dimensional since there is only a single gradient. Keeping the gradient fixed and incrementing time amounts to collecting the NMR signal (FID) while the gradient is turned on. This modality is known as frequency encoding. Figure 1.3 shows the simplest frequency encoding pulse sequence where the gradient is constantly on and a simple one pulse NMR scan is run. "RF" stands for radiofrequency and signifies the excitation pulse; "G_x" is the gradient; and "ACQ" is acquisition.

Incrementing the gradient while keeping time fixed is known as phase encoding. The pulse sequences for a phase encoding image experiment are shown in Figure 1.4. In this mode a series of experiments are required. The gradient is turned on for a fixed amount of time and the signal is collected once the gradient is shut off. Then the gradient is increased and pulsed for the same amount of time followed by signal collection. Due to the construction of most spectrometers, the full FID is collected; however, the only necessary piece of information from each data collection is the initial point of the FID. The Fourier transform of the set of these initial points generates the 1-D image. One method of two-dimensional imaging (Fourier imaging) employs both frequency and phase encoding while another known as projection reconstruction uses only frequency. Both of these methods will be discussed

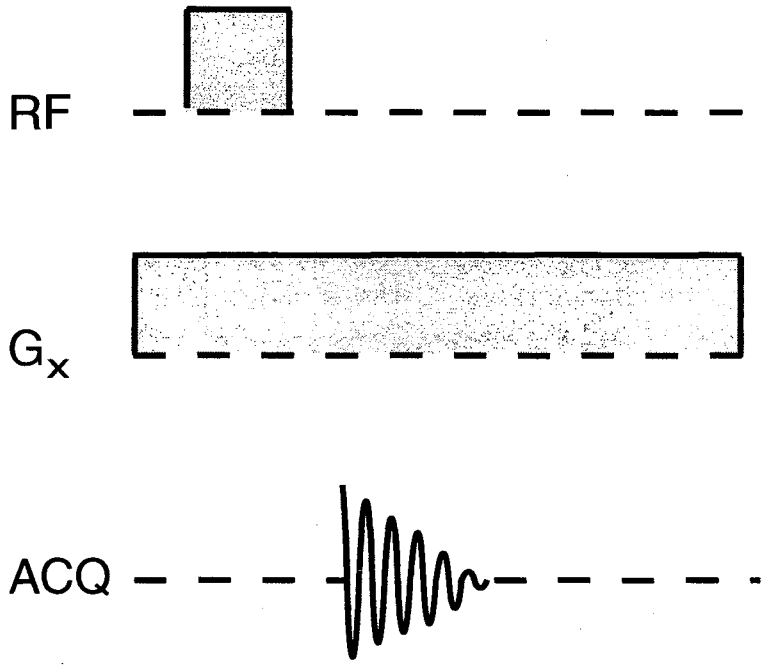

Figure 1.3. Frequency encoding pulse sequence

in later experimental sections, as appropriate.

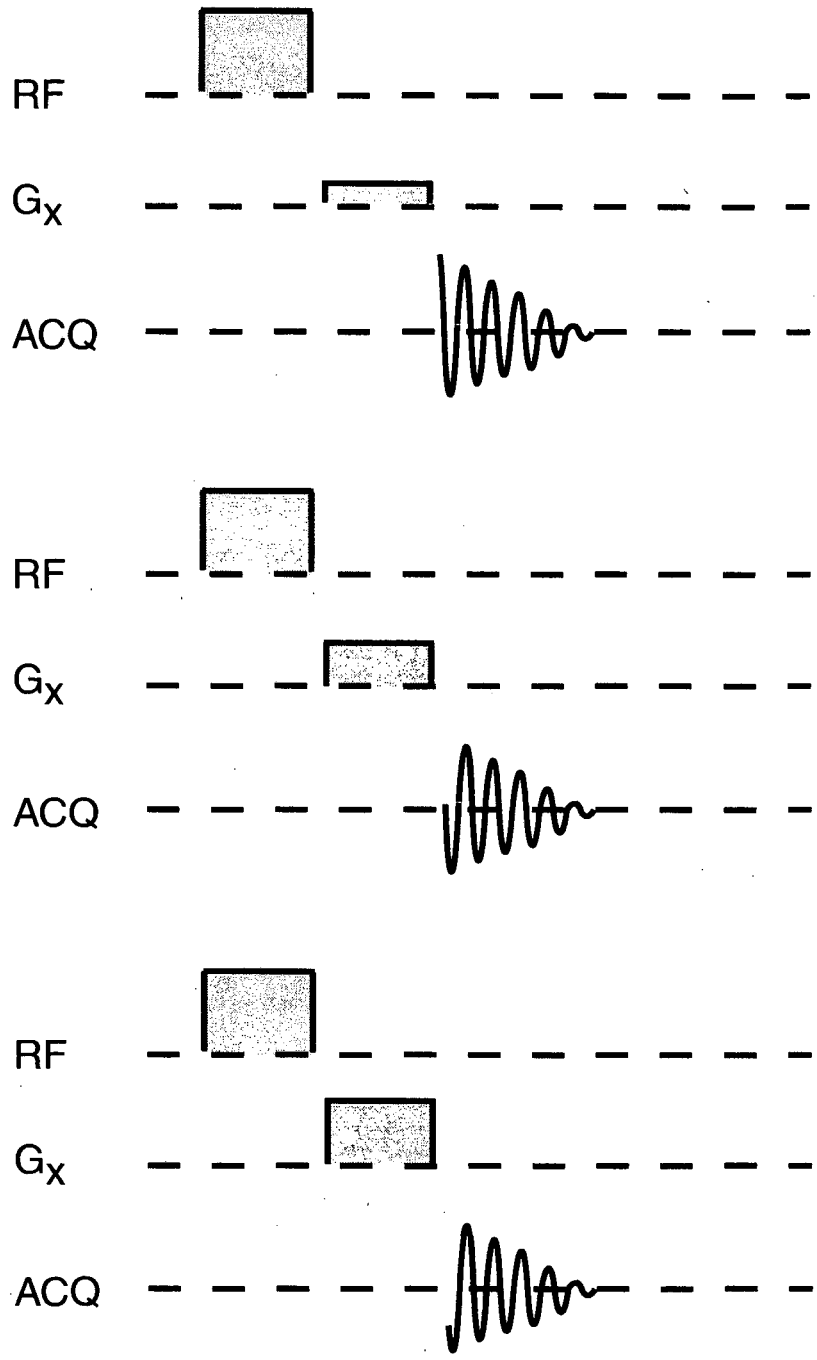

Figure 1.4. Phase encoding pulse sequences

Chapter 2

Optical Pumping

2.1 Introduction

The strength of NMR spectroscopy lies in the incredible amount of chemical and physical information that one can obtain about a system by studying the various interactions mentioned previously in Section 1.3. NMR is a powerful tool for the study of structure and dynamics, especially for liquid systems and non-crystalline solid systems. However, the biggest problem with NMR is the low sensitivity (small signals). The size of the net nuclear moment is the inherent sensitivity or cross section for NMR spectroscopy. Recalling the size of the induced moment given in Equations 1.9 and 1.8, there are a number of things that can be done in order to increase the moment: increase the number of nuclei (more sample), decrease the temperature, or increase the magnetic field. However, there are problems with each of these methods: more sample isn't always possible (such as cases of rare proteins); most NMR spectroscopists work with liquid samples, which if frozen to the solid state would disallow many of the high resolution liquid state NMR approaches and force them to use solid state NMR techniques. Use of a stronger magnet is perhaps the most obvious and most generally applicable strategy; unfortunately, the bigger the magnet, the higher the cost.

An important fact to note, however, is that the magnetic moment as calculated earlier is the thermal equilibrium induced moment. One could imagine preparing

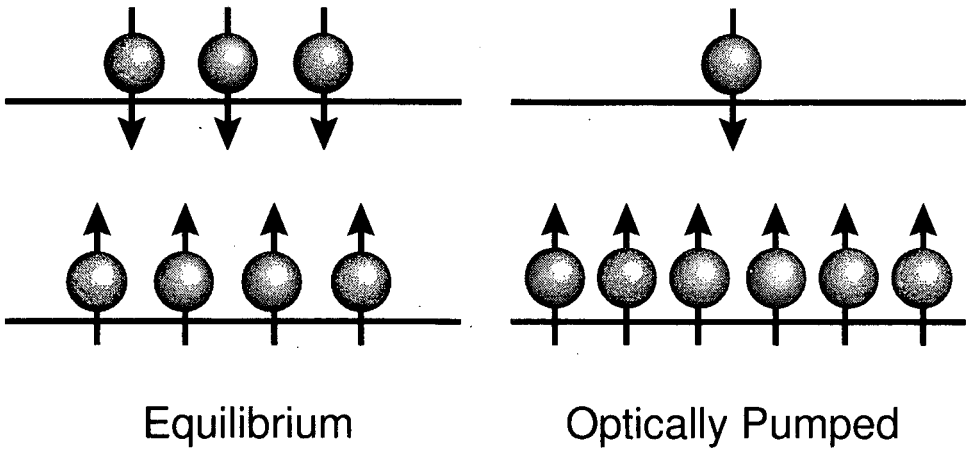

Figure 2.1. Cartoon of spin polarization at thermal equilibrium in a magnetic field versus polarization after optical pumping.

a non-equilibrium state so long as it would last long enough to take NMR spectra. Noble gases can have long spin relaxation times on the order of minutes or hours [24], which could be exploited for creating long lasting, highly non-equilibrium situations. The non-equilibrium states can be created by optical pumping. Figure 2.1 shows a cartoon of the optically pumped versus thermal equilibrium spin states.

Optical pumping (OP) is the general technique of using circularly polarized light to create a non-equilibrium distribution of spins up versus spins down. The effect was first described in 1950 by Kastler [25] who subsequently demonstrated the method of "pompage optique" to generate large electron and nuclear polarizations [26, 27, 28, 29]. He eventually won the 1966 Nobel Prize in Physics for this development. A good deal of research during the 1960's focused on understanding and lengthening the electronic polarization relaxation rates (to equilibrium) of various optically polarized alkali metals, especially rubidium [30, 31, 32, 33, 34]. Various buffer gases were used, including nitrogen and the noble gases. In 1960 Bouchiat, Carver, and Varnum discovered that their helium-3 buffer gas gained a nuclear polarization from the rubidium [35]. Eighteen years later Grover was successful in using optically pumped rubidium to enhance the nuclear polarizations of ^{3}He, ^{21}Ne, ^{83}Kr, ^{129}Xe, and ^{131}Xe [36]. This process known as spin-exchange opti-

cal pumping has gained popularity in recent years for preparing samples of helium and xenon with large nuclear polarizations. Reviews of some of the applications for optically pumped nobled gases can be found in references [37, 38, 39, 40].

2.2 Spin-Exchange Optical Pumping of Noble Gases

The lighter noble gases ^{3}He and ^{21}Ne can be optically polarized by a method known as metastability exchange [41, 42, 43, 44], but no such method yet exists for the heavier noble gases like xenon. Spin exchange with optically pumped rubidium, however, is possible and fairly efficient [36]. As a side note, other nuclear spin systems can be optically pumped directly such as composite semiconductors [45, 46, 47, 48, 49]. The hyperpolarization of the noble gases via spin-exchange optical pumping is a two step process: first is the optical pumping of rubidium to create a large electronic polarization and second is the spin flip-flop between the rubidium electron and the noble gas nuclear spin. One pathway of relaxation for the rubidium is spin transfer to the noble gas nuclei, which retain their polarization much longer than the electronic state of the rubidium.

2.2.1 Rubidium Optical Pumping

Figure 2.2 shows two simplified energy level diagrams of the valence electron of rubidium in a weak magnetic field. Naturally abundant rubidium is a mixture of 72.12% ^{85}Rb with a nuclear spin I=5/2 and 27.85% ^{87}Rb which has a spin I=3/2. Nevertheless, neither the hyperfine splittings nor the difference between ^{85}Rb and ^{87}Rb are explicitly shown in 2.2 because the energy range due to the splittings is only 28 μeV = 0.23 cm^{-1} and for pressures above 100 *torr* (which is always true for our work), pressure broadening smears and mixes the levels [50, 51] into small energy bands which are represented by the block energy levels in the diagram. The selection rules for the absorption of light (allowed electric dipole transition) require that the orbital angular momentum change by one quantum, $\Delta m_\ell = \pm 1$. The change in quantum number of the spin angular momentum is dependent on

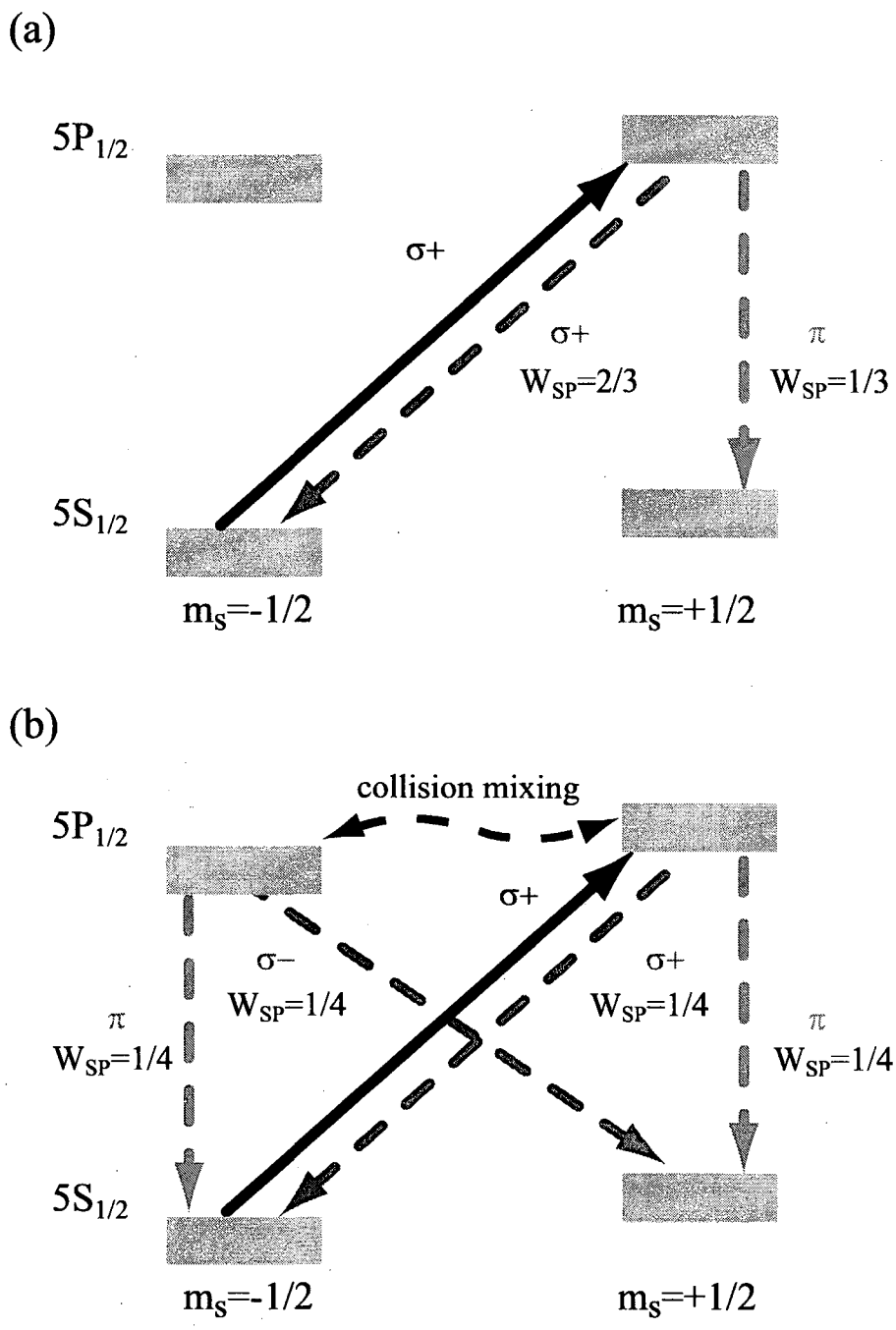

Figure 2.2. (a) Optical Pumping of Rb valence electron in a small magnetic field with no collisional mixing. (b) Optical pumping of Rb with collisional mixing.

the polarization of incoming light. Linearly polarized light, π, does not change the spin quantum state of the electron, but right circularly polarized light, σ^+, has the selection rule $\Delta m_s = +1$, while left circularly polarized light, σ^-, lowers angular momentum, $\Delta m_s = -1$. Since electrons are spin-1/2 particles, only those with $m_s = -\frac{1}{2}$ can interact with σ^+ light.

The branching ratio (W_{SP}) for spontaneous emission from the $^2P_{1/2}$, $m_s = +1/2$ level is 2/3 back to the $^2S_{1/2}$, $m_s = -1/2$, and 1/3 straight down to the $^2S_{1/2}$, $m_s = +1/2$ state. The lifetime of the S state can be as long as many seconds [51], so a large population difference in magnetic substates can develop. For higher gas pressures, collisions can mix the magnetic substates, Figure 2.2 (b). Note that the ground state sublevels are not shown to mix because the symmetric S orbitals are much more stable than the P states. The branching ratios are 1/4 from each P state to both S states. The wavelength of light needed to excite the shown electronic transition is 794.7 nm in the near infrared, just below the visible portion of the electromagnetic spectrum. This wavelength is easily available from Ti-Sapphire lasers as well as the new solid state diode lasers. The $P_{3/2}$ state is 15 nm = 667 $\times 10^3$ cm^{-1} higher in energy than the $P_{1/2}$, so transitions to it are not made with the lasers we use.

2.2.2 Spin Exchange

The optical pumping described in the preceding section creates a large electronic spin polarization of the valence electron of the rubidium. To make this useful for NMR this polarization must be transferred to the nuclei of noble gases during collisions. Herman (1965) was the first to present the theory of spin exchange to explain the transfer of polarization [32]. The Hamiltonian he used to describe the hyperfine interactions is:

$$H = -2g_n\mu_n\mu_\beta \sum_{i=1}^{n} \left(\underbrace{\frac{\vec{I}\cdot\vec{S}_i}{r_i^3} - 3\frac{(\vec{I}\cdot\vec{r}_i)(\vec{S}_i\cdot\vec{r}_i)}{r_i^5}}_{polar\ interaction} - \underbrace{\frac{8\pi}{3}\delta(\vec{r}_i)\vec{I}\cdot\vec{S}_i}_{scalar\ interaction} \right) \tag{2.1}$$

where g_n is the nuclear gyromagnetic ratio, μ_n is the nuclear magneton, and μ_β is the Bohr magneton. $\vec{I}$ is the noble gas nuclear spin, $\vec{S}_i$ is the ith electronic spin where $\vec{S}_1$ is the spin of the rubidium valence electron and $\vec{S}_{2...n}$ are the spins of the noble gas electrons, $\vec{r}_i$ is the radius vector from the noble gas nucleus to electronic spin i. $\delta(\vec{r}_i)$ is a Dirac delta function of the position vector. Herman calculated that the polar interaction (dipole-dipole vector interaction) was unimportant compared to the scalar (Fermi contact) interaction. So the important term can be written as:

$$H = \frac{16\pi}{3} g_n \mu_n \mu_\beta \delta(\vec{r}_i) \left[I_z S_z + \frac{1}{2}(I_+ S_- + I_- S_+) \right] \tag{2.2}$$

expanded in a basis assuming I_z and S_z give good quantum numbers. In this form, the spin flip-flop terms are explicitly shown with the ladder operators I_+, I_-, S_+, and S_-.

In a refined version of the theory from Happer and coworkers [52], the polar interaction is again disregarded, but new terms are added. Using Happer's notation, the appropriate Hamiltonian is:

$$H = \alpha \vec{K} \cdot \vec{S} + A \vec{I} \cdot \vec{S} + \gamma \vec{N} \cdot \vec{S} + g_s \mu_B \vec{B} \cdot \vec{S} + g_I \mu_B \vec{B} \cdot \vec{I} + g_K \mu_B \vec{B} \cdot \vec{K} \tag{2.3}$$

where $\vec{I}$ is the nuclear spin of the alkali metal, $\vec{S}$ is the electronic spin of the valence electron of the alkali metal, $\vec{K}$ is the noble gas nuclear spin, $\vec{N}$ is angular momentum of the two interacting atoms, $\vec{B}$ is an externally applied magnetic field, and the g's are g-factors. A, γ, and α are coupling coefficients which are system specific. The last three terms describe the interaction of the spins with the external field. The first term describes the spin transfer between electron and nucleus. The second term is the alkali metal self hyperfine coupling. Finally, the third term includes the coupling of the electron spin to the angular momentum of the "molecule."

One of the main advances of Happer's theory is that he considers the nuclear spin interacting with the electron spin coupled with the bulk rotation, realizing that

a spin flip-flop between the rubidium electron and, for example, xenon nucleus does not conserve angular momentum. The excess angular momentum gets coupled into the "molecular" rotation. For both Herman and Happer, the exchange correlation between the alkali valence electron and the noble gas core electrons increases the efficiency of the spin exchange [32, 52]. According to Happer another reason for the large exchange cross section is the formation of van der Waals molecules of alkali metal-noble gas atoms formed in three body collisions. The third body is necessary to absorb and carry away the excess momentum from the alkali metal and noble gas atom inelastic collision.

2.2.3 Commentary: The Three-Body Problem

Happer's 1984 **Physical Review A** paper (same cited above) contains statements such as: "Spin exchange with heavy noble gases is dominated by interactions in long-lived van der Waals molecules." and

> ... spin-exchange rates between alkali-metal electron spins and the nuclei of heavy noble gases are completely dominated by interactions in van der Waals molecules. ... A Rb atom and a Xe atom collide in the presence of a third body, ..., and form a weakly bound van der Waals molecule.

Because of these statements, it has become popular in recent years for members of the Pines Group to describe the mechanism of spin transfer between the rubidium and xenon as being due to a three body collision that creates a van der Waals complex. However, this is only true for low pressure situations. A previous Happer paper [53] as well as Section X in the 1984 paper state that two-body collisions dominate at higher pressures. And a more recent paper from 1997 [54] states that for the conditions of most NMR applications, the spin-exchange process is effectively binary. For practically all of the work done in the group, the spin exchange process is best described by binary collisions and not the trinary collisions leading to van der Waals molecules. Two other papers that discuss spin-exchange in high pressure gases can be found in references [55, 56], and cross section parameters can be found in reference [57].

Chapter 3

SQUID Theory and Operation

3.1 Introduction

Superconducting QUantum Interference Devices (SQUIDs) were first created in 1964 [58]. They offer unsurpassed sensitivity in the detection of magnetic flux, and their first use in NMR experiments was during the 1970s [59, 60]. The body of work utilizing SQUIDs for magnetic resonance is still small but growing. Currently, the most likely place that a chemist might encounter a SQUID is in a magnetic susceptometer. Perhaps the success of some of our SQUID NMR and MRI will make the use of SQUIDs in magnetic resonance more widespread. Before I describe those experiments in the next two chapters, I want to explain exactly what SQUIDs are and how they work. There are a number of good general references and reviews on SQUIDs and their uses [61, 62, 63, 64, 65, 66].

3.2 Superconductivity

Superconductivity was first discovered in 1911, and most people today know something of the macroscopic properties of superconductors: they have zero electrical resistance, they can levitate magnets, and they must be kept *really* cold. Pure metals such as niobium, lead, and aluminum typically require liquid helium boiling at 4.2 K to cool them to the superconducting state. Newer ceramics,

such as various mixtures of yttrium-barium-copper-oxide (YBCO) become superconducting just above the boiling point of liquid nitrogen (77 K) and are called high transition temperature superconductors. One of the ongoing "Holy Grails" of materials science is the development of a room temperature superconductor. For more than forty years after the first discovery of superconductivity physicists struggled to understand how superconductivity worked. Finally in 1957 Bardeen, Cooper, and Schrieffer published their quantitative and predictive description, now known as BCS Theory [67, 68]. It is an elegant piece of work, and I personally believe that all physical scientists should work through the theory at least once in their lives. However, reproducing the mathematics is beyond the scope of this thesis. Instead, I will outline the general ideas here in order to give a qualitative but physical picture. For references on superconductivity, including BCS theory as well as important superconducting effects that are not touched upon here such as the Meissner effect, the reader is directed to references [69, 70, 71, 62, 72]. .

Two important effects occur in a material as the temperature is lowered towards the superconducting phase transition: pairing of electrons and Bose condensation. Under normal circumstances (non-superconducting temperatures) one can expect in a metal, for example lead, that there are many electrons above the Fermi level in the conduction band simply due to thermal energy excitation. As temperature is lowered, there are fewer electrons in the conduction band. At the same time, resistance decreases since there are fewer mobile electrons for collisions on top of the fact that they have slower speeds and less momentum to deflect other electrons. At the phase transition the electrons form pairs with oppositely directed angular momentum. Due to phonon scattering, there is an attractive potential that is stronger than the electron-electron electrostatic repulsion. To understand this attractive potential, remember that the electrons are not alone—there are many positively charged nuclei around them. When one electron is excited (thermally, for example), it leaves a positively charged hole in the lattice which attracts another electron. One commonly used analogy is of a ball rolling on a rubber sheet [62]. As the ball rolls, it depresses the sheet and other balls in the vicinity roll into the depression, seemingly following the first ball. The interaction is "phonon

mediated" because the movement or excitation of one electron creates an oscillating disturbance in the lattice which creates the positive potential, just as the ball disturbs the rubber sheet.

These electron pairs, called Cooper pairs, are actually single particles. It is not correct to envision the electrons as bonded the same way that atoms are bonded together to make molecules, but neither are the Cooper pairs point charges with twice the charge of electrons. A Cooper pair can be described by a wavepacket with a diameter of about 1 μm, a wavelength of 1 nm, and frequency of oscillation on the order of $10^{15} Hz$ [62]. The tiny point electrons distribute themselves over a relatively great distance in the weakly coupled pair. A further distinct property of Cooper pairs is that they are integer-spin bosons whereas electrons are fermion (half-integer spin particles). This allows for the superconducting phase transition's second effect of Bose Condensation of the Cooper pairs. The Bose condensation to a single quantum state whereby all the particles in a superconductor can be described by a single wavefunction will be important in describing the behavior of the Josephson junction.

3.3 The Josephson Junction

The next step in understanding the SQUID is the Josephson tunnel junction, named after the physicist who first predicted their properties in the 1960s [73, 74, 75]. A Josephson tunnel junction is the arrangement of two superconductors in close proximity but separated by a thin insulator. As can be guessed from the name "tunnel junction," Cooper pairs can tunnel across the insulator between the superconductors (as long as the insulator is thin), see Figure 3.1. It is easy to derive the Josephson relations using a simple picture of plane wave wavefunctions in each superconductor on either side of the barrier [70, 75, 62]. The form of the wavefunctions in the superconductors are:

$$\psi_1(x) = \sqrt{\rho_1(x)}\, e^{-i\theta_1}, \;\; \psi_2(x) = \sqrt{\rho_2(x)}\, e^{-i\theta_2} \tag{3.1}$$

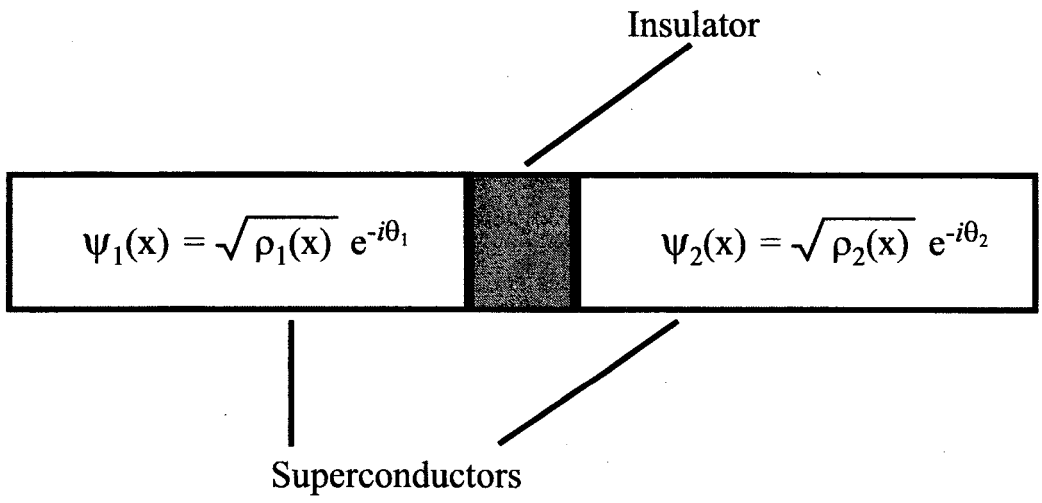

Figure 3.1. Schematic of a Josephson Tunnel Junction.

where $\rho_1(x)$ and $\rho_2(x)$ are the Cooper pair densities in the respective wavefunctions and θ_1 and θ_2 are the wavefunction phases. Time evolution of these wavefunctions is then given simply by the Schrödinger Equation:

$$i\hbar\frac{\partial\psi_1}{\partial t} = U_1\psi_1 + K\psi_2 \tag{3.2}$$

$$i\hbar\frac{\partial\psi_2}{\partial t} = U_2\psi_2 + K\psi_1 \tag{3.3}$$

where K is the coupling constant between the wavefunctions, and U_1 and U_2 are the energies of ψ_1 and ψ_2 respectively. Assuming an applied voltage difference between the sides $U_2 - U_1 = e^*(V_2 - V_1) = e^*V$, we can choose the zero point of energy midway between the energies of the wavefunctions where e^* is the charge of the particles, equal to $2e$ for Cooper pairs. The time evolution is now:

$$i\hbar\frac{\partial\psi_1}{\partial t} = \frac{-e^*V}{2}\psi_1 + K\psi_2 \tag{3.4}$$

$$i\hbar\frac{\partial\psi_2}{\partial t} = \frac{+e^*V}{2}\psi_2 + K\psi_1 \tag{3.5}$$

We can now substitute the actual wavefunctions, Equation 3.1, into the above equations. Separating real and imaginary parts and defining $\phi = \theta_2 - \theta_1$

$$\frac{\partial \rho_1}{\partial t} = \frac{2}{\hbar} K \sqrt{\rho_1 \rho_2} \cdot sin\phi \tag{3.6}$$

$$\frac{\partial \rho_2}{\partial t} = -\frac{2}{\hbar} K \sqrt{\rho_1 \rho_2} \cdot sin\phi \tag{3.7}$$

$$\frac{\partial \theta_1}{\partial t} = -\frac{K}{\hbar} \sqrt{\frac{\rho_2}{\rho_1}} \cdot cos\phi + \frac{e^* V}{2\hbar} \tag{3.8}$$

$$\frac{\partial \theta_2}{\partial t} = -\frac{K}{\hbar} \sqrt{\frac{\rho_1}{\rho_2}} \cdot cos\phi - \frac{e^* V}{2\hbar} \tag{3.9}$$

Since current is the amount of charge passing through a point per unit time (remember $Amp = Coulomb/second$), Equation 3.6, is basically an expression for current density from superconductor 2 to superconductor 1:

$$J = J_c sin\phi \tag{3.10}$$

J_c is the critical current density derived by Ambegaokar and Baratoff [76, 77]:

$$J_c = \frac{G_n}{A} \left(\frac{\pi \Delta(T)}{2e} \right) tanh \left(\frac{\Delta(T)}{2k_B T} \right) \tag{3.11}$$

where G_n is the tunneling conductance, A is the junction area, and $\Delta(T)$ is the superconducting gap parameter, which is basically the binding energy of the electrons of a Cooper pair. The second Josephson relation comes from subtracting Equation 3.8 from Equation 3.9:

$$\frac{\partial \phi}{\partial t} = \frac{2e}{\hbar} V \tag{3.12}$$

and describes the time evolution of the phase difference between the superconductors. The key points to note about Josephson junctions from the relations 3.10 and 3.12 is that current can flow even with no voltage. The current flow is determined by the phase difference between the two superconductors and can take any value from 0 up to a critical current that is determined by the particulars of the junction. In fact, applying a voltage will generally stop current flow because the current oscillates so quickly back and forth through the junction that no current is observed [70]. Furthermore, the junction does not follow the standard Ohm's

Law. Current is not proportional to the voltage; instead, applying a voltage to a Josephson junction only serves to modulate the current.

3.4 Parallel Josephson Junctions

The first type of SQUID was made of two Josephson junctions in parallel [58]. Referring to Figure 3.2 we can identify four important sections: superconductor P, superconductor Q, barrier a and barrier b. There are two Josephson junctions: $P-a-Q$ and $P-b-Q$. However the phase difference between the wavefunctions that describe superconductors P and Q must be the same across either junction since the plane waves that we have defined cannot have two phases in different regions. So the integrated Josephson relation describing the phase difference across the left junction is:

$$\Delta_{PQ} = \delta_a + \frac{2e}{\hbar}\int_{left} \vec{A}\cdot\vec{ds} \tag{3.13}$$

and across the right:

$$\Delta_{PQ} = \delta_b + \frac{2e}{\hbar}\int_{right} \vec{A}\cdot\vec{ds} \tag{3.14}$$

The phase difference Δ_{PQ} is made of two parts, an intrinsic phase difference δ_a and δ_b (which can be thought of the constant of integration when the Josephson relation 3.12 is integrated) and the phase difference due to a potential, written as the generalized vector potential $\vec{A}$. Setting these two equations equal and doing the appropriate Algebra we can derive a new relation between the intrinsic phase differences and notice that by Stoke's Theorem the loop integral of the vector potential is equal to the flux threading the loop:

$$\delta_b = \delta_a + \frac{2e}{\hbar}\underbrace{\oint \vec{A}\cdot\vec{ds}}_{Flux} = \delta_a - \frac{2\pi\Phi}{\Phi_\circ} \tag{3.15}$$

where $\Phi_\circ = \frac{h}{2e}$ is the flux quantum. This relation basically means that magnetic flux entering the SQUID loop causes a current flow by changing the intrinsic phase

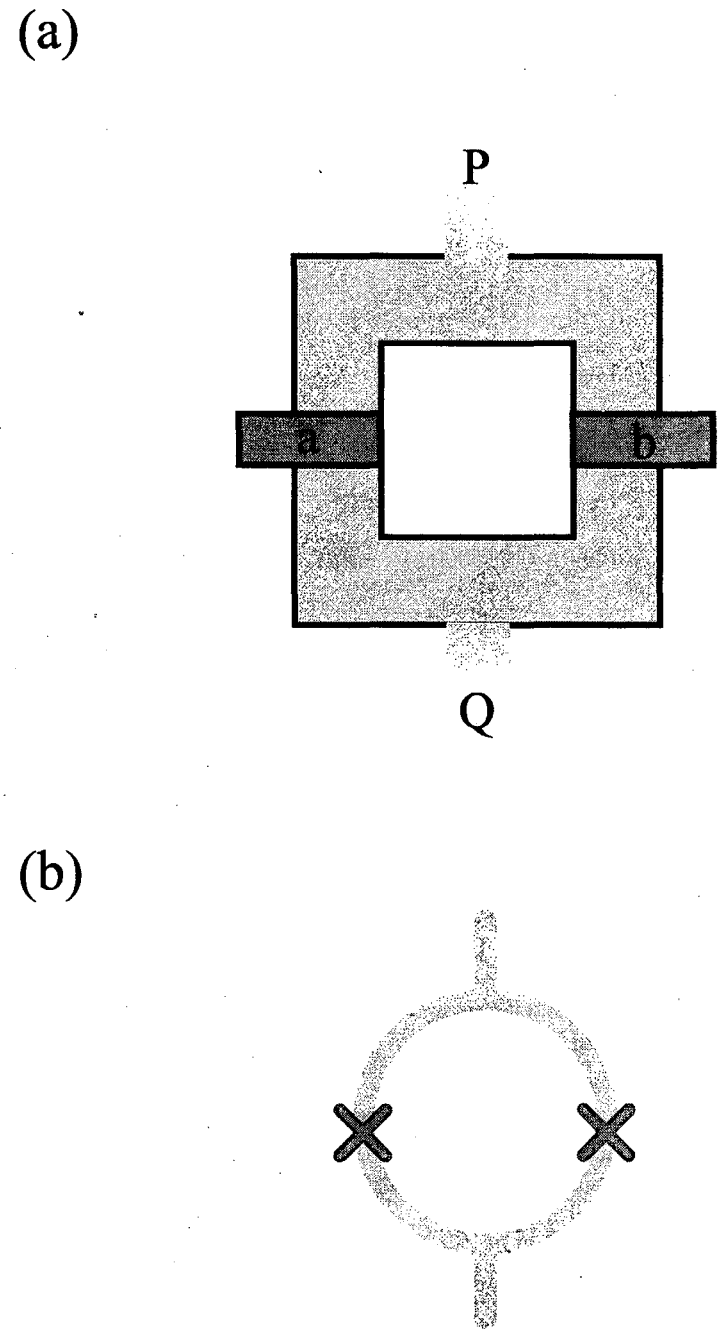

Figure 3.2. (a) Two Josephson junctions in parallel make a SQUID. (b) Circuit diagram representation of a SQUID.

differences, $\delta_{a,b}$, across the junctions. The total current from superconductor P to Q is the sum of the current across the two junctions.

$$\begin{aligned} J_{PQ} &= J_a + J_b = J_c^a \, sin\delta_a + J_c^b \, sin\delta_b \\ &= J_c^a \, sin\delta_a + J_c^b \, sin\left(\delta_a - \frac{2\pi\Phi}{\Phi_\circ}\right) \end{aligned} \tag{3.16}$$

However, unlike the Faraday Law which says that a change in flux induces a voltage and current in a loop, static flux will cause a current flow in a SQUID. Another important attribute is that while the difference in intrinsic phases may be an increasing function of flux, the actual current is still sinusoidally dependent on magnetic flux.

3.5 Actual SQUIDs

Actual SQUIDs are basically microchips made of superconducting material deposited onto a substrate. There are a number of procedures that have been developed for fabricating SQUIDs. I will describe the general procedures that the Clarke group used since they provided us with SQUIDs [78, 79].

3.5.1 Low-T_c Devices

The low transition temperature SQUIDs were fabricated based on the design of Ketchen and Jaycox [80, 81]. They were made by photolithographical patterning and etching of thin films deposited on silion wafers. The SQUID loop was a square washer made of niobium with dimensions of 25 μm for the inner length and 900 μm for the outer. The junction barriers were composed of niobium oxide, and the second superconductor was made of lead with 5% indium. These SQUIDs did not look like the parallel Josephson junction diagram in the previous section. These low temperature SQUIDs were actually tri-layer sandwiches with superconducting niobium on the bottom making almost an entire loop, two tiny patches of insulator

made of niobium oxide on top of the two ends of the "broken" loop, and finally a lead-indium bridge on top of the insulators as shown in Figure 3.3.

144 SQUIDs could be fabricated on a single 50 mm diameter oxidized silicon wafer approximately 1 mm thick. The first component patterned and deposited was a copper-gold damping resistor, necessary to remove the hysteretic behavior of an undamped SQUID caused by circulating currents in the SQUID from inductive or capacitive coupling of the SQUID to its input coil [78, 82, 83, 84]. The first niobium layer was then deposited and etched to make the washer and the feedback coil. Two insulating layers of SiO were then deposited on top of the niobium, leaving exposed two 2 $\mu m \times$ 2 μm square patches for the junctions. These junction areas were then protected by photoresist before a second niobium layer was patterned for the input coil of the flux transformer (which I will talk more about later), leads, and contact pads. Finally, the niobium at the junctions was oxidized in an Ar/O_2 (90%/10%) plasma discharge, and then the lead-indium bridge was created. The silicon wafer was usually diced to make individual SQUID chips before the lead-indium bridge was deposited. Although the SQUIDs themselves each had an area of about 1 mm^2, each SQUID chip had an area of approximately 25 mm^2 due to the input coil, contact pads and leads and a little bit of edge room.

The SQUIDs that I used were fabricated by Dinh TonThat, Ph.D. 1998 from the Clarke Group. They had typical critical current values of 40 μA. The SQUID inductance was about 100 pH with 60 pH from the square washer and 40 pH from the break or slit in the washer. The niobium input coil (in the second niobium layer) was a 48 turn square coil with a self-inductance of 150 nH and SQUID mutual inductance of 3.5 nH. The junction shunt resistors each had a resistance of 3 Ω. The white noise for good low-T_c SQUIDs is 1 $\mu\Phi_0/\sqrt{Hz}$. So a device with an effective area of 1 mm^2 gives a field noise of 2 $fT/\sqrt{Hz}$.

3.5.2 High-T_c Devices

The devices that became superconducting at liquid nitrogen temperatures were made of different materials than the low-T_c devices but were again fabricated by

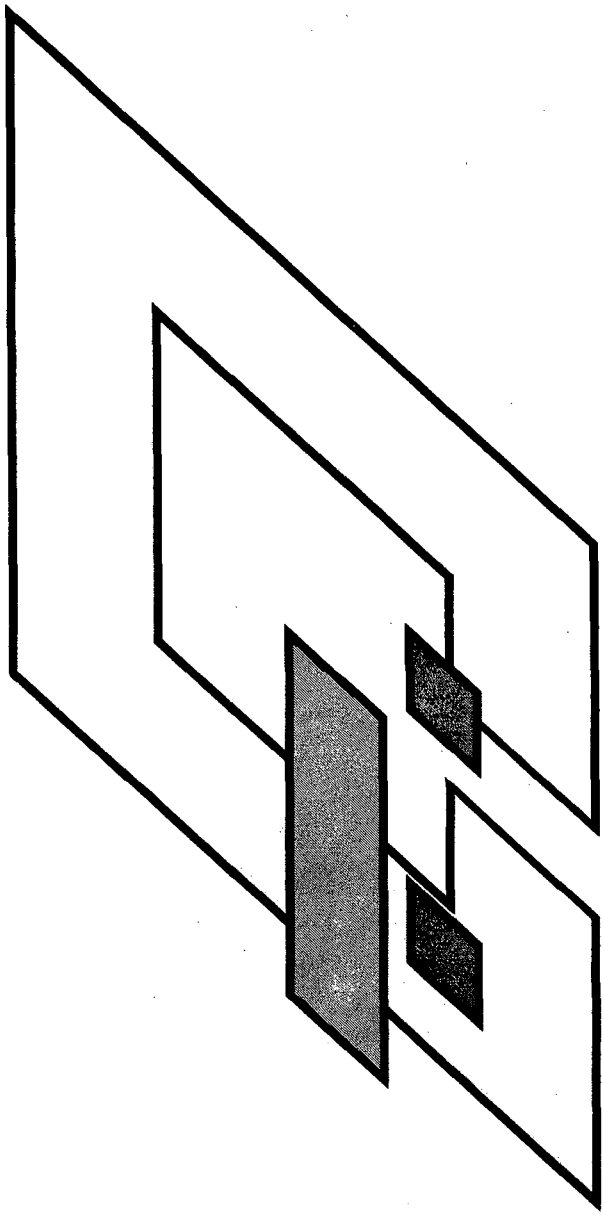

Figure 3.3. Schematic of the low temperature SQUID "tri-layer sandwich" (shown sideways). The bottom layer is the broken niobium square washer. The middle layer is composed of the two square patches of niobium oxide insulator. Finally the last layer is the bridge made of lead-indium spanning the two insulators and the slit in the washer.

reactive ion etching of thin layers of superconductor deposited on a substrate. Yttrium-barium-copper-oxide (YBCO) with an empirical formula of $YBa_2Cu_3O_{7-x}$ deposited on strontium titanate ($SrTiO_3$ or STO to the physicists) were the materials of choice for the Clarke group. The Josephson junctions of the high-T_c devices are actually not superconductor-insulator-superconductor tunnel junctions. Instead, they are known as weak link grain boundary junctions formed at the interface of two superconductors that have different crystal orientations. This can be done controllably and reproducibly by growing the SQUID onto a bicrystal substrate made by slicing a single crystal of strontium titanate in half and cutting a wedge from one of the halves then fusing the crystal back together (sans wedge), see Figure 3.4. The YBCO that is deposited on the bicrystal will follow the two orientations of the substrate, and microbridges across the grain boundary will produce Josephson junctions [78].

YBCO thin films were grown on the substrate by laser deposition (blasting a chunk of YBCO with an excimer laser and allowing the crystal to reform on the substrate). Patterning was done photolithographically and etched using a reactive argon ion beam. The simplest high transition temperature SQUIDs formed on grain boundaries are not trilayer sandwiches and more closely resemble the parallel junction schematic. Some of those produced by the Clarke group were composed of a square SQUID washer with dimensions of 32 μm x 32 μm and junction widths of 1-3 μm. White flux noise for these SQUIDs can be comparable to the noise of low temperature devices 1.5 $\mu\Phi_0/\sqrt{Hz}$, but the effective areas are extremely small, meaning the magnetic field noise is high, on the order of 1 $pT/\sqrt{Hz}$, 1000 times higher than low-T_c devices.

In order to increase the effective area, different magnetometer configurations have been developed. The three types of high-T_c SQUID magnetometers that I used were: the directly coupled magnetometer, the fractional turn (multiloop), and the multiturn flip-chip magnetometer. In the directly coupled magnetometer there is a large 7 mm x 8 mm pickup loop which directly couples current to the 32 $\mu m\times$ 32 μm SQUID loop, Figure 3.5. Note that current can only circulate in the large loop by passing through the SQUID. The field noise of the directly coupled

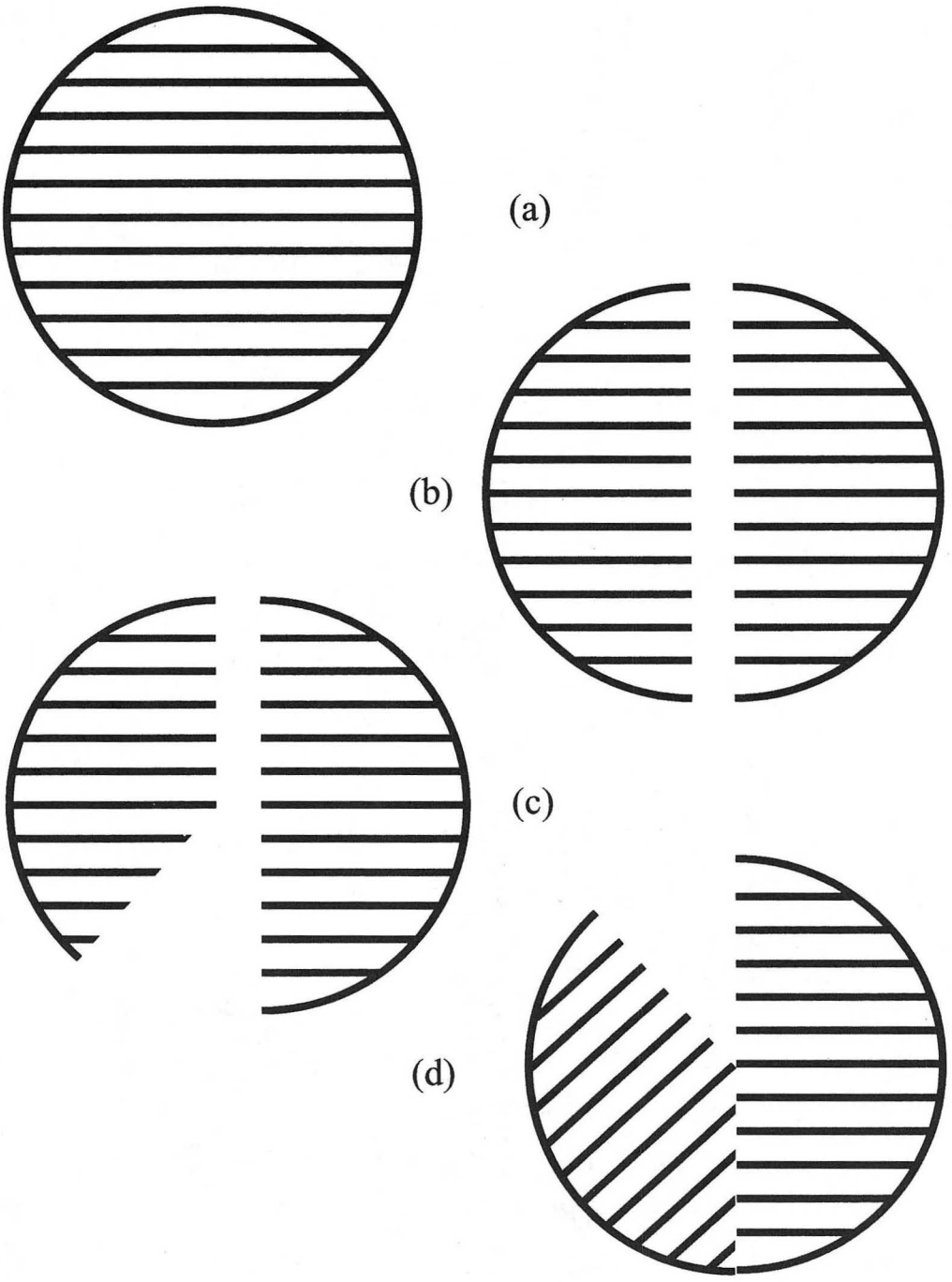

Figure 3.4. **The Strontium Titanate Bicrystal. (a) The full crystal; lines indicate crystal orientation. (b) Split crystal. (c) Wedge cut from crystal. (d) Crystal Halves fused back together with lattice mismatch.**

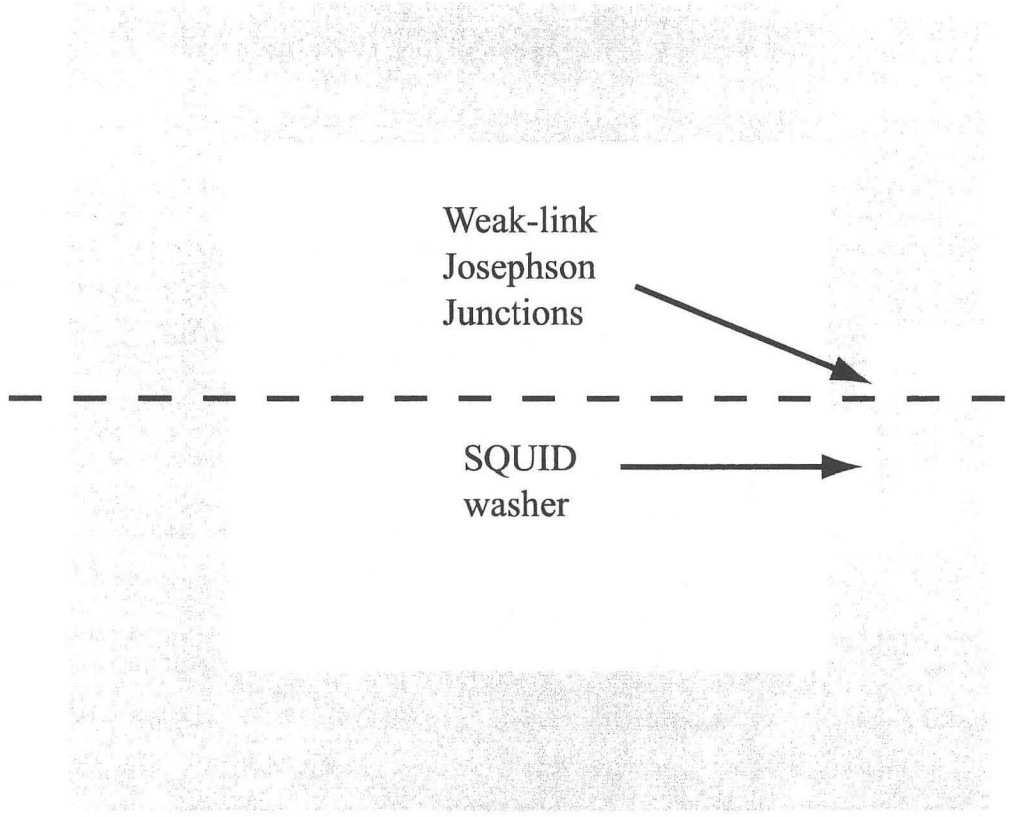

Figure 3.5. **Schematic of the high transition temperature SQUID directly coupled magnetometer. Figure not to scale. The large rectangular loop is the pickup loop. The SQUID washer is shown in the right part of the pickup loop. The dashed line represents the grain boundary. The junctions are 1-3 μm wide. They are the only narrow lines of superconductor material crossing the grain boundary.**

SQUID that I used was 70 $fT/\sqrt{Hz}$. The fractional turn, also called multiloop or cartwheel, magnetometer increases its effective area by cleverly joining many small loops in parallel [85, 86, 87, 78]. Figure 3.6 shows a photograph of the SQUID fabricated by Frank Ludwig in 1994. There are 16 fractional loops, and the bicrystal boundary runs horizontally through the middle of the SQUID. This device had an outside diameter of 7 mm, and an effective area of 1.84 mm^2. It had a flux noise of 25 $\mu\Phi_0/\sqrt{Hz}$, giving a field noise of 30 $fT/\sqrt{Hz}$. A third design is the flip-chip magnetometer in which a large coil and a small coil connected together (in a flux transformer configuration) are patterned from YBCO on a separate piece of strontium titanate and then flipped over on top of the SQUID [88, 78]. The flux transformer and SQUID are inductively coupled since flux that enters the large loop causes a supercurrent flow in the small loop producing a flux directly at the SQUID. The last SQUID magnetometer that I used was such a SQUID. Its pickup area was approximately 1 cm^2, while its effective area (number for calculating field noise) was approximately 1 mm^2. This particular SQUID had a rather high white noise of 160 $fT/\sqrt{Hz}$.

3.6 Operation: The direct current SQUID

There are two basic configurations or methods of SQUID operation as a magnetometer. There is the direct current (dc) SQUID [58] and the radiofrequency (rf) SQUID [89] . The rf SQUID was discovered later than the dc SQUID but has been more widely commercially available since the 1970s. It is generally less sensitive than the dc SQUID; therefore, all of the SQUIDs currently used in the Pines Group are dc SQUIDs. For more information on the rf SQUID, good places to start looking are in references [89, 78]. I showed in Section 3.4 that flux entering the SQUID loop causes a current in the SQUID. So measuring this current should give a direct measure of magnetic fields. Unfortunately, there is not a good method to measure this current. Instead, the SQUID is driven to a voltage mode by the application of an external dc current, causing it to act as a flux-to-voltage converter. To understand how this works, first consider a complete superconducting

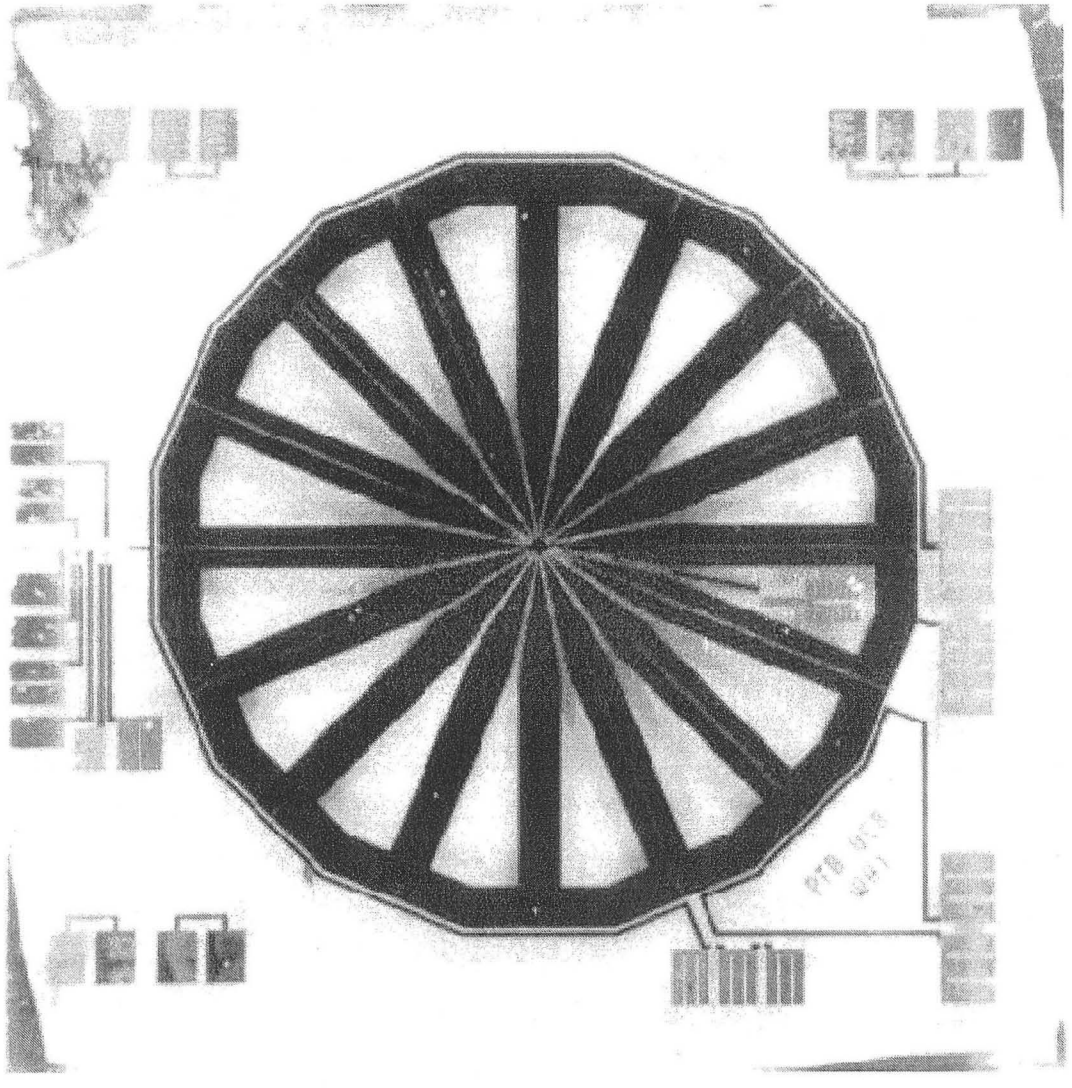

Figure 3.6. **Photograph of the cartwheel (multiloop) magnetometer fabricated by Frank Ludwig in 1994. There are 16 fractional loops. The bicrystal boundary runs horizontally through the center of the SQUID. The junctions lie across the boundary but cannot be seen in the picture.**

loop. As flux passes through this loop, a supercurrent (current with no resistance) circulates in the loop in an effort to quantize the flux in the loop. For integer number of flux quanta in the loop, no current will flow. Both of these phenomena are also true for a superconducting loop with two flaws in it (i.e. a SQUID). But one difference is that this flawed loop can not support the same amount of supercurrent as the perfect loop. There is a maximum current or "critical current" that the Josephson junctions can support, as was implied from the Josephson Equation 3.10. A potential (voltage) will be necessary to force more current through the junctions. The converse is also true, when more current than the critial current passes through the junctions, a voltage is developed. By applying a bias current to the SQUID of an amount just over the SQUID critical current, the sum of the individual junction critical currents, any flux that enters the SQUID loop will induce a circulating current in the loop which will produce a voltage that *can* be measured.

The SQUID current vs. voltage (I-V) curve is shown in Figure 3.7. The first thing to note is that no voltage is developed until the critical current is surpassed. The next important feature of the I-V curve is that the critical current changes depending on the amount of flux in the loop. It has a maximum value for integer numbers of flux quanta ($\Phi_\circ$), and a minimum value for half-integer numbers of flux quanta. The asymptotic limit of the curves is the resistance R equal to the junction shunt resistance. A simple picture from Clarke [78] considers a SQUID with two Josephson junctions a and b, each with a critical current of $I_\circ$, so the maximum current that the SQUID can support before going to the voltage state (developing a voltage) is equal to $2I_\circ$. If a small flux, less than $\Phi_\circ/2$, is applied to the SQUID, a current J will circulate in order to cancel the flux and force the number of flux quanta in the loop to an integer (zero in this case). The current through junction a is now equal to $+J$ and equal to $-J$ through junction b (circulating current, remember). Now imagine applying a direct current, I, to the SQUID. It will split evenly to both junctions. The current now flowing through junction a is $\frac{I}{2} + J$, and likewise junction b now has a current $\frac{I}{2} - J$. If we continue to increase the applied current to the SQUID, junction a will hit its critical current

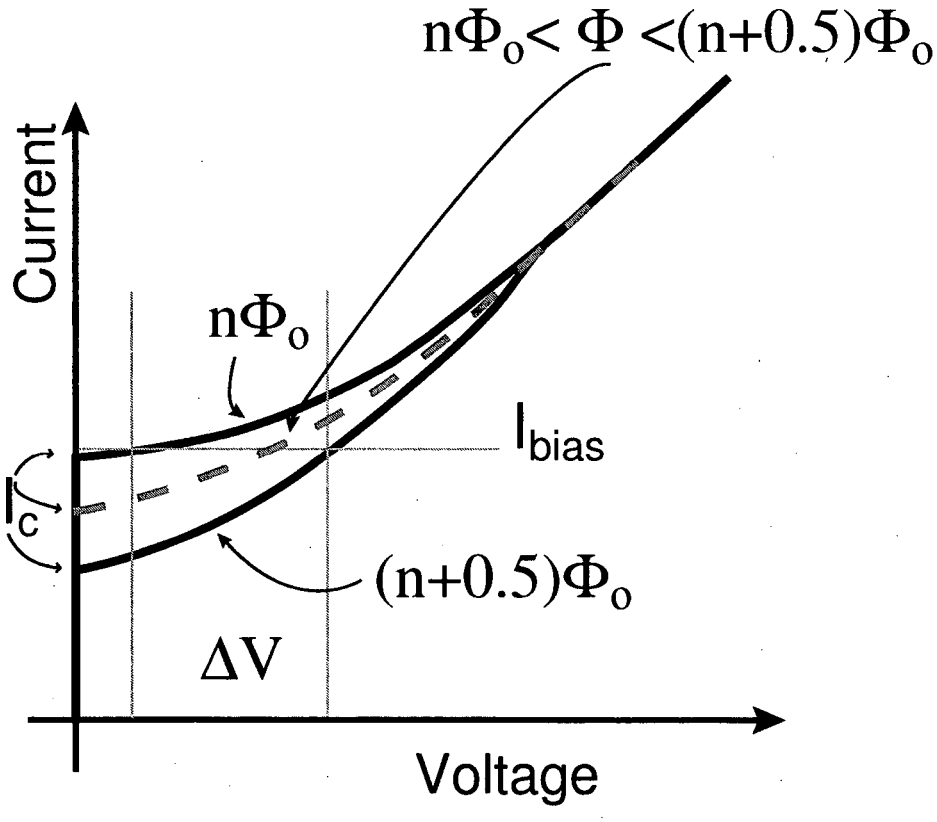

Figure 3.7. Current versus Voltage characteristic of SQUIDs. Voltage is developed only after the SQUID critical current is surpassed. The critical current is dependent on the magnetic flux in the SQUID loop.

at $\frac{I}{2} + J = I_\circ$ or rearranged $I = 2I_\circ - 2J$. This means that the current flowing through junction b is $\underbrace{(2I_\circ - 2J)}_{I}/2 - J = I_\circ - 2J$. Any more applied current would create a voltage—the SQUID has reached its *effective* critical current. The sum of the currents flowing through the junctions is $\underbrace{I_\circ}_{a} + \underbrace{I_\circ - 2J}_{b} = 2I_\circ - 2J$, which is smaller than the maximum critical current. This effective critical current will continue to decrease to a minimum as the applied flux reaches $\Phi_\circ/2$. For more flux than $\Phi_\circ/2$, the SQUID decides that instead of cancelling the flux, it would be better to add to the flux and bring the flux to a full flux quantum. So the current J reverses direction, and as flux increases to a full flux quantum, the SQUID critical current also increases up to its maximum value.

The SQUID critical current is a periodic function of magnetic flux. So operated in the dc mode by applying an external current slightly higher than the SQUID critical current, voltage is also a periodic function of magnetic flux, Figure 3.8. This means that a SQUID actually cannot detect anything greater than a flux quantum, $\Phi_\circ$. It detects flux modulo flux quantum.

3.7 Operation: The Flux-Locked Loop

The way to get around this limitation is with additional electronics. We use a design by Drung [90, 91] that has a very high bandwidth, from DC up to 5 MHz with the correct components. The electronics that we use have a bandwidth of about 1 MHz. The idea behind the electronics is to read the voltage from the SQUID (indicating external flux threading the SQUID loop) and then return flux to the SQUID in order to cancel the flux that it is sensing. The order of events is as follows: the SQUID (operated with a bias current) feels a little bit of flux, the electronics detect a voltage and send current to a small coil beneath the SQUID in order to cancel the flux so that no voltage is generated across the SQUID. If the external flux increases, the current that the electronics sent to the coil will not be enough to cancel the flux, the SQUID feels a net flux, develops a voltage, and the electronics again try to compensate by increasing the current to the coil. This

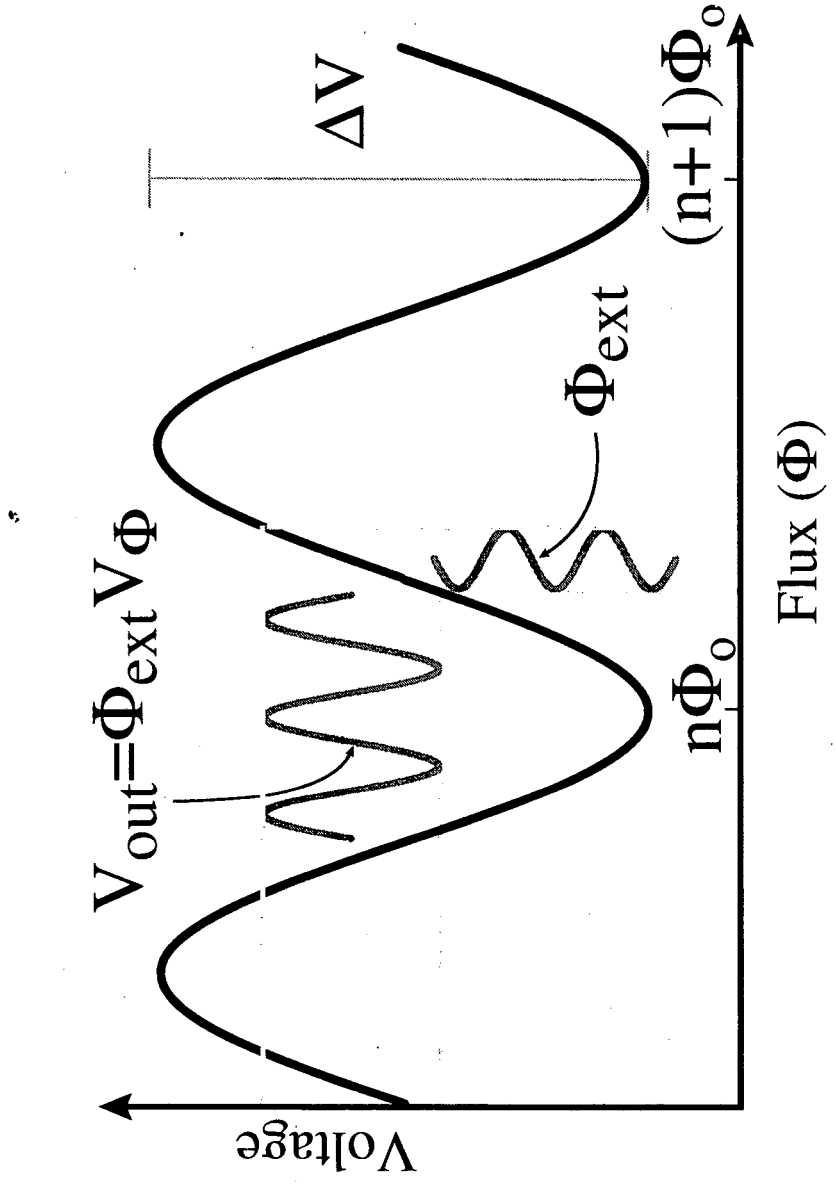

Figure 3.8. dc SQUID voltage versus flux. Voltage is a sine function of flux in the SQUID loop when the SQUID is operated in the direct current mode. For small oscillating magnetic fluxes, precessing magnetization for example, the voltage is given by the flux multiplied by the slope of the V-Φ curve at that point, V_Φ.

positive feedback flux-locked loop effectively locks the SQUID to one position on its voltage versus flux (V-Φ) curve. And the steeper the slope $\frac{dV}{d\Phi}$ at the position that the SQUID is locked, the more sensitive the magnetometer. The modulation depth is the value ΔV in Figure 3.8. Since the period of the V-Φ curve is always the flux quantum, $\Phi_\circ$, the modulation depth basically determines the slope $\frac{dV}{d\Phi} = V_\Phi$. Therefore it is important to have a large modulation depth in order to operate; a shallow ΔV will mean less sensitivity as well as more difficulty in locking the SQUID.

Figure 3.9 shows a schematic of the SQUID operated with a flux-locked loop. A bias current I_B is passed to the SQUID. When flux enters the SQUID, it develops a voltage. The voltage is amplified by two stages of amplification (pre-amp and amplifier) before it is passed to the integrator. The now phase corrected voltage is split to a buffer and to the feedback coil which is inductively coupled to the SQUID with a mutual inductance M_f. The feedback resistor R_f converts the voltage into a current for the feedback coil. The buffer holds the SQUID signal and creates the proper 50 Ω output impedance so that external electronics can properly interface with the SQUID feedback electronics. Finally the "Reset" is a an externally controlled photocoupled analog switch (Siliconix DG308) which shorts out the integrator when the NMR excitation pulse is applied. Without the switch, the integrator invariably saturates (to the electronic rail) disabling it and the rest of the circuit. The recovery time of the integrator without the reset and therefore the NMR dead time (time between the application of the pulse and the start of signal acquisition) is on the order of milliseconds—too long for many NMR experiments.

3.8 Flux Transformer and Gradiometer

The superconducting flux transformer is another important device or concept necessary to use the SQUID as a magnetometer. The length of the square loop for practical SQUIDs is on the order of 100 μm. Like any tiny coil, the effective sensing area is very small. This means that a bare SQUID can sense only tiny

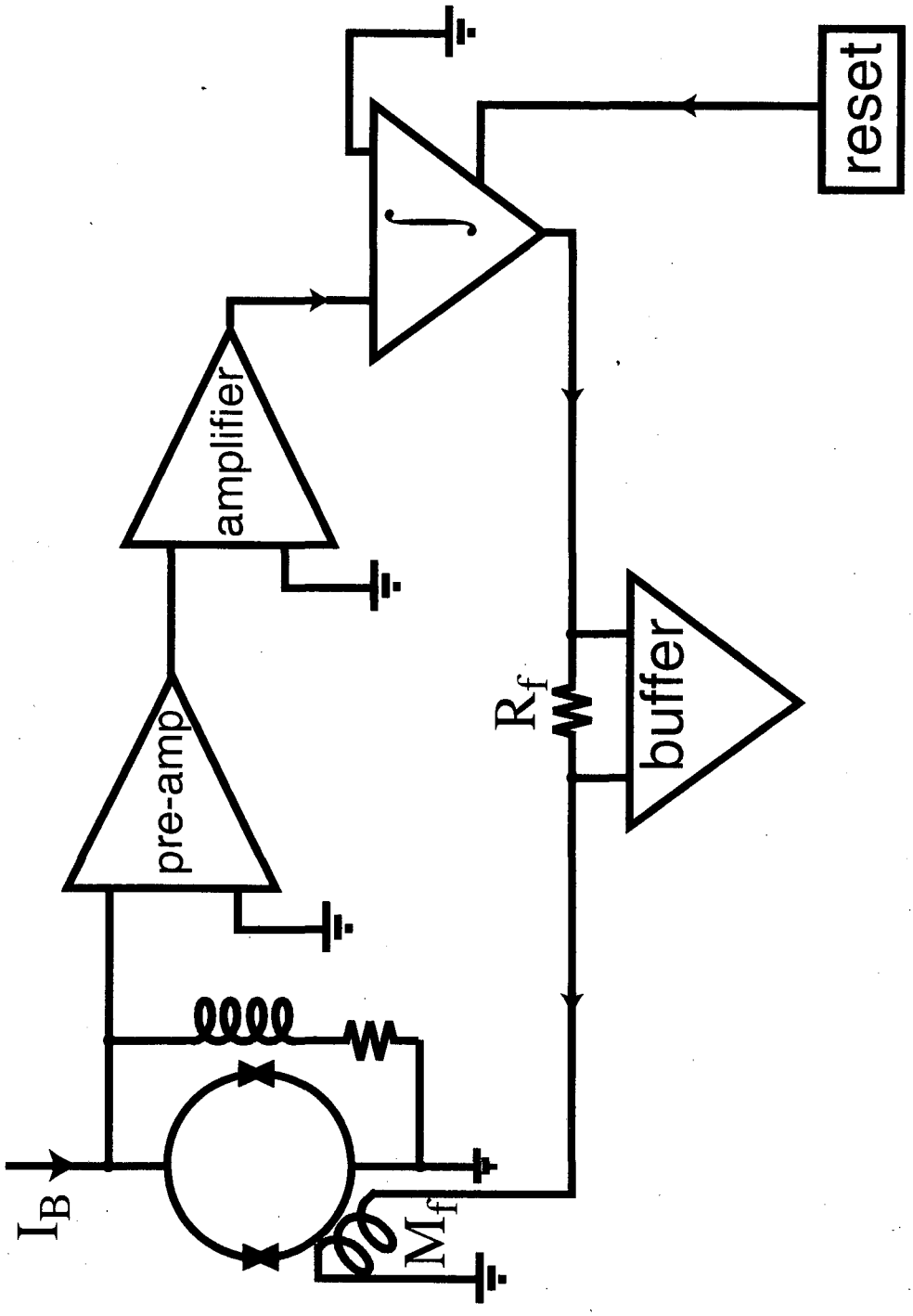

Figure 3.9. Schematic showing the Flux-Locked Loop.

samples or tiny fractions of larger samples. Since the NMR signal scales with the number of nuclei in a sample (or number that the detector can "see"), having a tiny SQUID means getting a miniscule signal. Therefore SQUIDs, especially the low-T_c SQUIDs, often employ superconducting flux transformers in order to increase their sensing area. Figure 3.10 shows schematically two types of flux transformers. The first type in (a) is a simple design with a single turn pickup coil and a 4-turn input coil. A magnetic flux Φ at the pickup coil induces a current J that flows through the input coil. Since the input coil is located close to the SQUID, and often patterned on the same chip, flux is coupled directly and efficiently into the SQUID washer. The pickup coil and input coil are generally not identical loops, but do have matched inductances [78]. Using a flux transformer for an NMR experiment is convenient since the SQUID does not have to be located close to either the static or pulse magnetic fields. It can be far removed and well shielded from ambient noise. Figure 3.10 (b) is a variation on the flux transformer. Instead of a single pickup loop, there are two, counterwound loops. This is a first-order (axial) gradiometer. Magnetic fields that are constant in both loops create currents that cancel each other, and nothing is sent to the SQUID. Magnetic field gradients, on the other hand, are detected by this configuration. In an NMR experiment the gradiometer is centered in the static and pulsed fields while the sample is placed in only one of the loops. The static and excitation fields are transparent to the SQUID, but the signal from the sample is detected since no signal is generated in the empty loop.

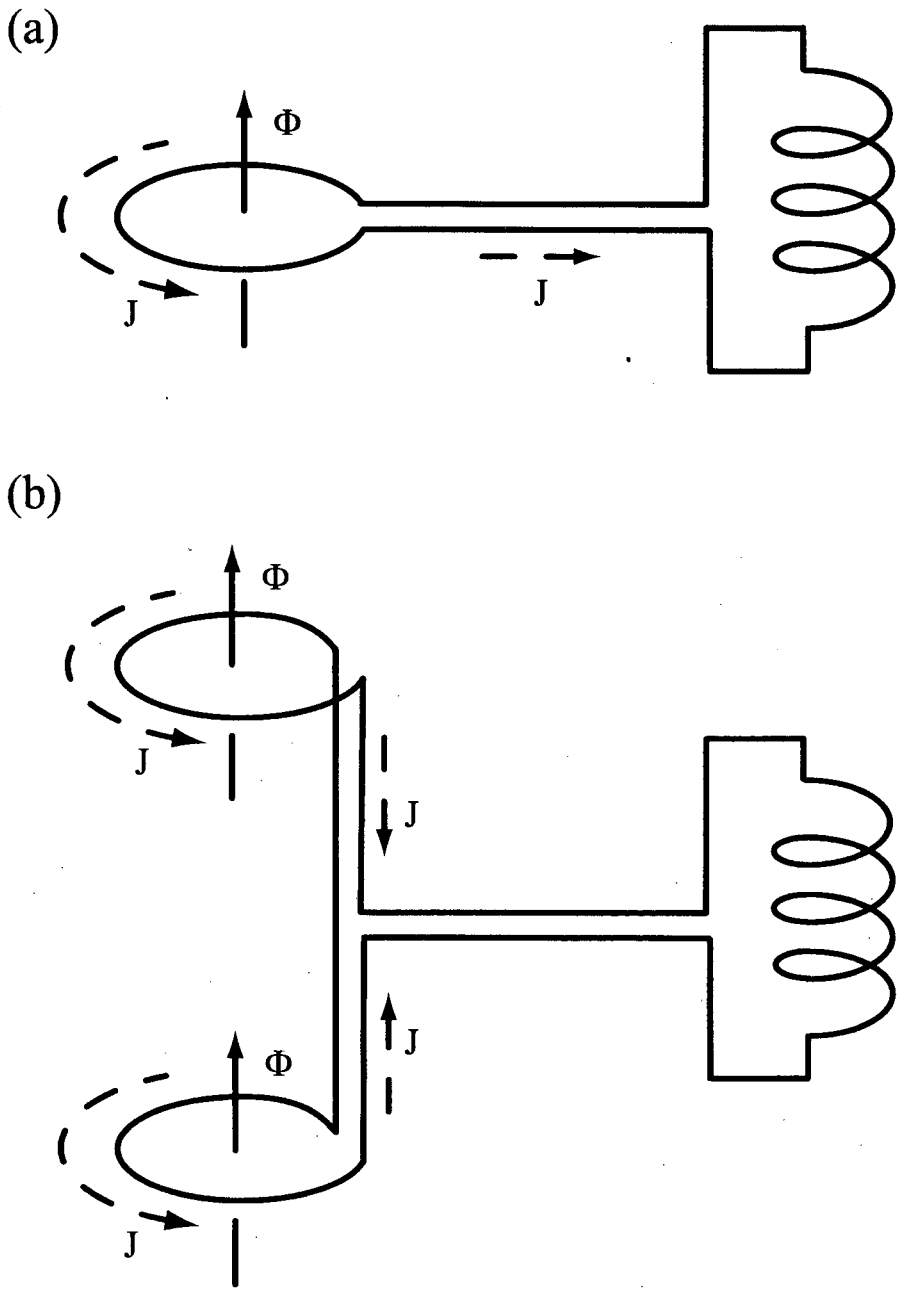

Figure 3.10. Superconducting flux transformers. (a) Simple flux transformer. (b) Gradiometric flux transformer.

Chapter 4

The Low Critical Temperature SQUID Days

4.1 Introduction

The first SQUIDs in the Pines Group were low transition temperature SQUIDs. By the time I joined the group, the commercial SQUID made by Biomagnetic Technologies, Inc. (BTI) was long gone. Instead, we used SQUIDs manufactured by our collaborators in the Clarke group. They were made of niobium, niobium oxide, and lead-indium and required liquid helium to operate. The experiments that were accomplished using the low-T_c SQUID were 1-D imaging of hyperpolarized helium gas in a static field of 5 Gauss (17.6 KHz), 2-D imaging of hyperpolarized solid xenon at 10 Gauss (11.8kHz). These Magnetic Resonance Imaging (MRI) pictures remain the lowest field images of milliliter sized samples with millimeter resolution ever taken. We also acquired the first directly detected 2-D pure NQR spectrum taken of ^{27}Al in ruby.

4.2 Ultra Low Field Imaging

In 1972 Lauterbur, Mansfield and Grannell took the first nuclear magnetic resonance images [9, 10]. MRI has since proven to be a powerful imaging technique

for medical diagnostics and materials characterization. At the same time that MRI was being born, X-ray computed tomography (CT) was also being developed [92]. And after thirty years, there are more CT scanners in existence than MRI machines. CT scans use harmful x-rays compared to MRI's harmless radio waves. MRI is capable of a higher resolution due to limitations in the beam collimation process in X-ray CT [11]. It is also possible for slice selection at any angle using MRI. So why do hospitals prefer X-ray CT over MRI? One reason may be familiarity since X-ray imaging has been around for so much longer than MRI (in non-CT mode), and some people may know and still be scared that MRI is truly *nuclear* magnetic resonance imaging. But the biggest reason for paucity of MRI machines is that they are expensive, and the cost of MRI scans is high. A regular chest x-ray will cost a patient $20 compared to a body MRI scan billed around $1500. The main cost comes from the construction and operation of the huge superconducting magnets. Field strengths around 1.5 Tesla are typically required to achieve the sensitivity and resolution necessary for medical diagnostics. A further requirement that the static magnetic field be homogeneous in the region to be imaged necessitates making the magnets bigger and bigger and more and more expensive. "Open MRI" machines further complicate the engineering.

The ability to take MRI pictures without the superconducting magnet, perhaps using only Earth's magnetic field, would be an incredible advancement. It would mean cheaper, more widely available, and more versatile MRI. Furthermore it would obviate the problem of susceptibility artifacts that arise from magnetic susceptibility differences in neighboring tissues, like ghosting or overlap of structures in the image. To understand this effect, keep in mind that nuclei will precess at the Larmor frequency corresponding to the magnetic field that they *feel*, which is not necessarily the field that is *applied* to them. Since the magnetic susceptibility of a certain tissue affects the magnitude of the magnetic field in that tissue, image overlap, for example, can occur when nuclei in different tissues feel the same magnetic field although the applied magnetic fields are different. Because the nuclei would then precess at the same frequency, they would appear in the MRI in the same location. Susceptibility effects scale linearly with field strength; therefore,

the weaker the applied field, the smaller the effect.

The difficulty with simply imaging without the powerful magnet is twofold: first of all the smaller the magnetic fields, the smaller the magnetization and therefore signal from the sample (recall Equations 1.8 and 1.9). Secondly the sensitivity of the detection equipment decreases as the Larmor frequency decreases. The standard tuned circuit detects changing magnetization according to the Faraday Law. Signal in terms of voltage, V, is proportional to the change in magnetic flux, $\frac{d\Phi}{dt}$. For a magnetic moment precessing at the frequency ω, the voltage is then proportional to the frequency ω.

$$V(t) \propto \frac{d\Phi}{dt} \propto \omega \tag{4.1}$$

Both of these factors lead to the same observable: smaller signal. Besides the obvious reason that smaller signal is harder to detect, signal-to-noise is also an important determinant of resolution in MRI. Mathematically, MRI resolution determined by gradient strength; however, strong gradients spread out the signal and decrease the peak signal-to-noise. With too small a signal, it does not matter what the theoretical resolution due to the strength of the gradients may be. So in practice, the most important determinant of resolution in MRI is signal-to-noise per voxel (3-D pixel). Vanishingly small NMR signal would suggest that Earth's field MRI is prohibitive, at least using conventional approaches (refer to Section 5.9 for quantitative estimates). Therefore we use an unconventional method: ultra low field MRI by combining the techniques of optical pumping of noble gases with the detection of MRI signal using superconducting quantum interference devices (SQUIDs).

4.2.1 MRI with Optical Pumping and MRI with SQUIDs

The first use of optically polarized noble gases for magnetic resonance imaging was reported in 1994 by Albert and coworkers [93]. Since then, hyperpolarized noble gas MRI has been rapidly becoming a standard technique [94, 95, 96, 97, 98, 38, 39]. Around the same time, the first use of a SQUID for MRI (which was in

fact low-field MRI) was reported by Seton and coworkers in 1995 [99]. Other early work was also from those researchers [100, 101]. Before the work described here [102] there was one prior published work using hyperpolarized helium in low-field MRI [103]. As of the writing of this thesis, the interest in low-field MRI using OP gases has increased [104, 105]. But since these experiments used conventional tuned circuit detectors, they were performed at higher magnetic fields than our work.

4.2.2 Imaging Theory: Projection Reconstruction

Recall from Section 1.4 that having a gradient in the applied magnetic field will spread out the NMR spectrum in frequency space, which can be related to distance space by knowing the gradient strength and the gyromagnetic ratio of the nuclei one is looking at. A gradient in one direction, the x direction for example, projects into the frequency domain the spatial distribution of nuclei in the x direction. A gradient in the y direction would be necessary to get information on the density of nuclei in the y direction. The principle behind the method of Projection Reconstruction is that by collecting a series of these 1-D projections each with different orientations of the gradient with respect to the sample a 2-dimensional (or even 3-D) map of the nuclear distributions can be obtained. Figure 4.1 shows a cartoon of the frequency domain MRI spectra that would be obtained for the two circular objects in different orientations in a magnetic field with gradient. The low transition temperature SQUID imaging probe contained only a single pair of gradient coils, so it was necessary to rotate the sample inside the probe in order to collect different spectral projections and obtain 2-D images.

The raw data from our sample rotations was a polar raster of time space with each FID having its native time dimension and further having an angle dimension. We decided that it was best to convert the data to a regular time×time Cartesian space. Figure 4.2 shows the relation between the experimental polar raster and the Cartesian raster. In order to fill out the Cartesian plane, we interpolated points based on a linear average of the four polar points (true data) that surround any

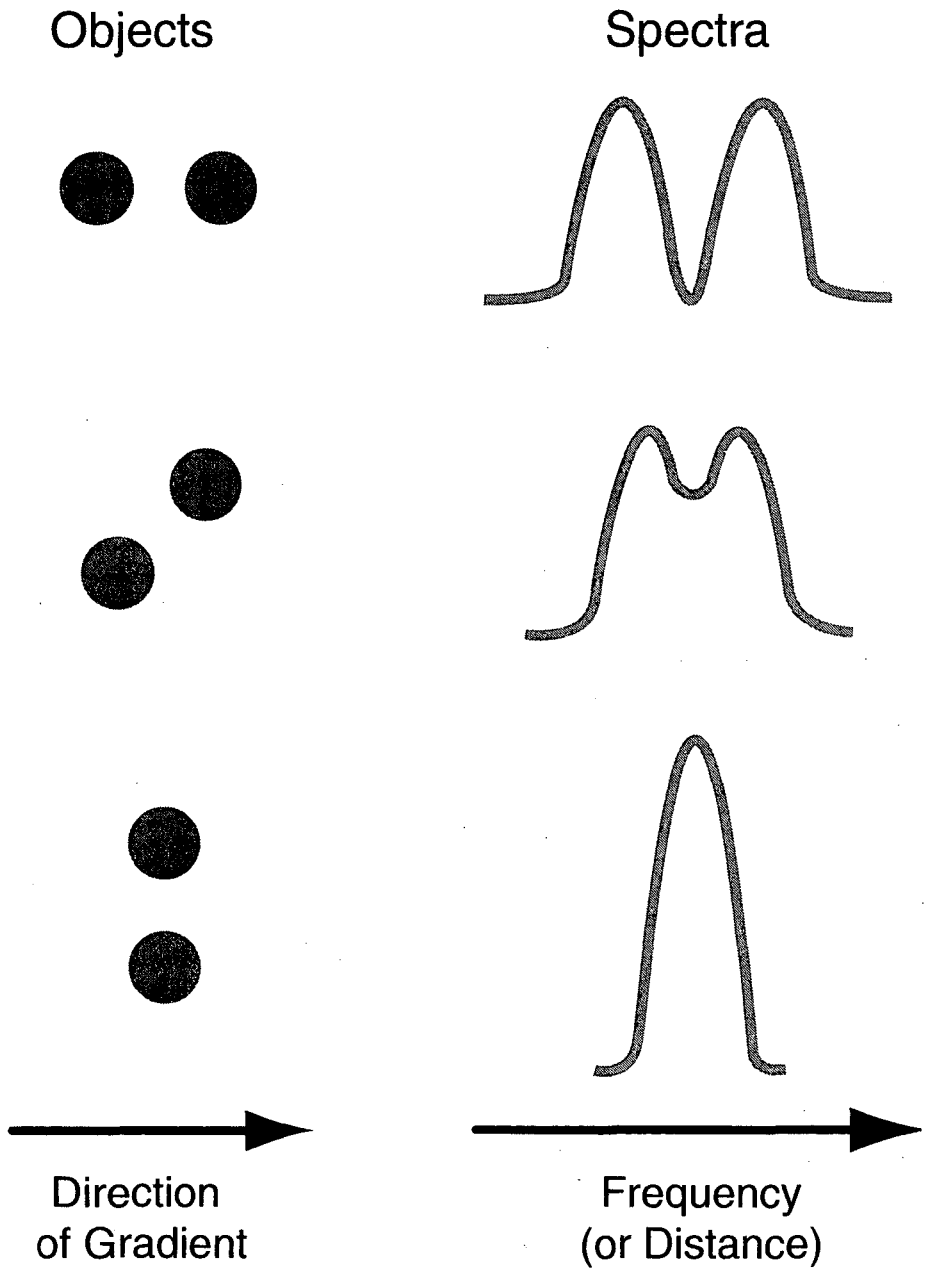

Figure 4.1. 2D Imaging: Projection Reconstruction. 2 dimensional imaging is done by changing the orientation of the gradient relative to the sample. The 1-D projections can then be reconstructed to give the full 2-D image.

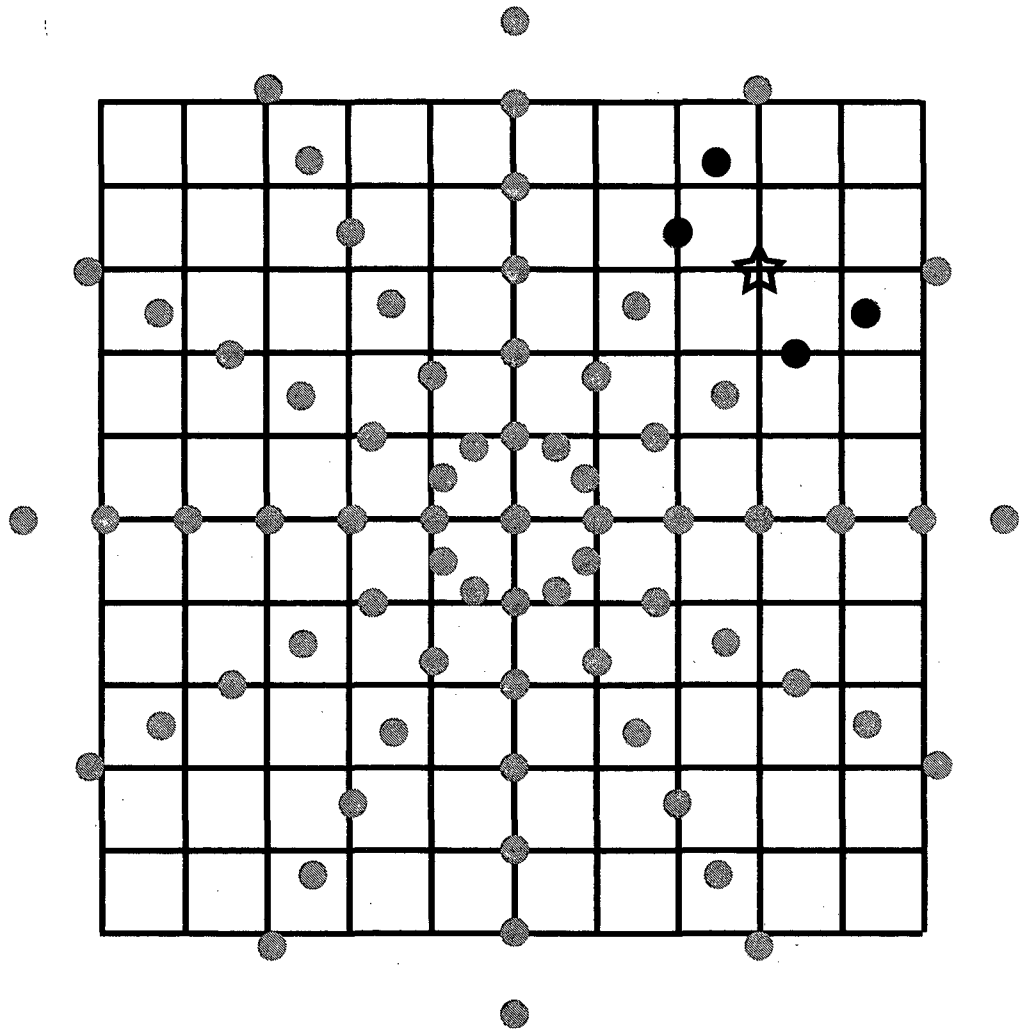

Figure 4.2. Polar to Cartesian Raster. The solid circles represent the polar raster of time space sitting in the regular Cartesian (square) raster. The four circles around the star are the four pieces of real data used to interpolate that point.

Cartesian point not on axis of a polar ray. Once the Cartesian time space was filled out, a two dimensional Fourier Transform produced the 2-D maps of nuclear density.

4.2.3 The SQUID Imaging Probe

Figure 4.3 is a photograph of the 1.5 m long low transition temperature SQUID probe. The important parts to take note of are the feedback electronics mounted to the brass flange at the top of the probe and the cylindrical lead shield at the bottom where the SQUID and the MRI probehead were housed. The long length of the probe was necessary since it was mounted to double nitrogen and helium glass dewars (Figure 4.4). Everything but the electronics were submerged in liquid helium. The dewar housing was a simple wooden cabinet. In order to further shield noise, there was a cylindrical mu-metal shield around the outside of the dewar in the region of the probehead, and the entire setup was locked into a copper mesh Faraday cage (screen room).

Figures 4.5 and 4.6 show two schematics of the same imaging probehead. Samples were required to have an outer diameter no larger than 8 mm and were tied to strings or sticks in order to put them in place in the probe and then pull them out again. The static field was supplied by a pair of rectangular coils 65 $\times$ 24 mm in a pseudo-Helmholtz configuration—pseudo because Helmholtz is a specific coil geometry with round coils whose separation is equal to the radius of the coils. Each coil was made of 30 turns of copper clad niobium-titanium (Nb-Ti) 26 gauge (AWG) wire. The gradient coils were a quasi Maxwell pair (a pair of counterwound coils), also rectangular 60 $\times$ 20 mm each made of 5 turns of copper clad Nb-Ti wire. The gradient coils were on axis with the static coils, so they produced a gradient dBz/dz. The gradient and static coils were run with persistent current charged by a Hewlett-Packard 6253A Dual DC Power Supply. Simple superconducting switches were built from insulated niobium wire, resistors, and epoxy. Superconducting connections were made by spot-welding the niobium wires to pieces of niobium foil and then covering them with epoxy to insulate and

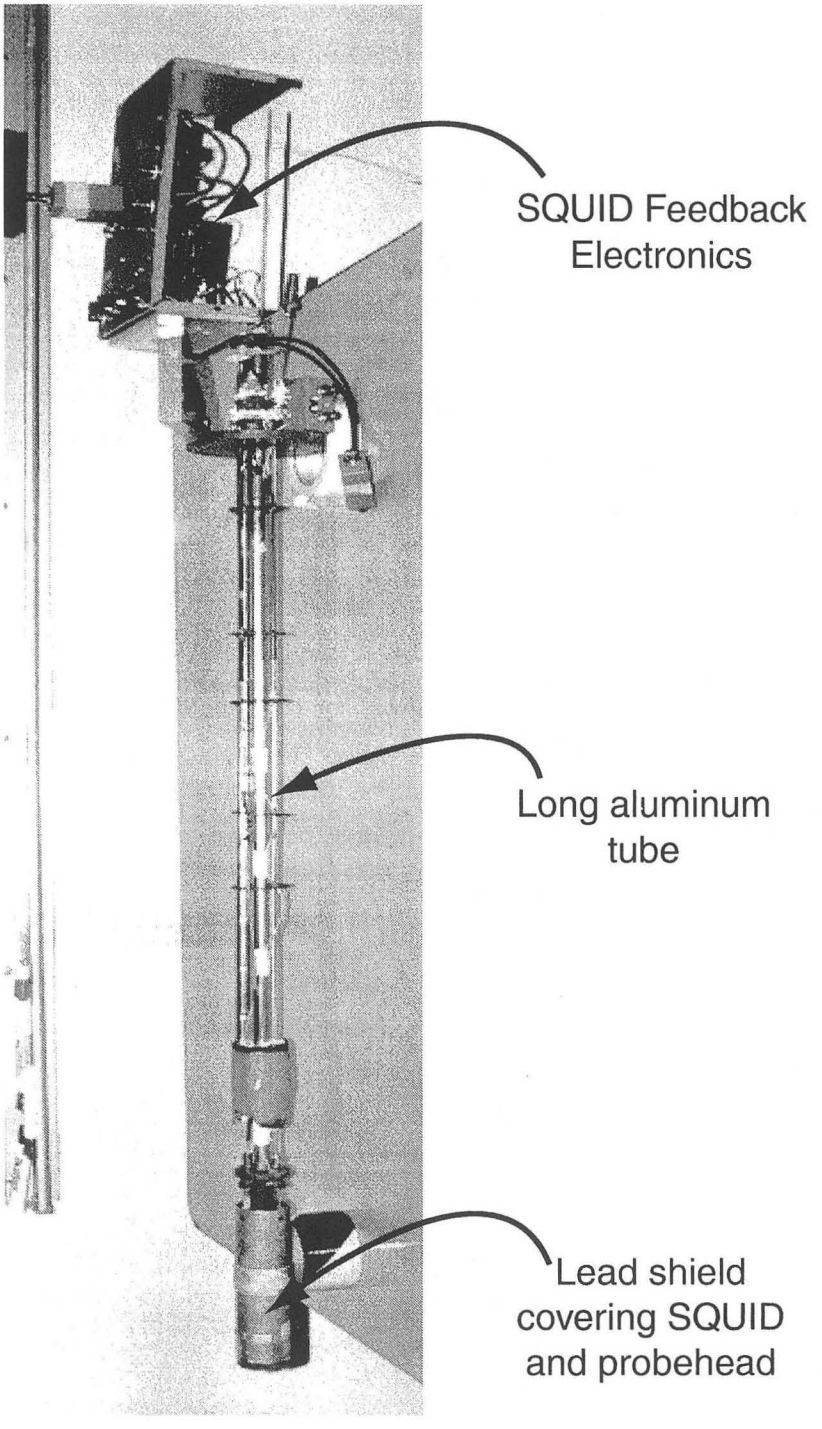

Figure 4.3. Low-T_C SQUID full-length probe

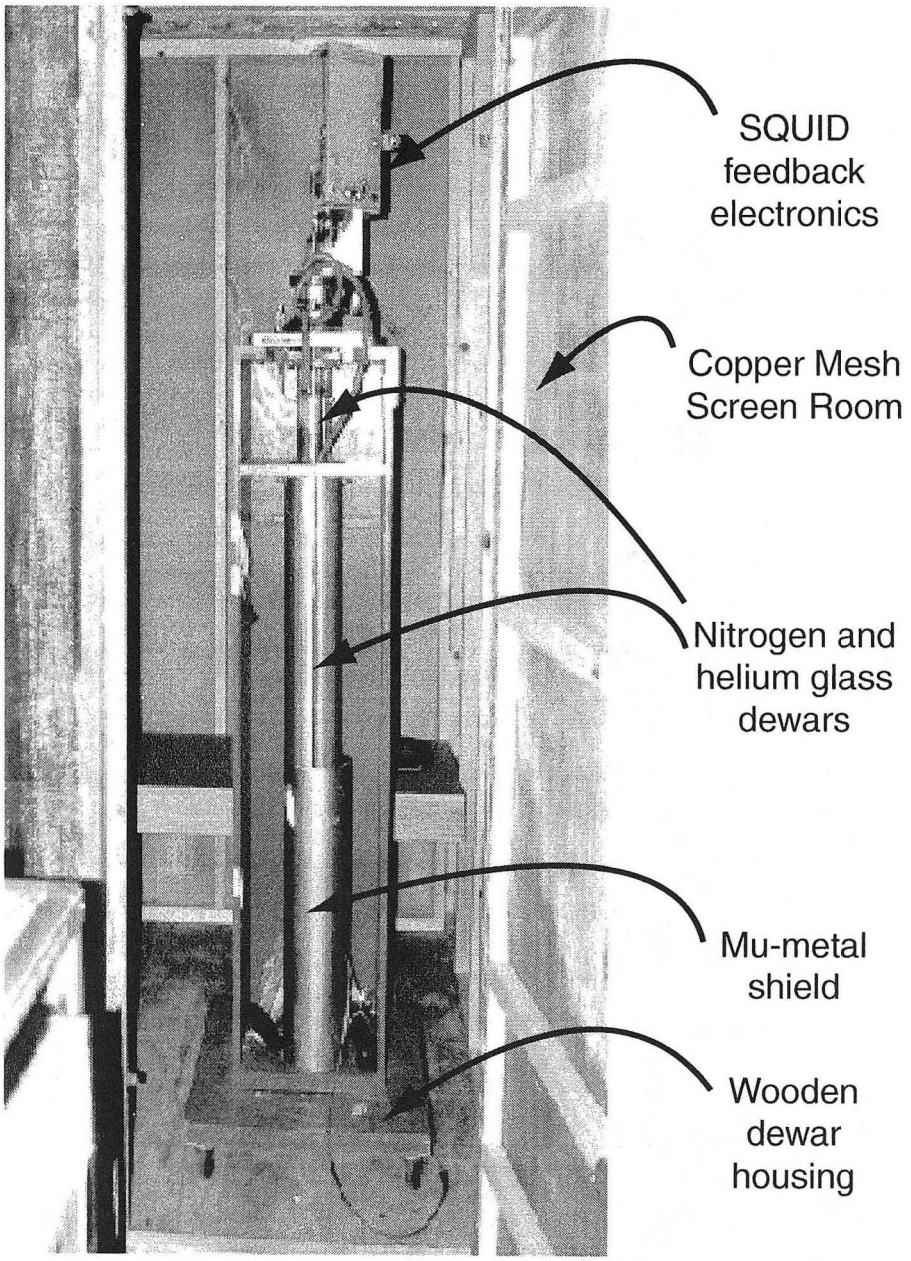

Figure 4.4. **The low-T_c SQUID dewar. The SQUID probe is inside the double nitrogen and helium dewars. The photo was taken through the open door of the copper mesh Faraday cage.**

protect the connections.

The audiofrequency (af) excitation coils were a pair of Helmholtz coils with a diameter and a separation of 15.6 mm. These coils were made of 20 turns of 26 AWG, insulated copper wire. The pickup coil was a 2 turn solenoid 9 mm in diameter and made of insulated niobium wire. It formed the flux transformer with the input coil patterned on the SQUID. The pickup coil was connected to the niobium foils on the G-10 fiberglass SQUID holder, see Figure 4.7, by pressure contacts made by sandwiching each wire between the niobium foil on the SQUID holder and a block of niobium (not shown in schematic) that was screwed to the fiberglass in order to squeeze the wire. The niobium foil pads were connected to the patterned input coil on the SQUID chip by ultrasonic wire bonds. Voltage and current connections were made by ultrasonically bonding aluminum wires from the on-chip contact pads to the copper contact strips on the fiberglass. The SQUID was epoxied to the holder and hermetically sealed by epoxying a fiberglass case on top. When sealed, the only parts exposed were the large niobium and copper contacts. A 10 turn copper coil for feedback was stuck to the outside of the fiberglass enclosure beneath the SQUID by Blue-Tack, a putty-like material similar in appearance to poster gum. Blue-Tack hardens at cryogenic temperatures but doesn't shrink much, doesn't crack and continues to adhere to the substrate. The SQUID holder with feedback coil is mounted inside a niobium cylinder to further shield the SQUID from noise, see Figure 4.5.

4.2.4 The Spectrometer

To run the imaging experiments we used a TecMag Aries interfaced to an Apple Macintosh IIci. The TecMag control software was MacNMR version 4.5.9. One TTL line from the Aries was used for the SQUID trigger to blank the integrator in the SQUID electronics (to prevent saturation as mentioned in Chapter 3). One TTL line was used to gate a Hewlett-Packard 3314A Function Generator. The output of this synthesizer was connected to a 10:1 voltage divider and then to the input of an ENI 1040L power amplifier (55 dB gain from 10 kHz to 500 kHz). The

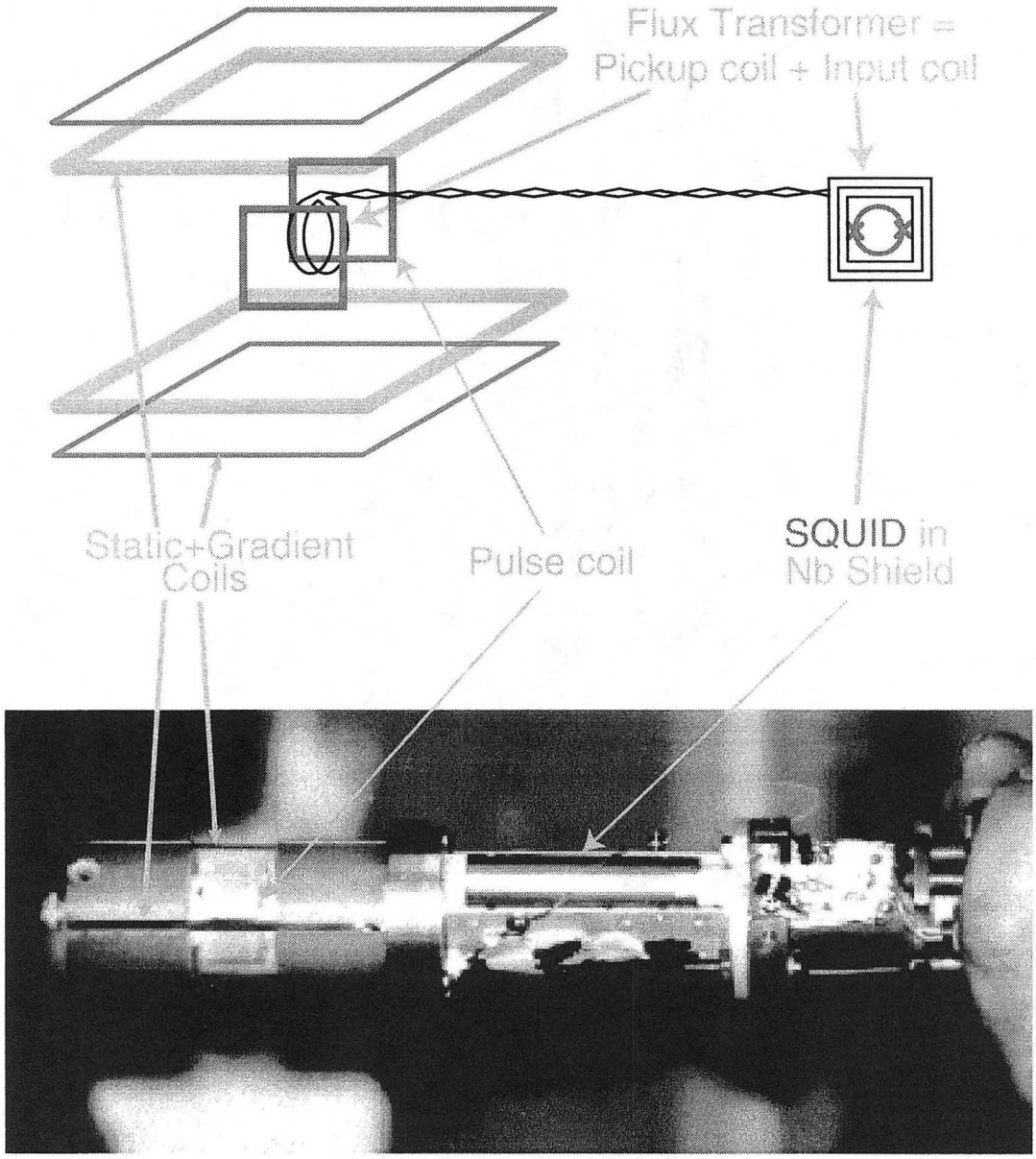

Figure 4.5. Low-T_c SQUID MRI Probehead (View 1). The flux transformer is not seen in the photograph since it is inside the probehead.

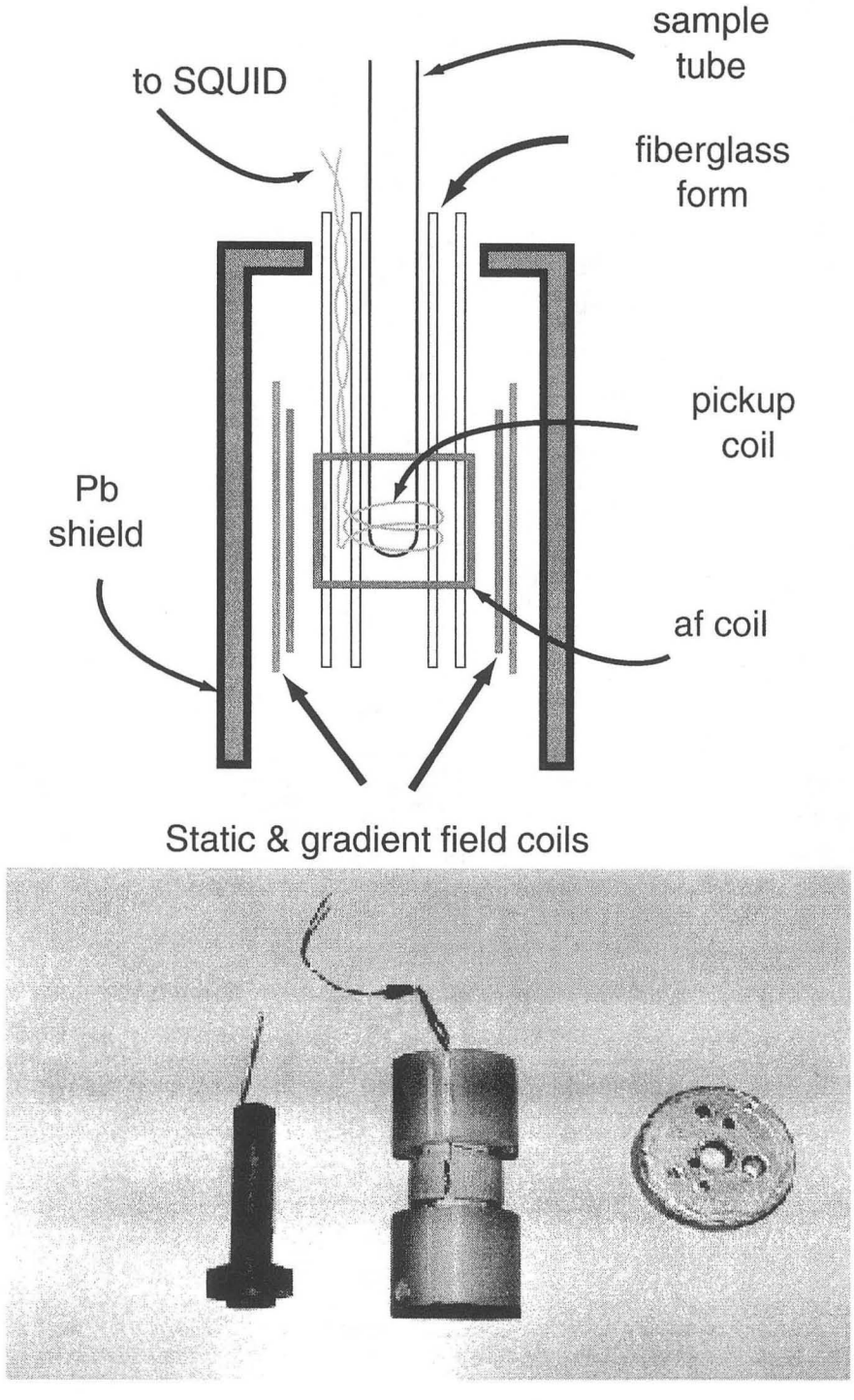

Figure 4.6. Low-T_c SQUID MRI Probehead (View 2)

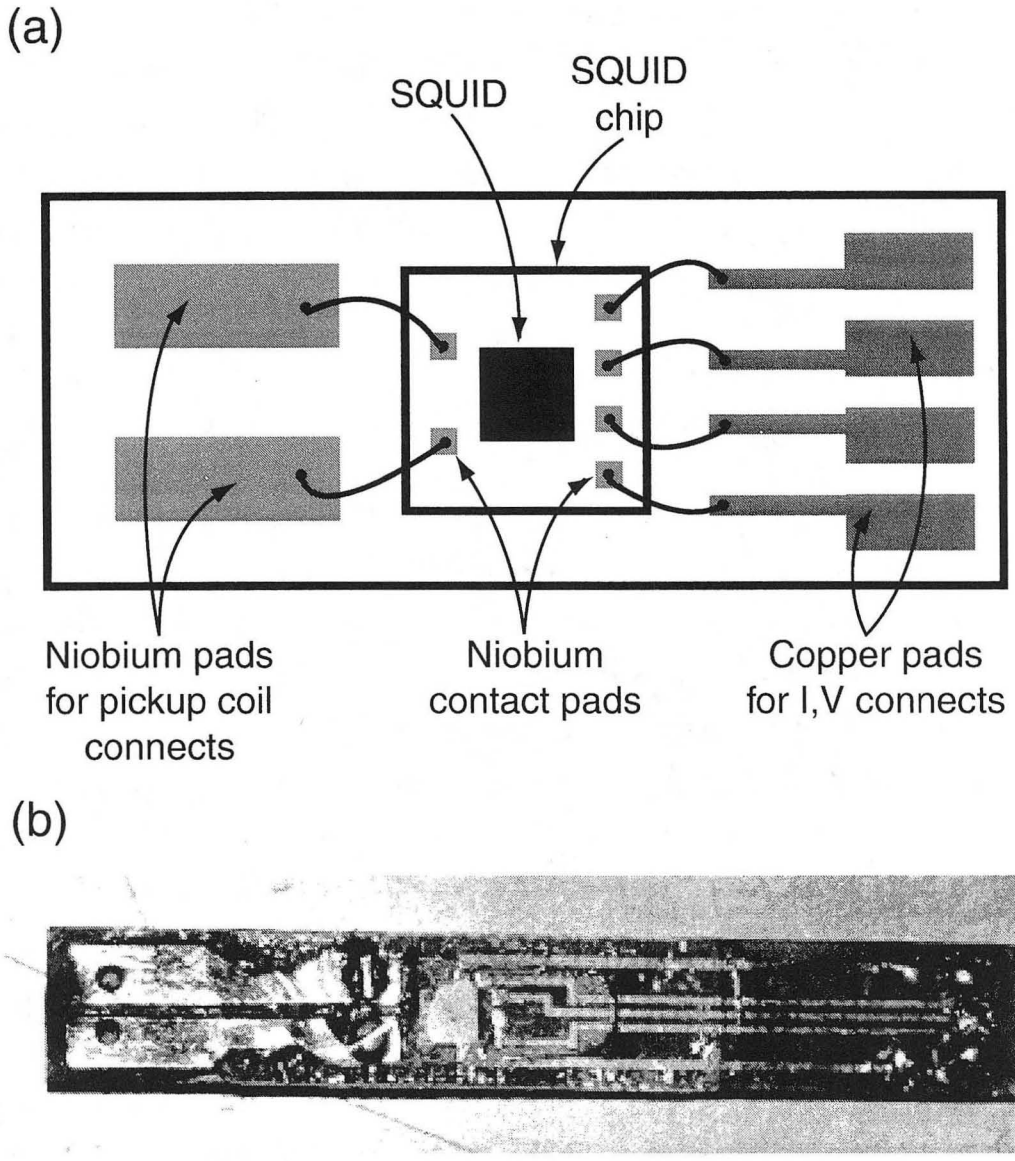

Figure 4.7. **Low-T_c SQUID Holder. (a) Schematic (not to scale) showing various connections from the SQUID chip to the niobium contact pads for the pickup coil connection and to the copper contact pads for the current and voltage connections. (b) Photograph of a fiberglass holder with no SQUID or connections.**

output of the amplifier was sent through two pairs of crossed diodes, through a 50 *ohm* resistor to match the output impedance of the amplifier, and then fed through the copper Faraday cage into the af excitation coil. The signal from the SQUID electronics was sent to a Princeton Amplifier Research (PAR) battery powered amplifier where it was low-pass filtered at 50 kHz and amplified by 20 dB. It was passed out of the SQUID cage to a Rockland Wavetek Model 442 filter where it was high-pass filtered and again amplified by 20 dB before going into the digitizer in the TecMag.

4.2.5 The Optical Pumping Setups

Our xenon sample was approximately 2 *atm* of naturally abundant xenon, 20 *mbar* of nitrogen gas, and a few milligrams of rubidium sealed in a cylindrical Pyrex cell with an inner diameter of 0.48 cm and length of 1.5 cm, giving a volume of 0.27 mL. One end was flattened while the other was pointed (from the sealing of the glass). The laser used to pump this sample was a 1 *watt* (W) titanium sapphire (Ti:Sapph) laser, model SEO Titan-Cw made by Schwartz Electron Optics, Inc., tuned to 794.7 nm pumped by a 10 W argon ion laser, model Innova 300 manufactured by Coherent. The beam from the Ti:sapph laser was passed through a quarter-wave plate to circularly polarize the light before entering the sample. The sample was heated to 400 K with a simple resistive heater made of nichrome wire mounted in a glass beaker. We pumped the sample for 5 minutes per run. One end of the cell was not optically clear (since it was not flat), so it was not possible to place the power meter behind the cell and tune the laser frequency by checking for light absorption as was typical procedure for flat-end pumping cells. Therefore we tuned by looking for the purple-white glow of the rudibium dimer fluoresence which one can see when the rudibium partial pressure is too high and nitrogen partial pressure (which quenches the fluoresence) is too low. Typical polarizations that we achieved were 3% as calibrated in a high field magnet against thermally polarized xenon. The coils that the sample sat in produced a magnetic field of 30 *Gauss* with a current of 15 amps. Figure 4.8 shows a schematic of the setup used

for the optical pumping of xenon. No mirrors are drawn in the diagram for the purpose of clarity, but they are in place wherever the light beams appear to bend.

The helium samples were cylindrical Pyrex cells containing 1 *atm* of 90% isotopically enriched ^{3}He, 11 *torr* of nitrogen gas, and a few milligrams of rubidium. The helium pumping cells each had an inner diameter of 0.68 *mm* and lengths of about 15 *cm*. Due to the length of the cell and the necessity for higher pumping temperatures (typically 473 K), we diverted the laser beam to the large blue Helmholtz coils with a diameter of 80 *cm* which produced a field of 30 G with a current of 15 *amps*. For heating, we tried using a resistive heater: nichrome wire wound around the sample, same as for the xenon. However, it proved to be inconvenient and time-consuming (as the polarization was relaxing) to quickly remove and insert the sample in the coil. Another method we tried was to use a heat gun to heat the sample. This turned out to be more convenient. However, we never observed large signals with the SQUID using either of these methods. We decided to use a high field magnet to check the polarization, and then further decided to modify the probe in order to optically pump the helium inside of the Pines Group "Delta" magnet (300 $MHz \simeq 7\ Tesla$). We used the Spectra Diode Labs SDL-8630 0.5 *watt* solid state diode laser and pumped the sample for half an hour inside the magnet. The beam was directed through the top of the magnet into the sample and was aligned by eye. In this case we heated only the bottom portion of the sample rather than the whole tube. The probe was a simple home-built "stick probe" with a small solenoidal heating coil and a saddle-shaped transmitter coil. Figure 4.9 shows a schematic of the optical pumping setup for the helium.

Mechanisms of optical pumping in high field are different than in the low fields (30 G) that are typically used. Spin exchange optical pumping in high magnetic fields was first investigated by Augustine and Zilm in 1996 [106, 107, 108]. Figure 4.10 shows the valence electron energy level diagram of rubidium in a field of 7 T. Note that this figure still ignores the difference between the two rubidium isotopes. The large splittings of the magnetic sublevels allows optical pumping selectivity based on light frequency as well as light polarization. It is not necessary to use

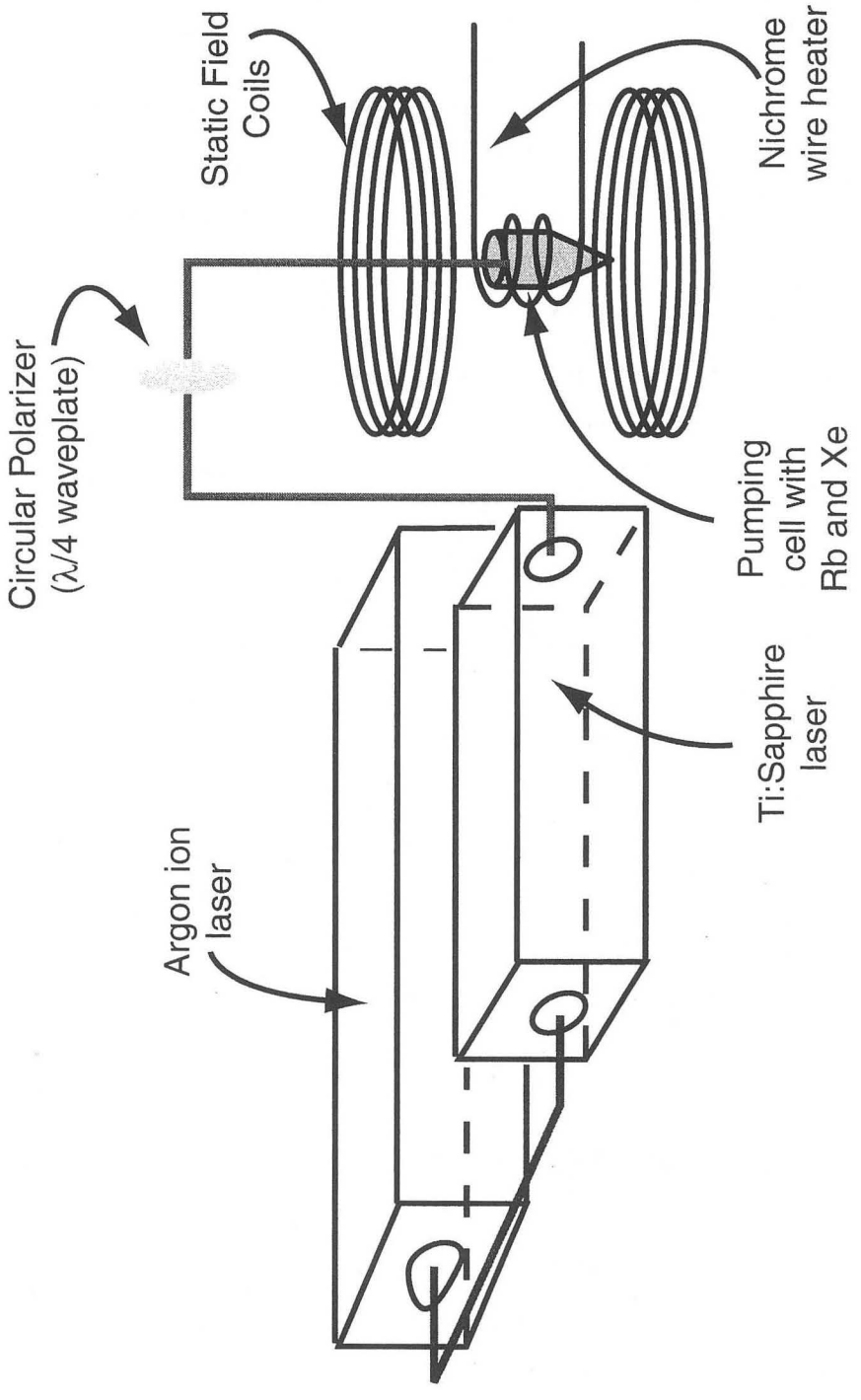

Figure 4.8. Xenon Batch Optical Pumping Setup. Not to scale.

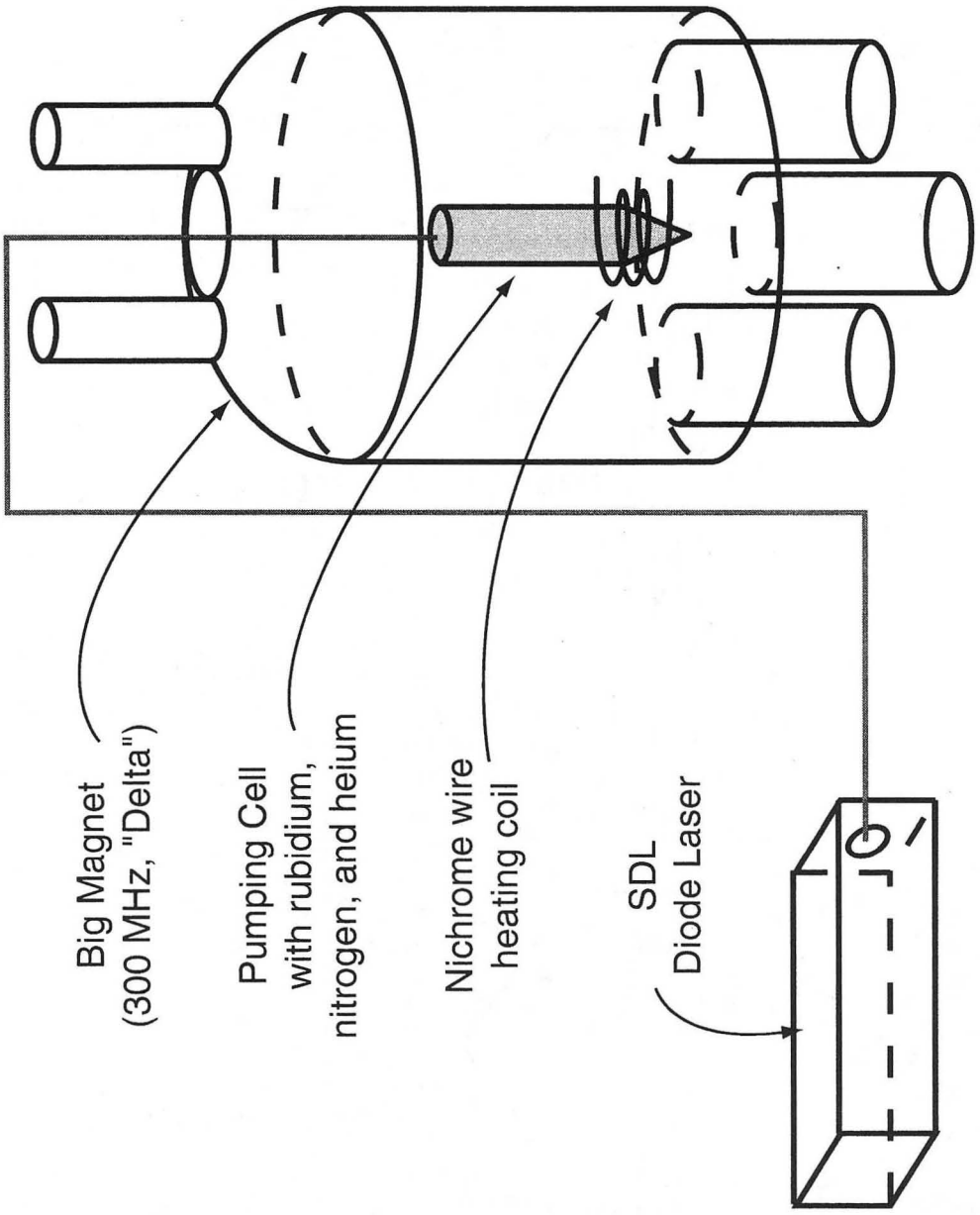

Figure 4.9. Helium High Field OP Setup. Not to scale.

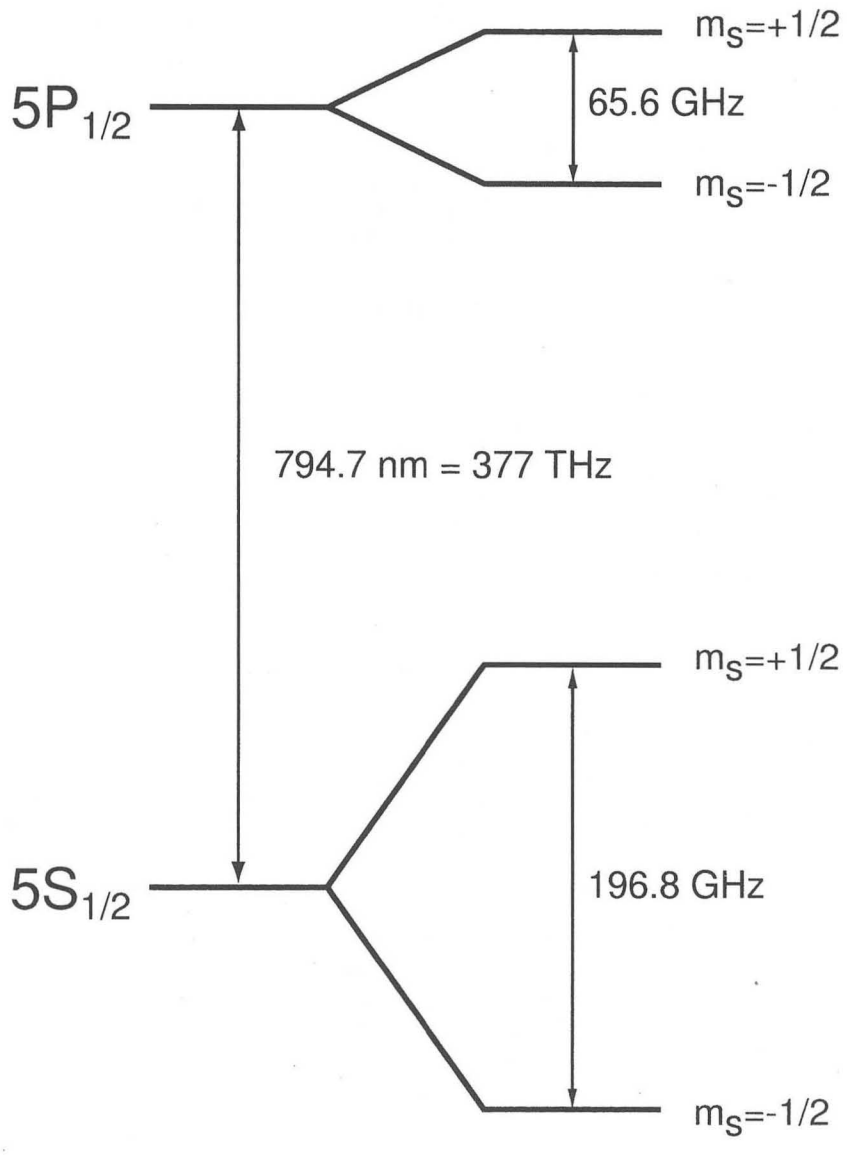

Figure 4.10. Valence electron energy levels of rubidium in a field of 7 *Tesla*.

circularly polarized light to optically pump the rubidium in high field [107]. Once the rubidium is spin polarized, the mechanism of spin transfer to the noble gas is similar to the mechanism at low field, as suggested by the measurements on spin-exchange cross sections between xenon and rubidium at high field [108].

4.2.6 The Images

Due to the long dead time of the SQUID electronics after the audiofrequency pulse, we used a simple 90-90 spin echo pulse sequence for all of the collections. Figure 4.11 is an example of the typical spin echo response. Each excitation pulse consisted of a single cycle with a magnitude of 0.09 mT at a frequency $\nu = 17.6$ kHz and were separated by 0.66 ms, leading to a refocusing of the magnetization at 1.32 ms. The helium 1-D time domain echoes were apodized by multiplication by hyperbolic secant functions centered at 1.32 ms and widths of 1.5 ms and then Fourier transformed. Three spectra are shown in Figure 4.12. All spectra were acquired in a static field of $B_\circ = 0.54$ mT, giving a resonance frequency of 17.6 kHz. The bottom spectrum (c) was produced with no gradient and shows a rather large 1 kHz $full\ width\ half\ max(fwhm)$ linewidth, most likely due to the inhomogeneity of $B_\circ$. The middle spectrum is a 1-D helium image with a gradient of $G = 0.33$ mT/cm and spatial resolution of 700 μm. The top spectrum was taken with a gradient of $G = 0.46$ mT/cm and a corresponding spatial resolution of 500 μm. The solid lines are the acquired data. The dashed lines in Figure 4.12(a) and (b) are the circular distribution functions that represent the expected density of a uniform material in a cylinder projected onto one axis. In other words, the spectral shape that you would expect from a applying a linear gradient to a cylindrical sample perpendicular to the axis of the cylinder. The dotted lines in 4.12(a) and (b) are the simulated 1-D images obtained by convolution of the circular distribution functions with a Lorentzian function describing the NMR lineshape.

The xenon data were acquired by sequentially rotating the sample tube in a static field of $B_\circ = 1$ mT, corresponding to a Larmor frequency of 11.8 kHz, and

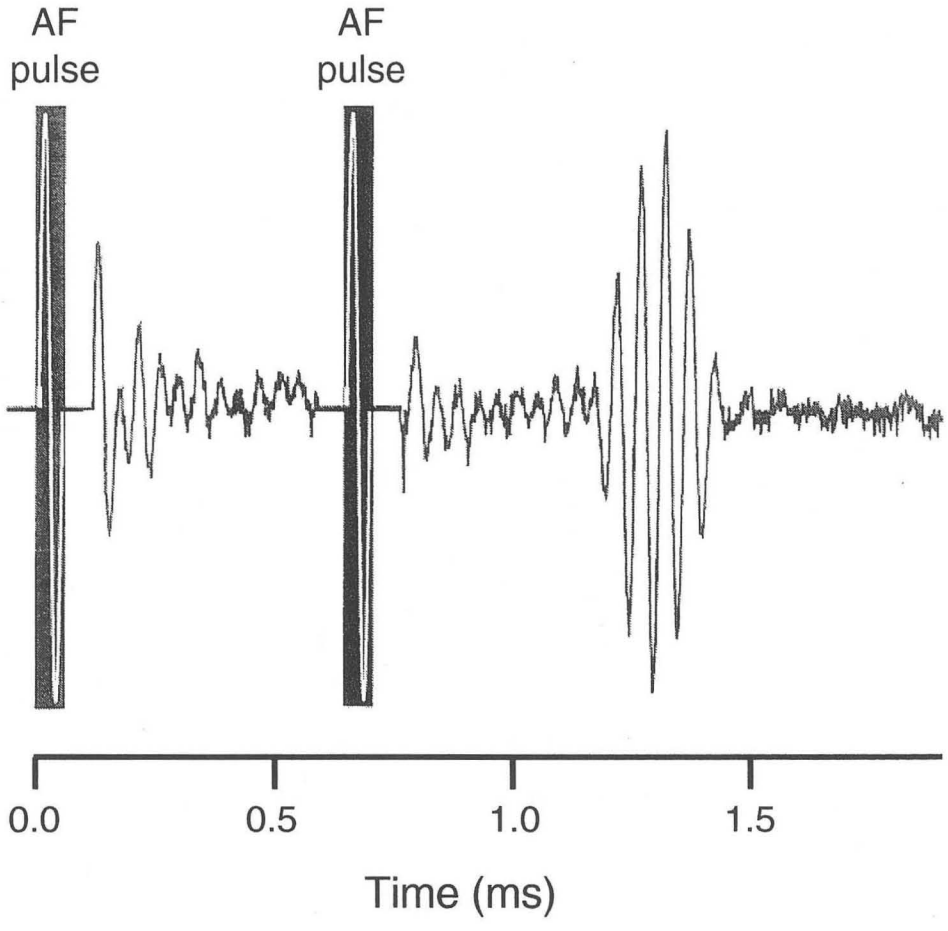

Figure 4.11. Spin Echo from Hyperpolarized Helium.

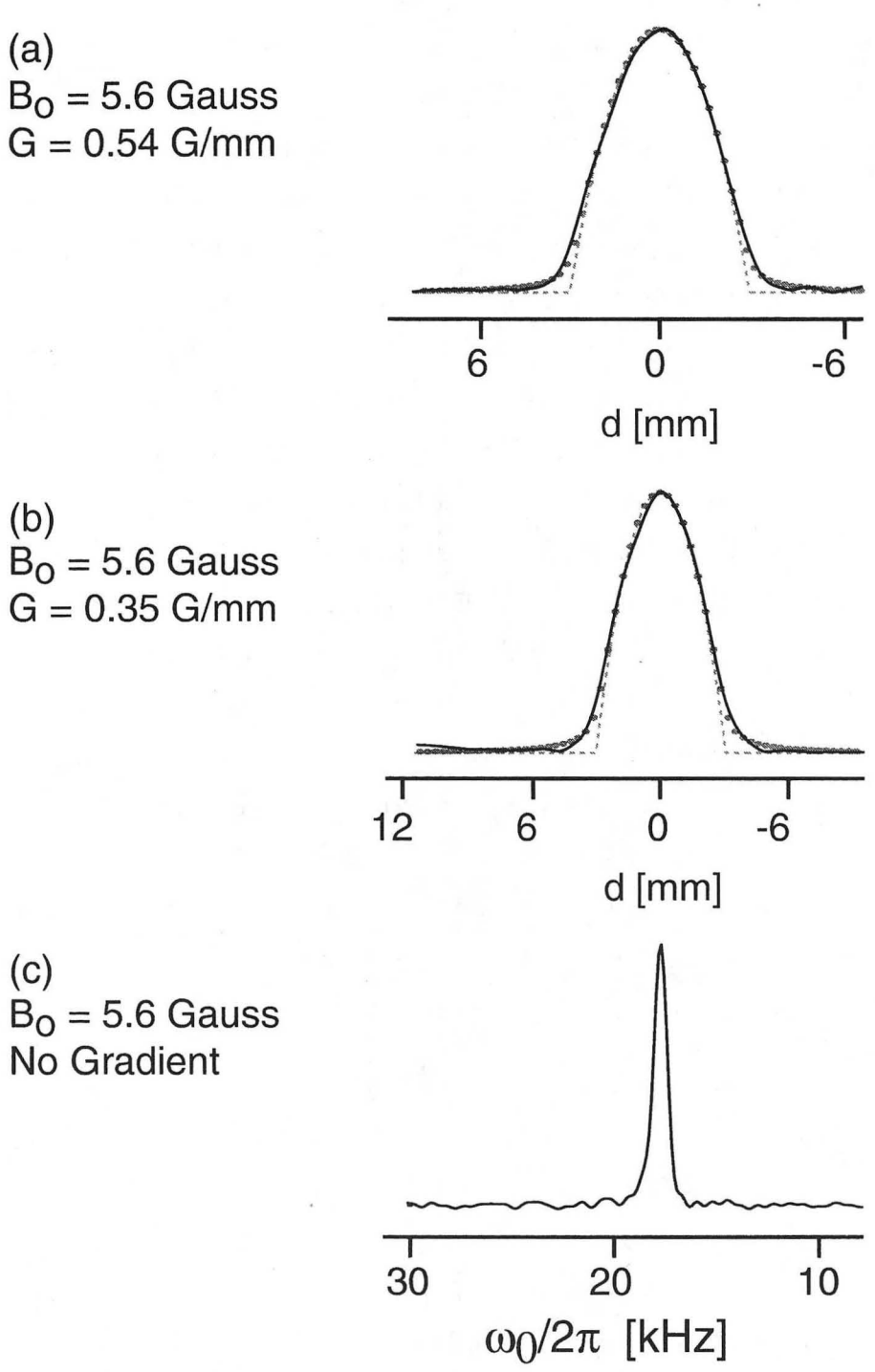

Figure 4.12. Hyperpolarized He 1-D Images

a fixed linear gradient $G = dB_z/dz = 0.46\ mT/cm$. A $\theta - \theta$ spin echo sequence was used with each af pulse giving a $\theta = 10°$ tipping angle. This 2-D data set required more signal processing than the helium single projections. We 2 times oversamples and collected 12 spectra each separated by 30°. We only needed 6 spectra separated by 30° to take the complete image because a gradient in the $+x$ direction contained the same information as a gradient in the -x direction—except that the two projections were mirror images of each other. Therefore we could not simply add spectra as one would for signal averaging. We cut each time domain signal at the top of the echo and threw away the beginning points to make 12 non-echo FIDs. We then arranged the 12 FIDs in a 2 dimensional polar time space where the origin corresponded to the start of each of the FIDs. Throwing away half of the echoes and reassembling the 12 spectra did not help us gain signal-to-noise, but it did allow for inhomogeneities in the gradient and static field to be averaged out that would otherwise distort the image. We normalized the intensities based on the maximum of each FID since each spectrum was progressively less intense as each pulse "destroyed" the nonequilibrium magnetizaton during acquisition. From the FIDs arranged in a radial pattern we interpolated the Cartesian space as described earlier in 4.2.2 and performed a 2-D Fourier transform to obtain the data in frequency space. And knowing the strength of the static gradient, G, and nuclear gyromagnetic ratio, γ, it is simple to convert the frequency, ν, axes to distance, D, axes.

$$D(cm) = \frac{\nu(Hz)}{\gamma\left(\frac{Hz}{T}\right) G\left(\frac{T}{cm}\right)} \tag{4.2}$$

Figure 4.13 shows the xenon "embryo" frozen to the side of the sample tube. Figure 4.13(a) is the actual data showing the pixel resolution. The picture is 30 points by 30 points giving approximately 1.2 cm on a side. Each pixel is approximately 0.4 mm wide, but because of the 520 Hz linewidth of solid xenon [109], the pixel resolution is better than the actual resolution of 950 μm. In this case the picture was resolution limited by the xenon linewidth. Figure 4.13(b) is the digitally smoothed version of the top image. Smoothing was done in Matlab by a method known as Gouraud shading which subdivides each pixel into many smaller pixels

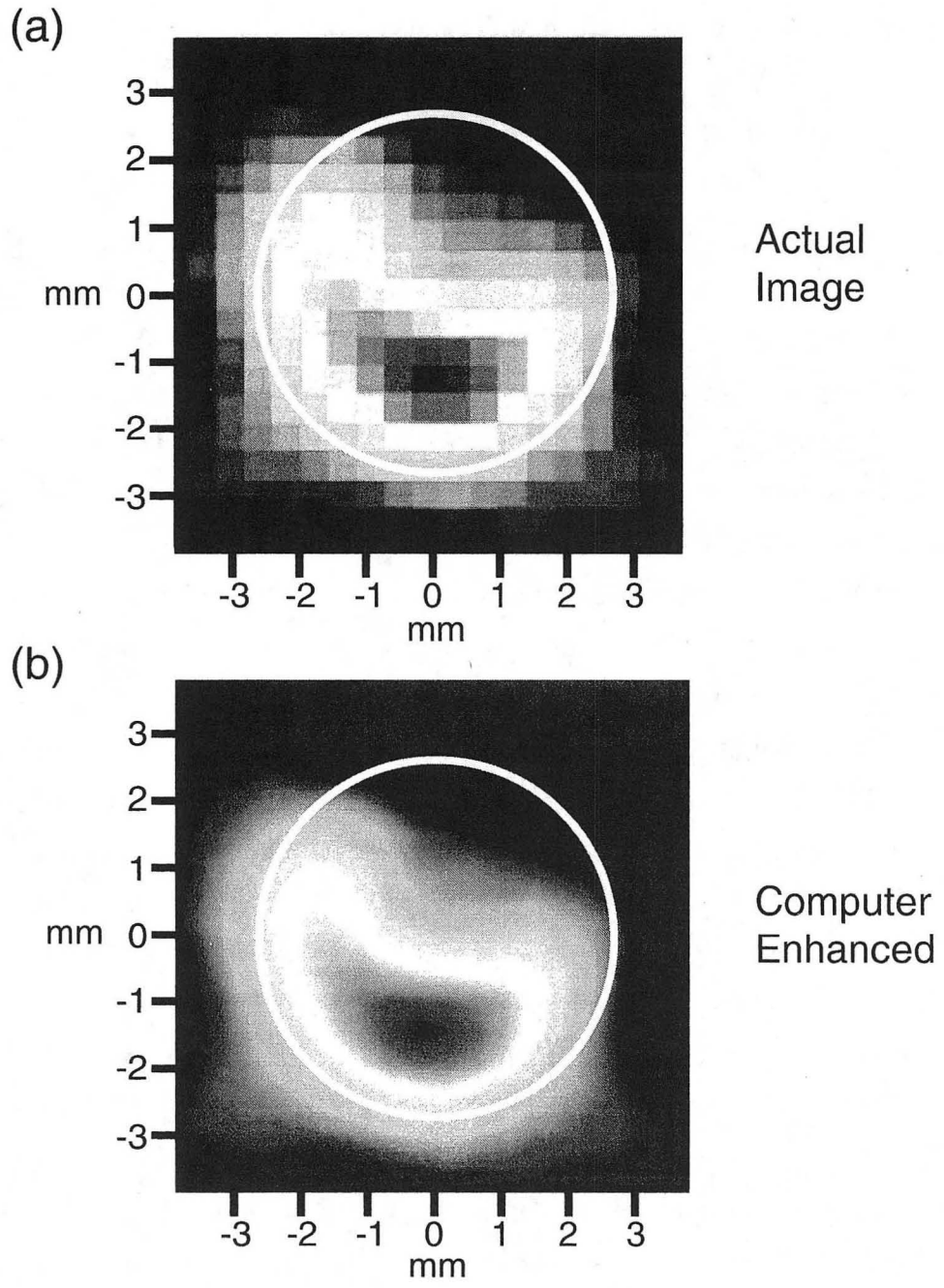

Figure 4.13. MRI of hyperpolarized xenon frozen to the side of a tube. Image taken with a static field strength of 1 mT and gradient strength of 0.46 mT/cm.

and linearly assigns a color to each subpixel based on the predefined colormap. Note that this was the "jet" colormap in Matlab. The white circle in both pictures represents the 4.8 *mm* diameter of the sample tube. The xenon density that extends beyond the white tube is caused by resolution limitations.

4.3 Pure Nuclear Quadrupole Resonance (NQR)

The history of nuclear quadrupole resonance dates to the 1940's with the molecular beam magnetic resonance experiment of Nierenberg, Ramsey, and Brody [110] based on the experiments by Rabi and coworkers in the late 1930's [111]. NQR was initially a method to simply measure quadrupole moments and to verify various aspects of the fledgling quantum mechanics theory. But it is a powerful analytical technique to gain physical and chemical information about molecules. More than $\frac{2}{3}$ of all elements have mainly quadrupolar isotopes, and the quadrupolar interaction is highly sensitive to the local electronic environment. High-field NMR of quadrupolar nuclei provides quadrupolar interaction information, but spectra can often be difficult to interpret due to the sheer number of lines and the NMR solid state powder pattern that could mask information. An alternative is zero field NQR, otherwise known as pure NQR.

The first pure NQR pulsed experiments were published starting in 1954 [112, 113, 114]. Although performed in CW mode, the next big evolution in NQR occurred in 1959 when Anderson applied the method of field cycling to quadrupolar metals [115]. The notion of field cycling had been introduced in 1951 by Ramsey and Pound [116] just after Pound had published his definitive work on NQR in crystals using a continuous wave technique [117]. The general idea behind field cycling is that the sample is first subjected to a strong magnetic field to polarize the nuclei. The field is then turned off allowing the nuclear interactions (such as the quadrupolar interaction) to evolve without the Zeeman interaction. The field is then switched back on to detect the magnetization.

Various field cycling methods have been developed such as "Double Resonance Lab Frame" [118, 119] and "Double Resonance Level Crossing" [120, 121, 122] with

perhaps some of the most elegant work done in the Pines group [123, 124, 125] with a method known as "Time Domain Field Cycling." But the problem with most field cycling experiments is that they are inherently 2-D experiments since the magnetization's slow precession cannot be detected directly: one dimension for the evolution in zero field of the quadrupole magnetization and the other dimension for the detection of the magnetization at high field. A SQUID, on the other hand, can detect the low frequency pure NQR magnetic resonances directly with high sensitivity, meaning simpler 1-D experiments. It should be mentioned that Tycko developed a clever technique in 1988 to perform zero field NQR in a high field magnet by spinning the sample and applying RF pulses [126, 127]. The advantage of using a SQUID for NQR compared to Tycko's method is that there is a fractional scaling factor for the magnetic interactions using his technique. There is already a growing body of work involving SQUID detected NQR [128, 129, 130, 131, 132, 133, 134, 135, 136, 137, 138, 139]. I present below the first pure NQR correlation spectrum using a SQUID taken with one directly detected dimension [139]. Note: yes I realize that I don't share authorship on the paper; these results were added to a review that was almost complete before the data was collected.

4.3.1 Pure NQR 2-D Correlation Spectroscopy of Aluminum-27 in Ruby

^{27}Al is a spin-5/2 nucleus, so in general there are six spin energy levels. Ruby is sapphire (Al_2O_3) doped with Cr^{3+}. In the crystal structure of Al_2O_3, each aluminum is octahedrally coordinated to six oxygen atoms. This high symmetry causes the six levels to become only three energy levels each doubly degenerate. It is easy to see this from the quadrupolar Hamiltonian:

$$\mathcal{H}_Q = \frac{-(eQ)(eq)}{4I(2I-1)} \cdot \left(3\hat{I}_z^2 - \hat{I}^2 + \eta(\hat{I}_x^2 - \hat{I}_y^2)\right) \tag{4.3}$$

This form of the Hamiltonian is different than that given earlier in Section 1.3.4 Equation 1.30. Though equivalent, this is perhaps more useful for magnetic resonance spectroscopy. eQ is the quadrupole moment magnitude of the nucleus, and

eq is the quadrupole moment magnitude of the interacting electric field gradient. In practice, the quadrupole coupling constant e^2Qq cannot be decomposed. The spin of the nucleus is given by I and the respective spin operators $\hat{I}$ and $\hat{I}_z$, $\hat{I}_x$, and $\hat{I}_y$. η is the asymmetry parameter of the electric field gradient, ranging from zero to one. A value of 1 corresponds to planar symmetry whereas a value of 0 corresponds to axial symmetry. For octahedral coordination, $\eta = 0$. This simplifies the Hamiltonian.

$$\mathcal{H}_Q = \frac{-(eQ)(eq)}{4I(2I-1)} \cdot \left(3\hat{I}_z^2 - \hat{I}^2\right) \tag{4.4}$$

$\hat{I}_z$ and $\hat{I}$ commute, so each matrix element of the Hamiltonian is given by:

$$\langle (m)|\mathcal{H}_Q|(n)\rangle = \frac{-(eQ)(eq)}{4I(2I-1)} \cdot \left(3m^2 - I(I+1)\right) \cdot \delta_{mn} \tag{4.5}$$

where δ_{mn} is the Kronecker Delta function. States $|(m)\rangle$ and $|(-m)\rangle$ have the same energy, so integer spin nuclei have a nondegenerate ground state $|(0)\rangle$ and all other states doubly degenerate. Half-integer spin quadrupolar nuclei have $(2I + 1)/2$ doubly degenerate energy levels. For spin-5/2 nuclei like aluminum, this corresponds to two allowable transitions: between the $|(\pm 1/2)\rangle$ and $|(\pm 3/2)\rangle$ levels and the $|(\pm 3/2)\rangle$ and $|(\pm 5/2)\rangle$ levels. For sapphire, those transitions have energies corresponding to the frequencies 359 kHz and 714 kHz respectively. Figure 4.14 shows a spectrum of the ruby sample with both transitions irradiated. The sample was composed of 500 mm^3 of ruby in the form of little ruby spheres with 0.5 mm diameters. The chromium dopant level was 7%. Doping sapphire with Cr^{3+} not only makes the balls a pretty red color, the paramagnetic impurity also significantly shortens the T_1 (longitudinal relaxation) of the aluminum. The T_1 of pure sapphire at 4.2 K is 1 minute. In contrast, the 7% chromium dopant level cut the T_1 to approximately 10 ms.

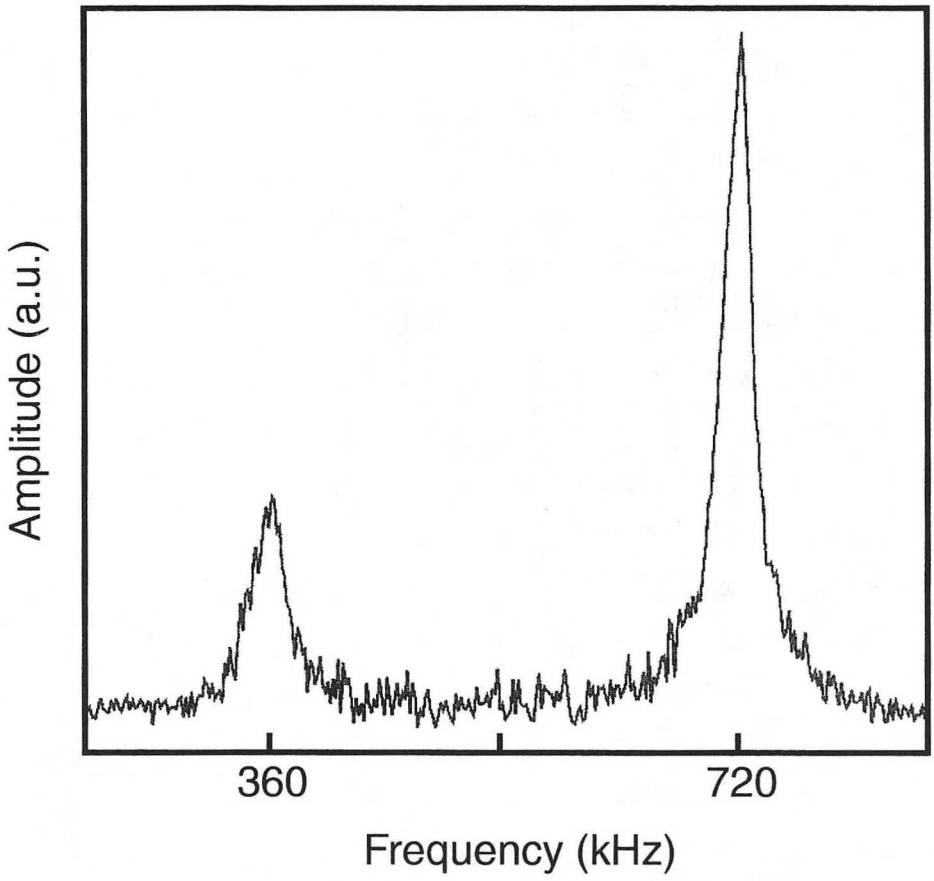

Figure 4.14. NQR Spectrum of ^{27}Al in Ruby. Both transitions were irradiated.

4.3.2 The NQR Probe and Spectrometer

Figure 4.15 shows a schematic of the NQR probe. The pickup coil was a four turn axial gradiometer. The pulse coil was a two-layer solenoid 15 mm in diameter and 30 mm long. It was wound with 28 AWG copper magnet wire (formvar insulation) on a Rulon form. Rulon is a material composed of paper compressed with plastic. There was a superconducting lead shield around the whole probehead to shield all external fields. It was important to balance well the gradiometer in the AF coil—in other words, position the gradiometer for maximum signal rejection from the AF coil. This could be achieved by sending a signal (100 kHz from a function generator) into the AF coil and connecting the ends of the gradiometer to a good scope, such as the Hewlett-Packard 3561A Dynamic Signal Analyzer. The Signal Analyzer was useful since it carried out a real-time Fourier Transform to easily track the amplitude of the signal that was being sent to the AF coil. By moving the gradiometer on its Rulon form relative to the AF coil (see exploded view of the probehead in Figure 4.15), it was possible to balance the gradiometer to better than 0.1% (10 mV pickup from 10 V input at 100 kHz).

These NQR experiments did not use the TecMag Aries. We had been using an old version of MacNMR (v.4.5.9) since newer versions did not run on the old Macintosh IIci. It did not perform the collection and file-save options that we wanted. We felt that we could easily put together a spectrometer that would do exactly what we wanted. The pulse timer that we used was a Stanford Research Systems Model DG535 Four Channel Digital Delay/Pulse Generator. One TTL line from the gated output (i.e. A-B or C-D rather than A, B, C, or D) was used to trigger the SQUID. The other gated TTL line was split to the external trigger inputs of two Hewlett-Packard 3314A Function Generators, one tuned to 360 kHz and the other tuned to 720 kHz. The function generator outputs were mixed with a simple 10:1 voltage divider and connected to the input of an ENI 1040L Power Amplifier. The output of the amplifier was passed through two pairs of crossed diodes and a 50 Ω high power resistor before it was fed through the Faraday cage to the pulse coil. Output from the SQUID electronics went to a Princeton Amplifier

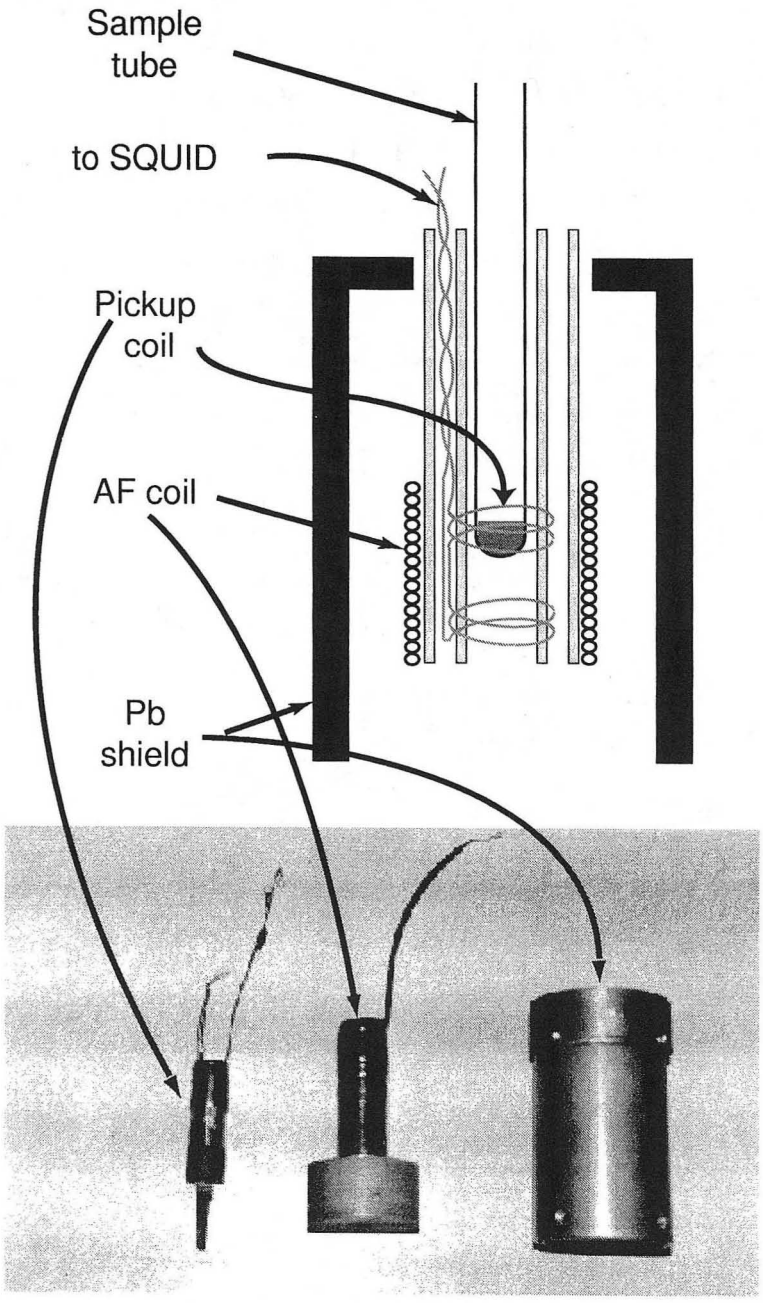

Figure 4.15. Schematic and photograph of the low T_c SQUID NQR probehead. Photograph shows disassembled view. This probehead replaces the MRI probehead on the long SQUID probe.

Research filter where it was amplified by 20 dB. The signal was then passed out of the Faraday cage and put through one channel of a Rockland Wavetek Model 442 Filter. The signal was then digitized by a Tektronix DSA 602 Digitizing Signal Analyzer with 11A72 Two Channel Amplifier (the input module). An Intel 486-DX25 (25 MHz processor) based PC was outfitted with a National Instruments IEEE-488 communications card to interface the computer to the pulse generator and digitizing scope. The IEEE-488 (also called HPIB) interface allows the daisy-chaining of devices, so only one interface card in the computer was required to control multiple instruments. I wrote a simple Instrument BASIC (I-BASIC) program to fully automate data collection. It controlled and synchronized both the Stanford pulse programmer and the Tektronix digitizing scope. After each NQR scan, it automatically downloaded the data from the Tektronix digitizing scope and saved it in a simple text file to be read into Matlab.

4.3.3 Results: 2-D Ruby Spectrum

The pulse sequence used for the 2-D collection is shown in Figure 4.16. The second pair of pulses mixes the spin populations after the time τ_1. By taking NQR spectra with different values of τ_1 we can resolve the resonance correlation that is caused by the mixing. The step size of the time τ_1 (coherence mixing time) between acqusitions was 0.5 μs. The 2-D data set was composed of 64 FIDs each averaged 512 times. The data in Figure 4.17 clearly shows two diagonal peaks corresponding to the 359 kHz and 714 kHz transitions. But there are also cross peaks indicative of the coherence transfer between the magnetic resonances. The weakest signal in the map is the on-diagonal low energy transition ($|(\pm 1/2)\rangle$ to $|(\pm 3/2)\rangle$), and the strongest signal is from the on-diagonal high energy transition ($|(\pm 3/2)\rangle$ to $|(\pm 5/2)\rangle$).

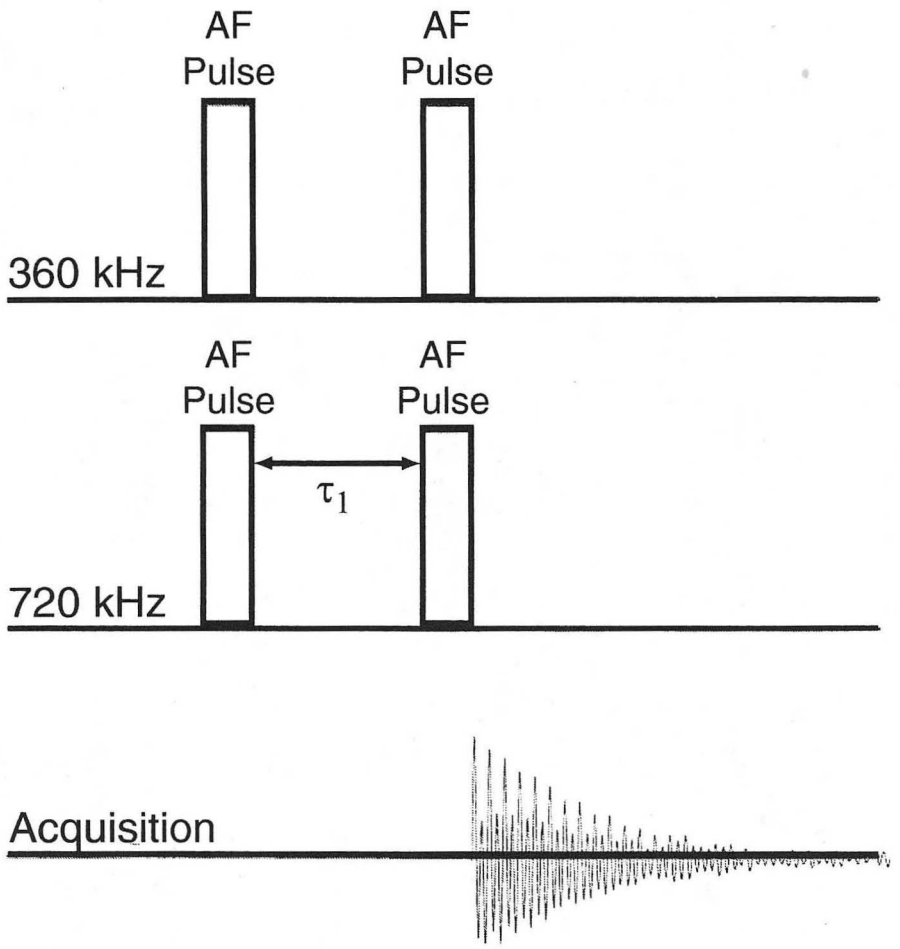

Figure 4.16. **Pulse Sequence for 2-D NQR of Ruby. The sequence shows the two frequencies irradiated simultaneously. The time τ_1 was incremented by 0.5 μs between scans.**

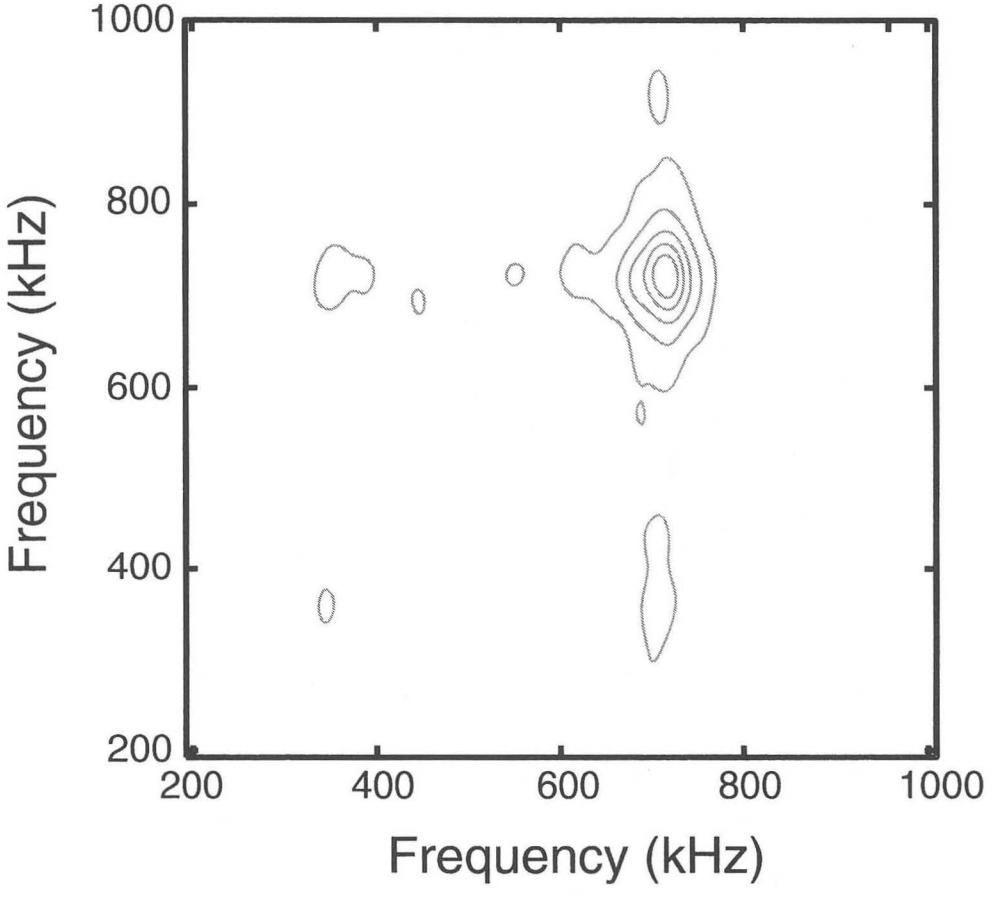

Figure 4.17. **2-D Pure NQR of ^{27} in Ruby. The off-diagonal peaks indicate magnetization transfer between the two resonances.**

Chapter 5

High Transition Temperature SQUIDs

5.1 Introduction

There were two main reasons for the move from using a liquid helium low-T_c SQUID to using a high-T_c device that would operate at liquid nitrogen temperature. The first was that our low transition temperature SQUID setup suffered from a serious handicap. It operated cold and required that samples also be cold. One problem with this limitation was that there were no good "standard samples" for 4 *Kelvin* operation in order to tune or trouble-shoot the probe. Good NMR standards like water have intolerably long relaxation times in the solid state sitting in liquid helium. The second reason was that while we were taking pictures with the highest resolution at the lowest fields, imaging objects in an 8 mm hole at 4.2 *Kelvin* was not the most widely applicable technique. So we wanted room temperature samples, and while it would have been possible to build a probe to insulate the 4.2 K SQUID from a room temperature sample [140, 141, 142], using the new high-T_c SQUIDs would greatly simplify the cryogenics [143]. After the high-T_c setup was completed, however, it was clear that it did not have the sensitivity to take the hyperpolarized xenon images that we wanted. We were able to take proton MRI pictures at fields of 2 mT, corresponding to a Larmor frequency of

87 kHz. But for gas imaging, we needed another upgrade: a continuously flowing optical pumping system.

In this chapter I describe first the high-T_c SQUID MRI system and the proton spectra and proton images that were acquired. I then detail the subsequent spectrometer improvements that gave us pulsed gradient capability. With pulsed gradients we were finally able to use modern imaging pulse sequences and more importantly, we could image without having to rotate the subject. This chapter also contains a description of the new flowing optical pumping system and the hyperpolarized xenon images that we were able to acquire. The last part of the chapter is devoted to the low field spectroscopy using the high-T_c SQUID detector. The work in this chapter was mostly published [144, 145, 146, 147, 148].

5.2 The SQUID Dewar

Just before we had completed the first hyperpolarized xenon, SQUID detected MRI, Lee and coworkers in the Clarke group had designed a dewar for high critical temperature SQUIDs that seemed like the perfect design for our purposes [149]. This so-called "SQUID Microscope" would allow one to bring a warm (room temperature) sample in very close proximity (less than 1.5 mm in our case) to the cold SQUID. Figure 5.1 shows a schematic of the design, and Figure 5.2 is a picture of the dewar.

The outer enclosure was made of G-10 fiberglass approximately 1 cm thick and coated with epoxy (clear Stycast 1266A & B) to prevent gas diffusion through the porous fiberglass. There was a 1 *liter* brass can inside which held the liquid nitrogen. Mounted just beneath the can was an aluminum plate onto which charcoal was glued as a dessicant. Also on the plate was a nichrome wire resistive heater to bake out the charcoal. There was also a nichrome heater around the brass can. The brass can was held in place by three rods screwed to the top of the fiberglass dewar. Also mounted to the top of the can was a copper rod 1 cm in diameter. It projected into the dewar so that it was always partially submerged in the liquid nitrogen. The part of the rod extending out of the can was clamped to a 10 cm

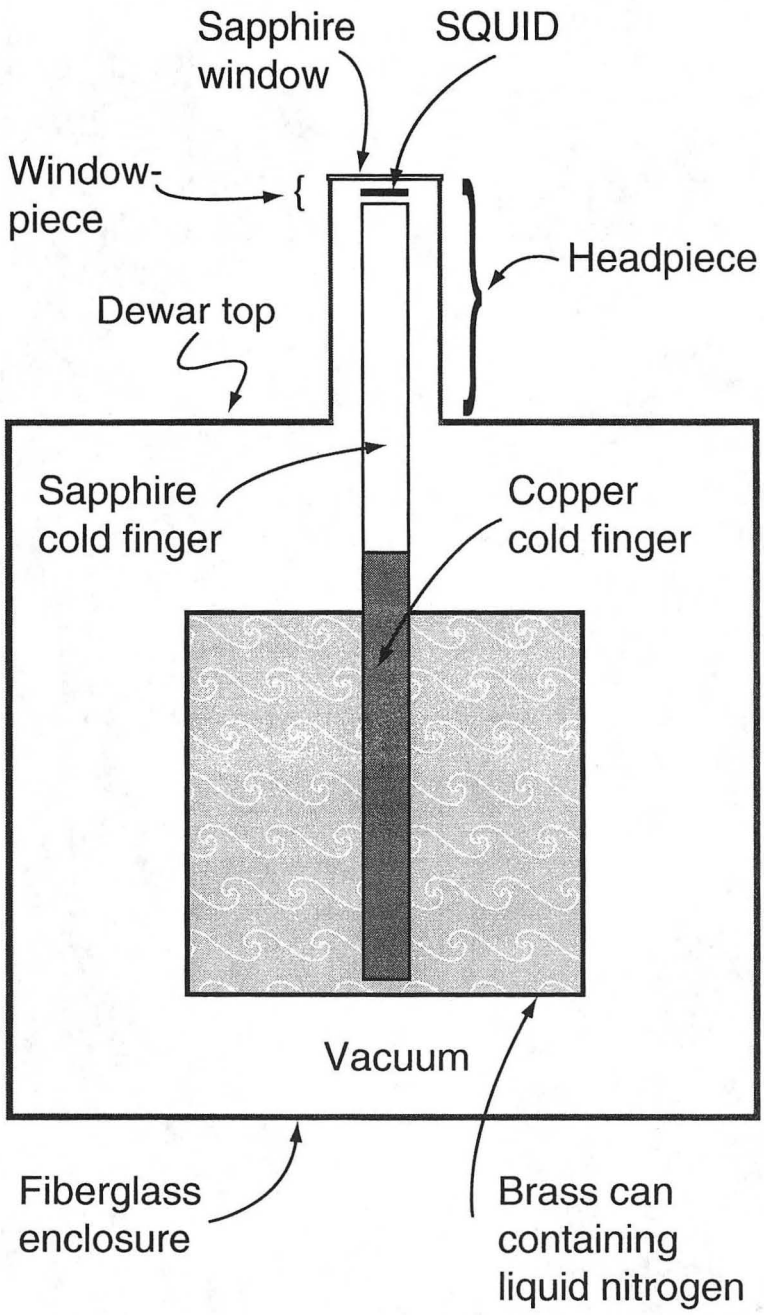

Figure 5.1. **Schematic of dewar for high-T_c SQUID. The SQUID is shown "floating" for clarity. In reality, it is stuck to the sapphire rod.**

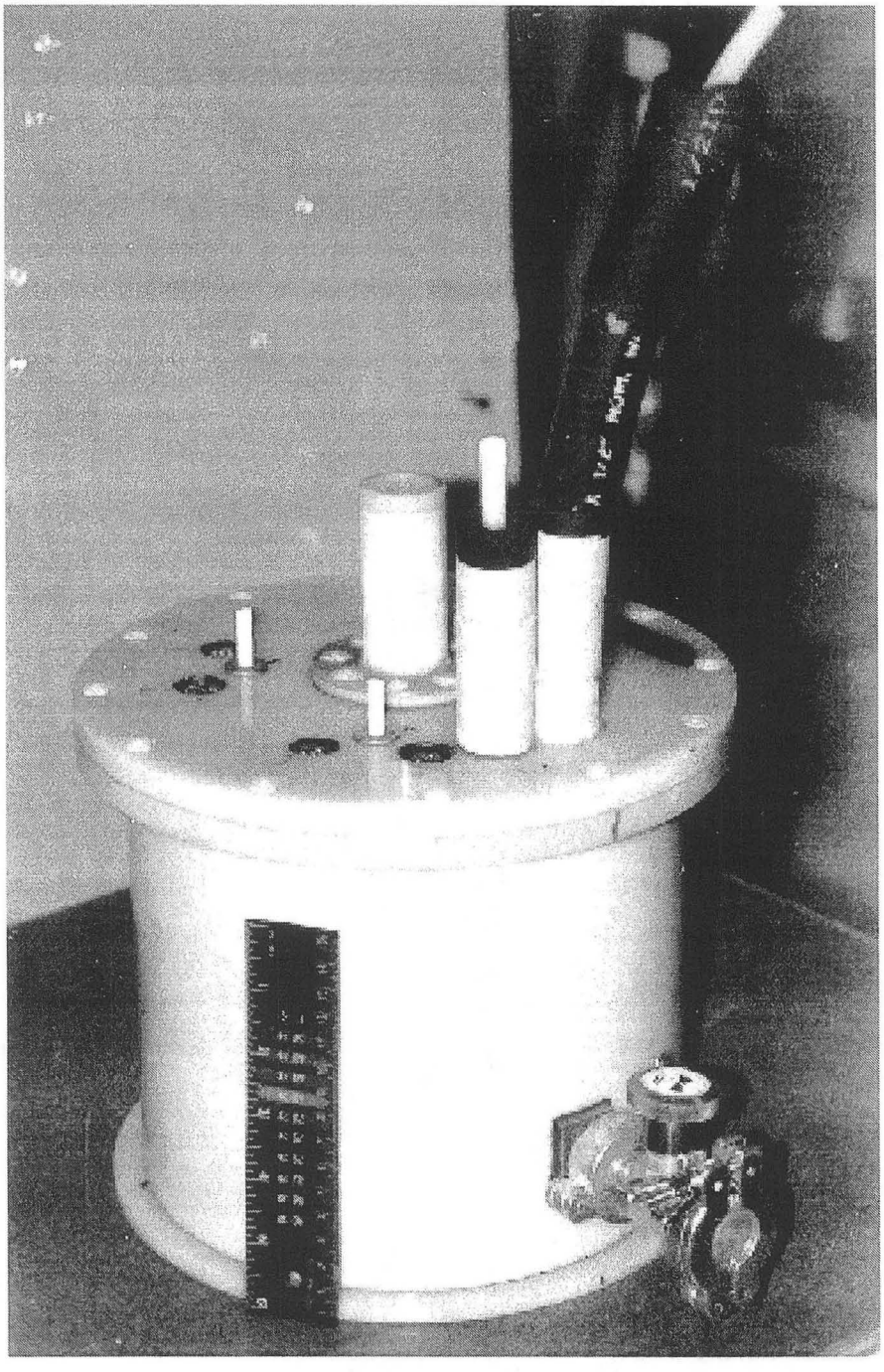

Figure 5.2. Photograph of dewar for high-T_c SQUID. The fill tubes are prominently displayed jutting from the top of the dewar.

long sapphire rod (Al_2O_3 single crystal) also 1 cm in diameter. The SQUID was mounted on top of this rod. We found that the best compound to stick it in place and have good thermal contact was Apiezon N high vacuum grease. Wrapped around the sapphire rod just beneath the SQUID were a one-turn feedback coil and a two-turn feedback coil used for the flux-locked loop. The externals of the dewar were all fiberglass except for the window directly above the SQUID. It was a 3 mil (0.003 in = 762 μm) thick sapphire plate, 2.5 cm in diameter. The fiberglass top was sealed to the dewar bottom with either a large Viton or Buna o-ring and held in place by nylon screws. Likewise the headpiece (the fiberglass that covered the sapphire rod) was sealed to the top by an o-ring and held by nylon screws. The window was epoxied to a window-piece which was made of fiberglass and inserted into the headpiece and sealed with an o-ring. There were also three or four layers of aluminized mylar (superinsulation like that inside the vacuum space of superconducting magnets) covering the brass can and cold finger for radiation shielding. Figure 5.3 is a photograph of the headpiece showing the clear sapphire window and the SQUID (square object inside the cylinder). The gray and black objects on the very right of the photo are the liquid nitrogen fill tubes. Figure 5.4 is a photograph showing the internals of the dewar. Mostly visible are the mylar superinsulation, the dewar's fiberglass top, and the mylar covered sapphire cold finger.

Electrical connectors were epoxied to the fiberglass top as well as two nitrogen fill and vent tubes (not shown in the diagram). There were four connectors: the first comprised the voltage and current connections to the SQUID as well as leads to the feedback coil; the second provided connections to the second feedback coil (originally planned for use as the Additional Positive Feedback (APF) coil, see references [150, 151] on APF) and to the "PT100" platinum resistor mounted at the top of the sapphire rod close to the SQUID for monitoring temperature. The third connector contained contacts for the two platinum resistors mounted on the brass can and on the charcoal plate; and finally the fourth connector for the three heating coils. The heating coils were driven by a simple Variac.

The first dewar connector was routed through a simple switch box before con-

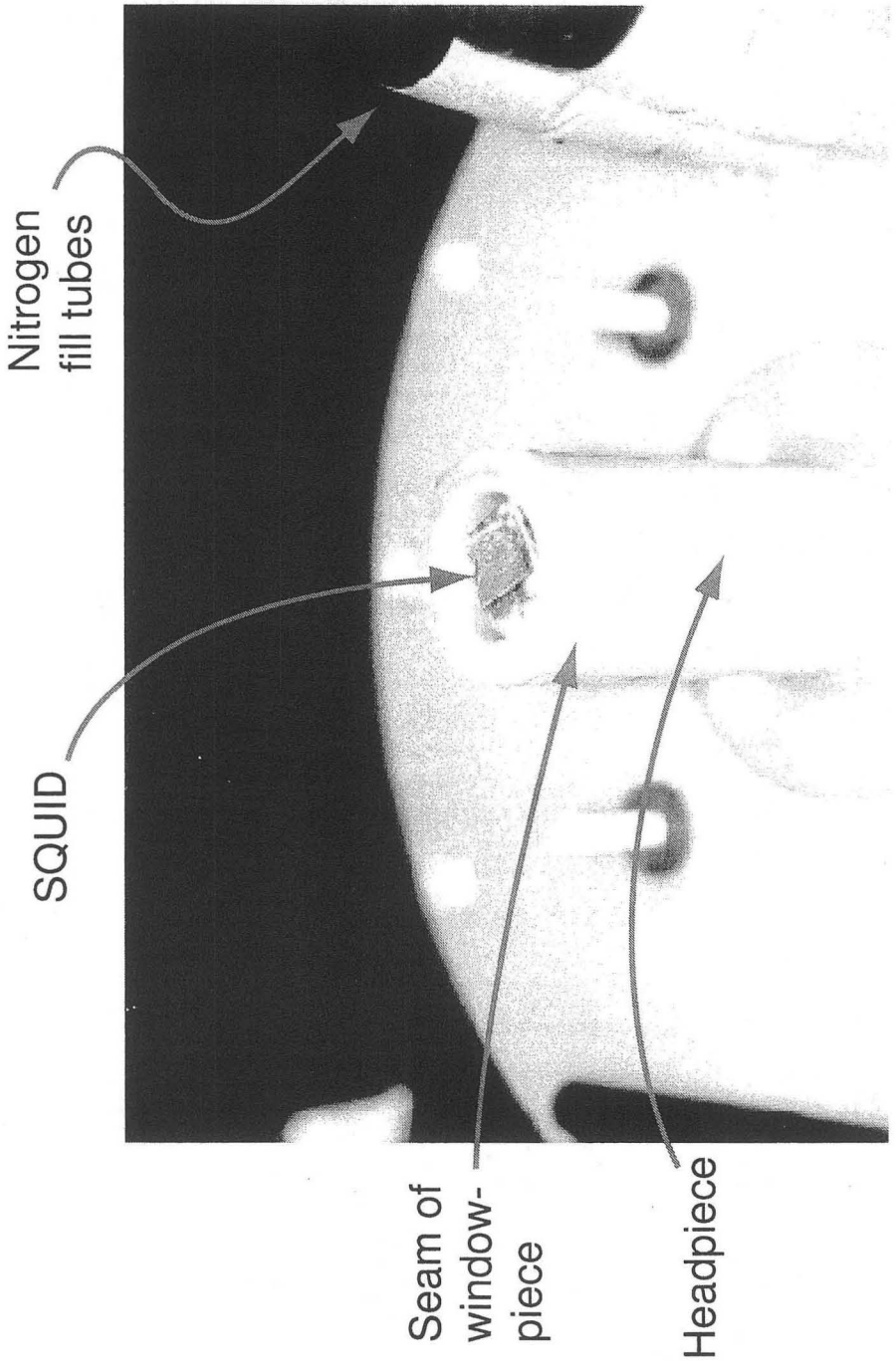

Figure 5.3. Photo of the Dewar Headpiece. The SQUID is visible through the clear sapphire window.

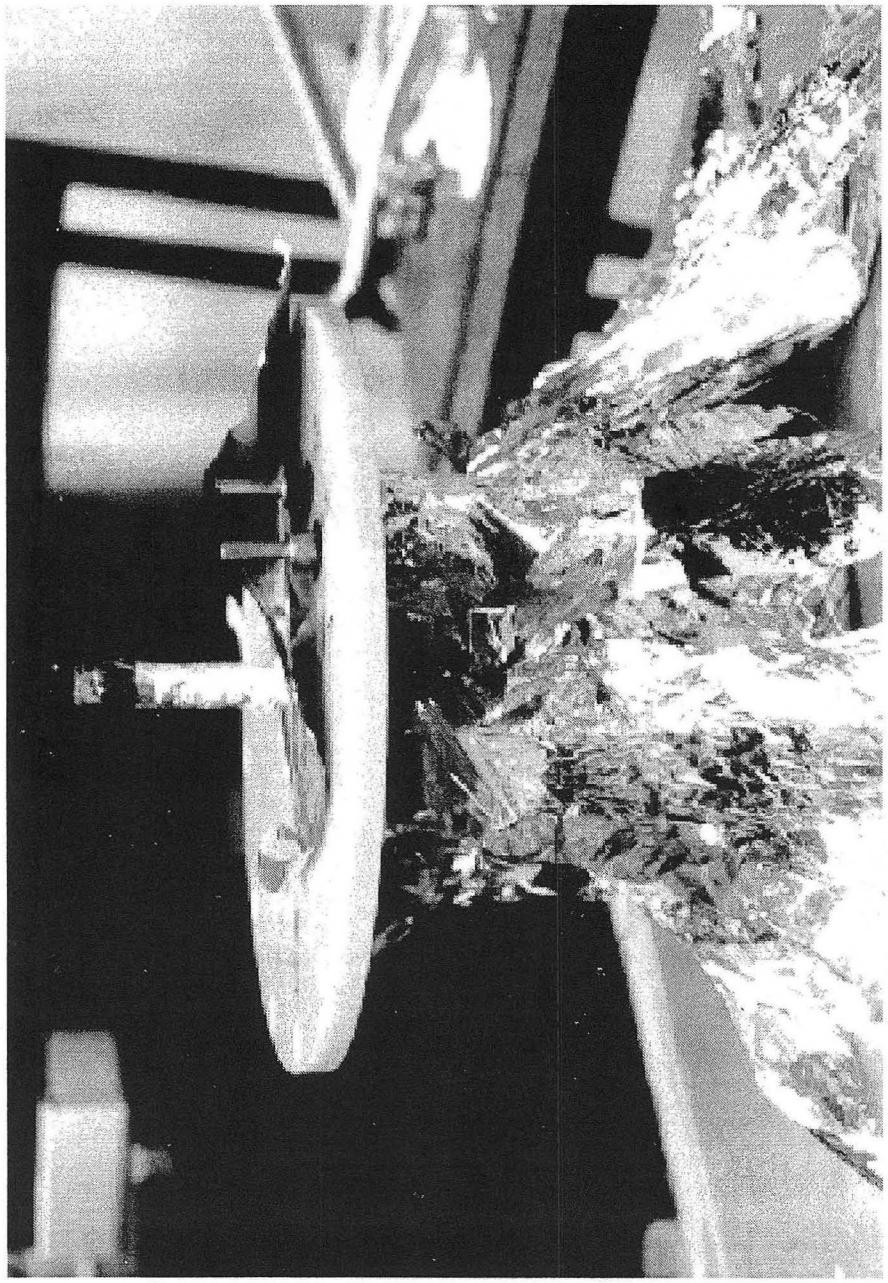

Figure 5.4. Photograph of Dewar Internals. Note: picture is rotated.

nection to the SQUID feedback electronics box. The purpose of the switch box was to short the voltage and current connections so that any little spikes coming from flipping switches on the SQUID feedback box (such as the bias current switch) would not directly spike the SQUID. The last three dewar connectors were sent to another small electronics box whose purpose was to interface to the Variac and the ohmmeter and provide a simple switch to choose between the different heaters and temperature sensors (platinum resistors).

This was a completely different design philosophy compared to the low temperature SQUID probe. One difference was of course that the high-T_c SQUID was not submerged in the cryogen as was true for the low-T_c SQUID, the consequence being that special care was needed to make sure that the SQUID had good contact to the cold finger and was cold enough to be superconducting. Another important difference was that the SQUID magnetometer detected directly the NMR signal rather than remotely through a flux transformer as was the case in the low temperature probe, see Chapter 4. The low temperature SQUID could be meticulously shielded from all types of magnetic fields including the fields necessary for NMR. This was not the case for the SQUID microscope, a situation which often required us to have extra patience in tracking down and eliminating noise. A design for a liquid nitrogen NMR/MRI probe or dewar that utilized a large flux transformer that encircled the sample was unfortunately not possible because no one had yet developed high-T_c superconducting wire. As of the writing of this thesis, researchers had successfully made a flexible ribbon made of plastic with YBCO. Perhaps composite materials like this will enable the design of a better high transition temperature SQUID NMR/MRI probe.

5.3 The SQUID, the Coils, and the Spectrometer

For proton spectroscopy and imaging we used the SQUID "Cartwheel Magnetometer" described in Section 3.5.2 and shown in Figure 3.6. Out of the sixteen loops, three were verified visually as being dead due to obvious erosion in the YBCO pattern. Others may have been dead, but we could not tell; nevertheless,

the four year old device still functioned. The 1/f noise elbow was situated around 5 kHz, and the high frequency noise figure for the system was almost 30 $fT/Hz^{1/2}$. This corresponded to a system flux noise of 25 $\mu\Phi_0/Hz^{1/2}$ for the 1.8 mm^2 effective area of the SQUID.

The static field B_o was produced by a pair of Helmholtz coils each with a diameter of 12 cm and a separation of 6 cm. Each coil was wrapped with 1,300 turns of 30 AWG copper magnet wire. The excitation field B_1 coils were also a Helmholtz pair oriented perpendicular to the B_0 coils. These AF coils had a diameter of 8.6 cm and 20 turns of 26 AWG copper wire. They were tuned by simply soldering a capacitor in series with the coils. The gradient field $G = \frac{dB_z}{dz}$ was produced by a Maxwell pair situated on axis and just outside of the static field coils. These coils also had a diameter of 12 cm and 50 turns of 30 AWG copper wire. The coil frame was made of G-10 fiberglass and plexiglass and was screwed down to the top of the SQUID dewar. Figures 5.5 and 5.6 are a schematic and a photo, respectively, showing the dewar with coils. The maximum coil size was limited by the length of the headpiece. If we had made coils larger than 12 cm, their sweet spot would have been much higher than the effective sensing depth of the SQUID. On the other hand, it was not possible to build coils to enclose the entire SQUID dewar because they would not have fit inside the triple layer μ-metal shield that enclosed the whole system. The μ-metal can was necessary to shield the low frequency magnetics which the Faraday cage did not properly shield. External DC fields were attenuated by a factor of 1,430 by the extra shielding.

The pulse programmer and digitizer we used was a TecMag ARIES controlled by MacNMR V.4.5.9 running on a Macintosh IIci. One TTL signal line was dedicated to the SQUID trigger. Another TTL line was used to gate a Hewlett-Packard 3314A Function Generator to produce the excitation pulses. The output of the function generator was fed to an old Krohn-Hite Model 3322 Filter which we employed as a 20 dB power amplifier. The output was then sent through the Faraday cage into the pulse coils. The output of the SQUID electronics (the signal) was fed out of the Faraday cage where it was split: one signal line was connected to the input of a Hewlett-Packard 3561A Dynamic Signal Analyzer while the other

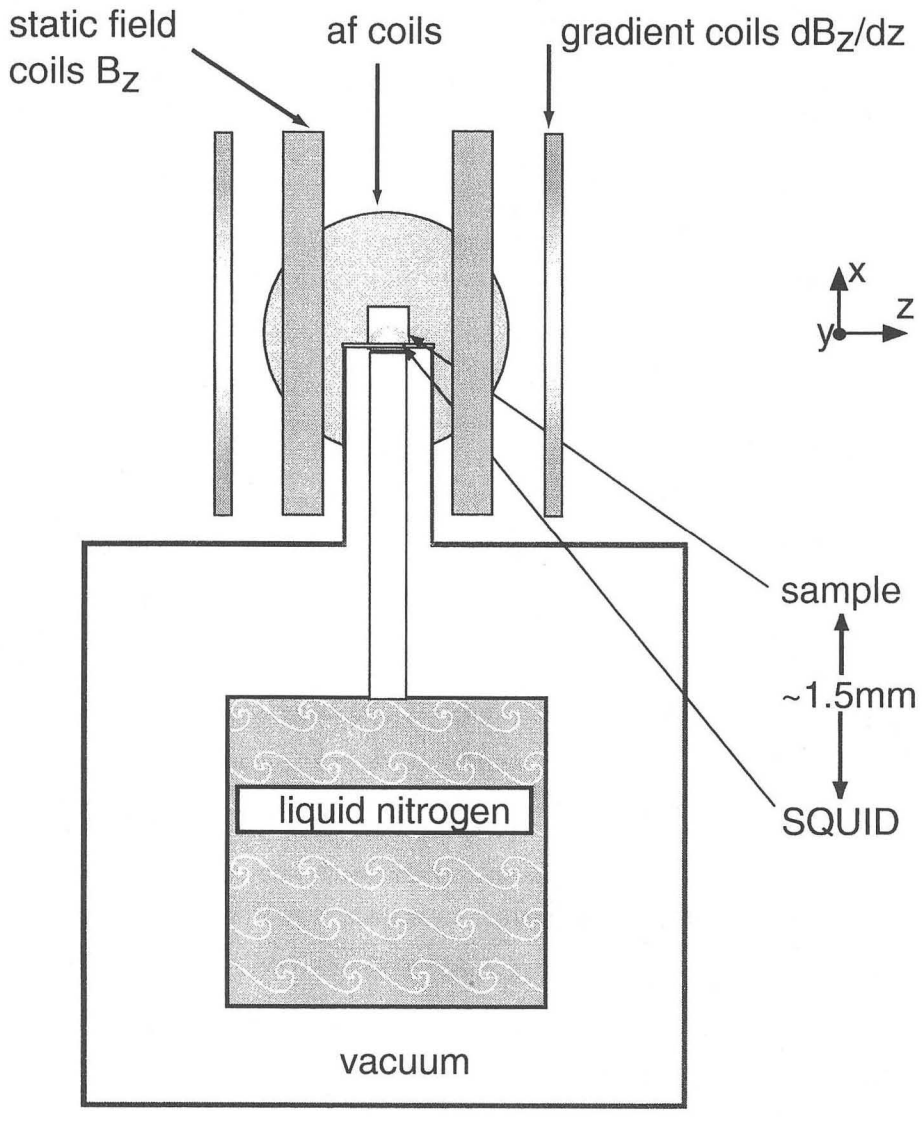

Figure 5.5. Schematic of High-T_c SQUID Dewar with Coils

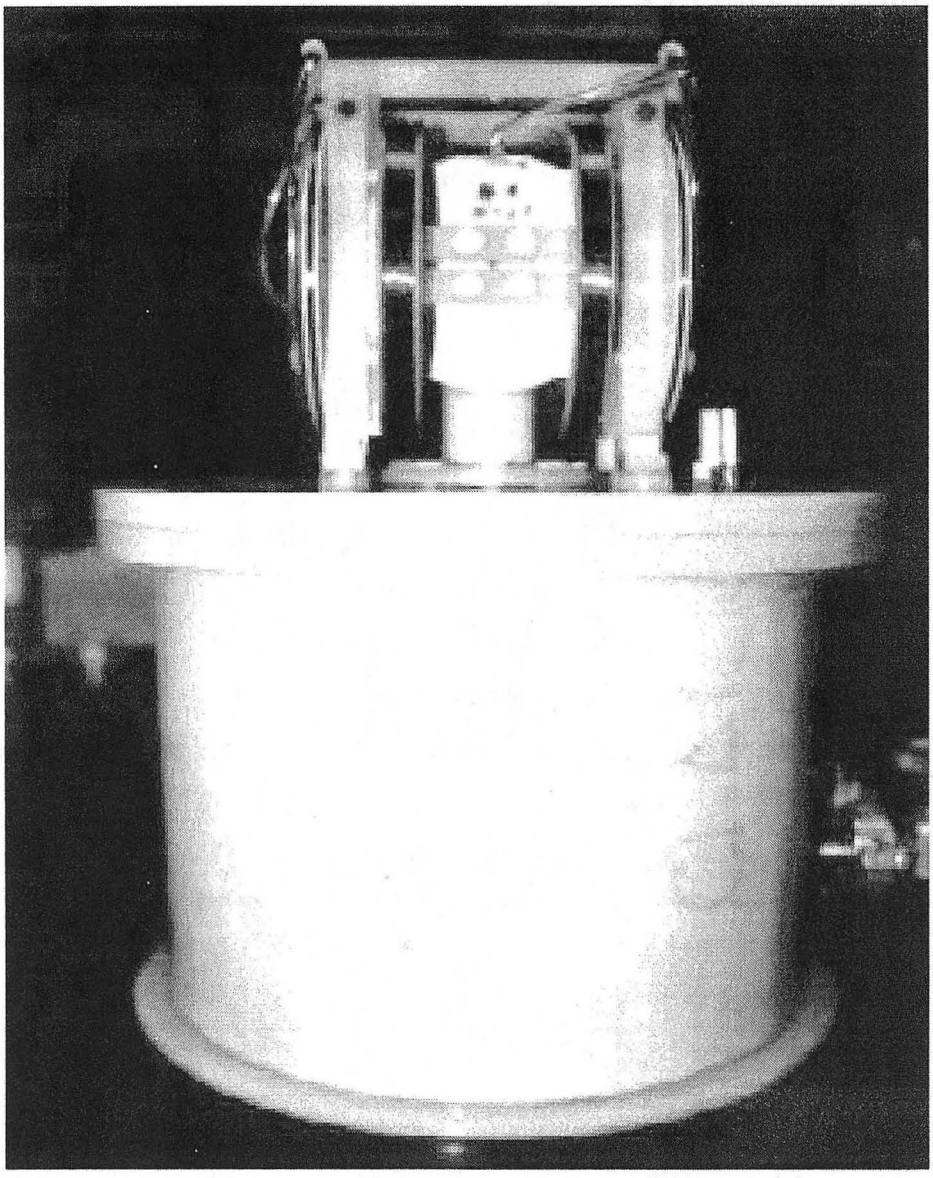

Figure 5.6. Photograph of High-T_c SQUID Dewar with Coils

was routed to a Rockland Wavetek Model 442 filter where it was amplified by 40 dB and band-pass filtered before sent to the digitizer of the ARIES. The signal analyzer was necessary to track in real-time whether or not the SQUID was locked during the acquisition. While it was possible to track real-time signal on the TecMag, it displayed the running average of acquisitions rather than the last single scan, which is what we were interested in. We spent many, many hours simply watching the screen of the signal analyer, waiting for a discontinuous jump in the time trace signifying that the SQUID had "jumped" flux quantum states and the feedback electronics were not properly tuned. Flux jumps inevitably happened; in best case, it meant that the feedback electronics needed to be adjusted in order to "keep up" and cancel the incident flux. In worst case, the SQUID had absorbed too much flux which was trapped in flux vortices and pinning sites changing the critical current and making the SQUID unstable. When a jump occurred, the SQUID cage had to be opened (sometimes acquisition stopped, sometimes not), and the electronics tuned to feed back more (or less) current to the feedback coil. If the SQUID could not be re-locked, then it needed to be thermal cycled. Thermal cycling the SQUID simply meant heating the SQUID a few degrees above the superconducting transition to allow the trapped flux to dissipate. After cooling the SQUID back to a superconducting temperature, experiments could be resumed. The signal analyzer also required a TTL trigger line from the TecMag ARIES so that it would collect at the proper time.

5.4 Proton NMR Signals

Figure 5.7 is a proton spectrum of 1 mL of mineral oil in a field of 20 $Gauss$. The NMR peak had a small 2:1 signal-to-noise, but it was acquired with only a single scan. The $\frac{\pi}{2}$ pulse was 200 μs long with a field amplitude of 60 μT. The resonance frequency was $\nu = 86.7\ kHz$, and the thermal polarization was 7×10^{-9}. A particularly impressive spectrum is shown in Figure 5.8. It displays a proton NMR spectrum of 1 mL of mineral oil at Earth's magnetic field. Notice that I say "at" rather than "in." Because of the triple layer mu-metal shield that the

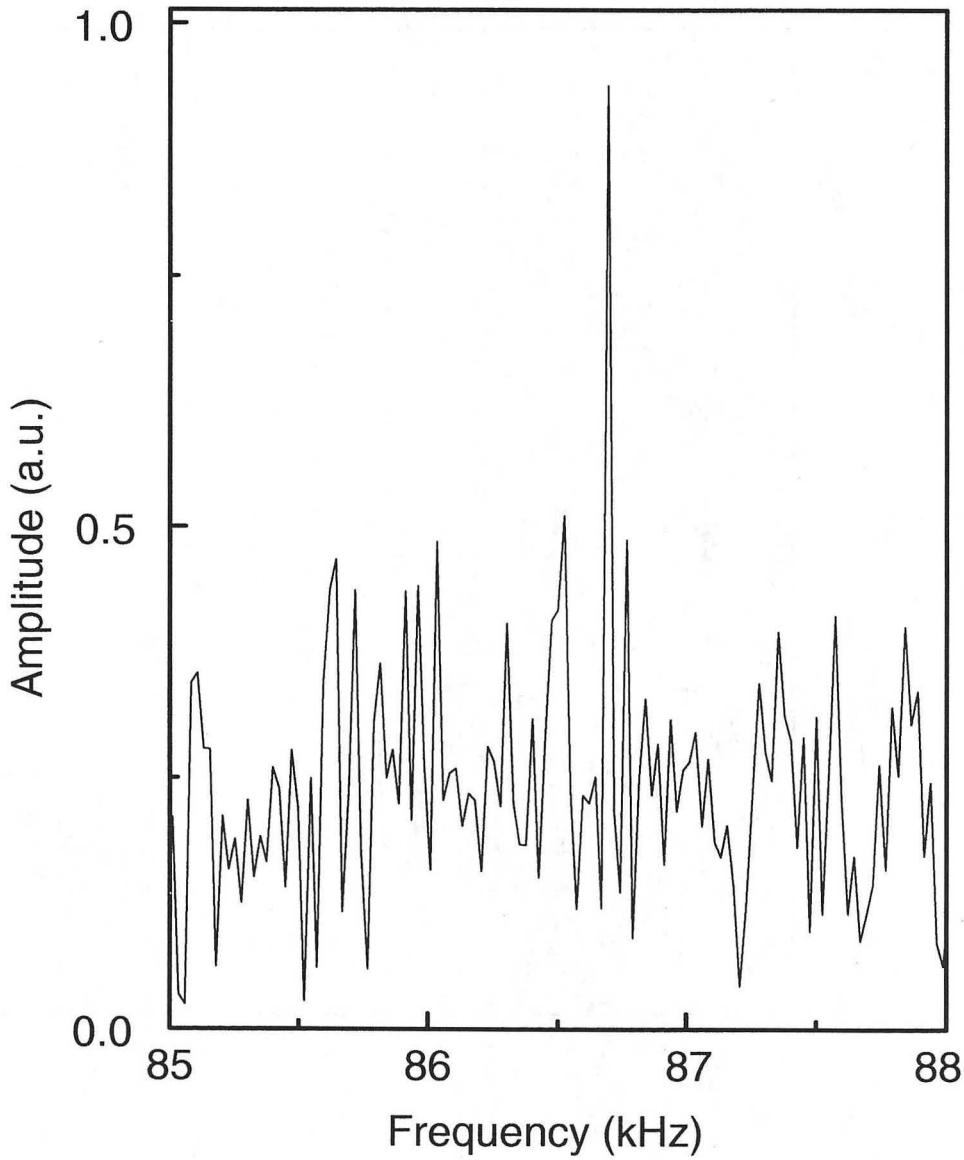

Figure 5.7. Proton Spectrum at 20 G. Only a single scan on 1 mL of mineral oil

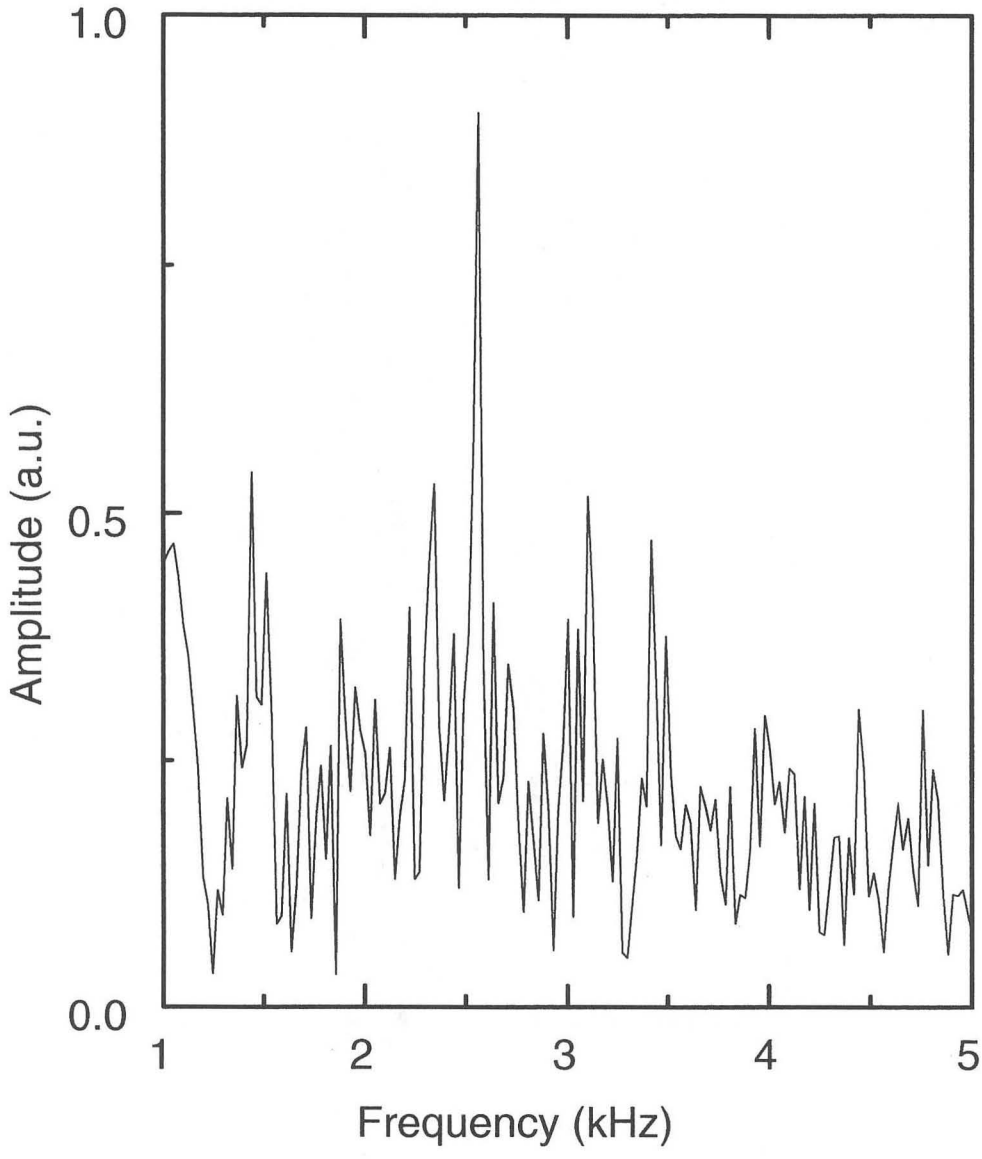

Figure 5.8. Earth's Field Proton Spectrum. 10,000 scans of 1 mL of mineral oil in a static field of 59 μT.

SQUID dewar sat in, Earth's field was shielded out. So we charged our static field coils to 0.59 G and were able to see the proton peak at 2.57 kHz with a signal-to-noise ratio of 2:1 in only 10,000 scans. While the first Earth's field proton NMR was taken in 1954 by Packard and Varian [152], they had prepolarized the sample above Earth's field thermal equilibrium. The final spectrum, Figure 5.9 is again of protons in 20 G but not from mineral oil. This is a spectrum of *in vivo* water in a finger. The finger belonged to Dr. Ricardo de Souza; he only had to place his finger on the sapphire plate over the SQUID for about a minute while 100 scans were collected.

Because of the high nuclei density, high gyromagnetic ratio of protons, and short relaxation times, the room temperature mineral oil proved to be a convenient sample for reliably taking spectra and testing the new SQUID instrument. Mineral oil is an unquantified mixture of long chain hydrocarbons and has a proton density similar to water's 100 *molar*. It had short relaxation times for faster signal averaging. Small signals made it difficult to accurately measure relaxation rates with our equipment, but we ballparked the T_1 to be about 50 *ms* and T_2 to be about 15 *ms* at 20 *Gauss*. Mineral oil was the easiest sample to work with, and we used this standard for almost all of the proton MRI experiments.

5.5 Proton Imaging

5.5.1 Projection Reconstruction: Linear Backprojection

For the 2-D imaging done with the low critical temperature SQUID, we employed a projection reconstruction method of rotating the sample in a static gradient and then remapping the polar raster of data to a Cartesian space where we could perform a 2-D Fourier transform (see Section 4.2.2). For all of the proton imaging with the new SQUID, it was still necessary to rotate the sample in a static gradient, but the data reconstruction was different; we decided to use a method known as linear backprojection [153] simply because we had not used it before. The main difference between the two methods is that the first method combines

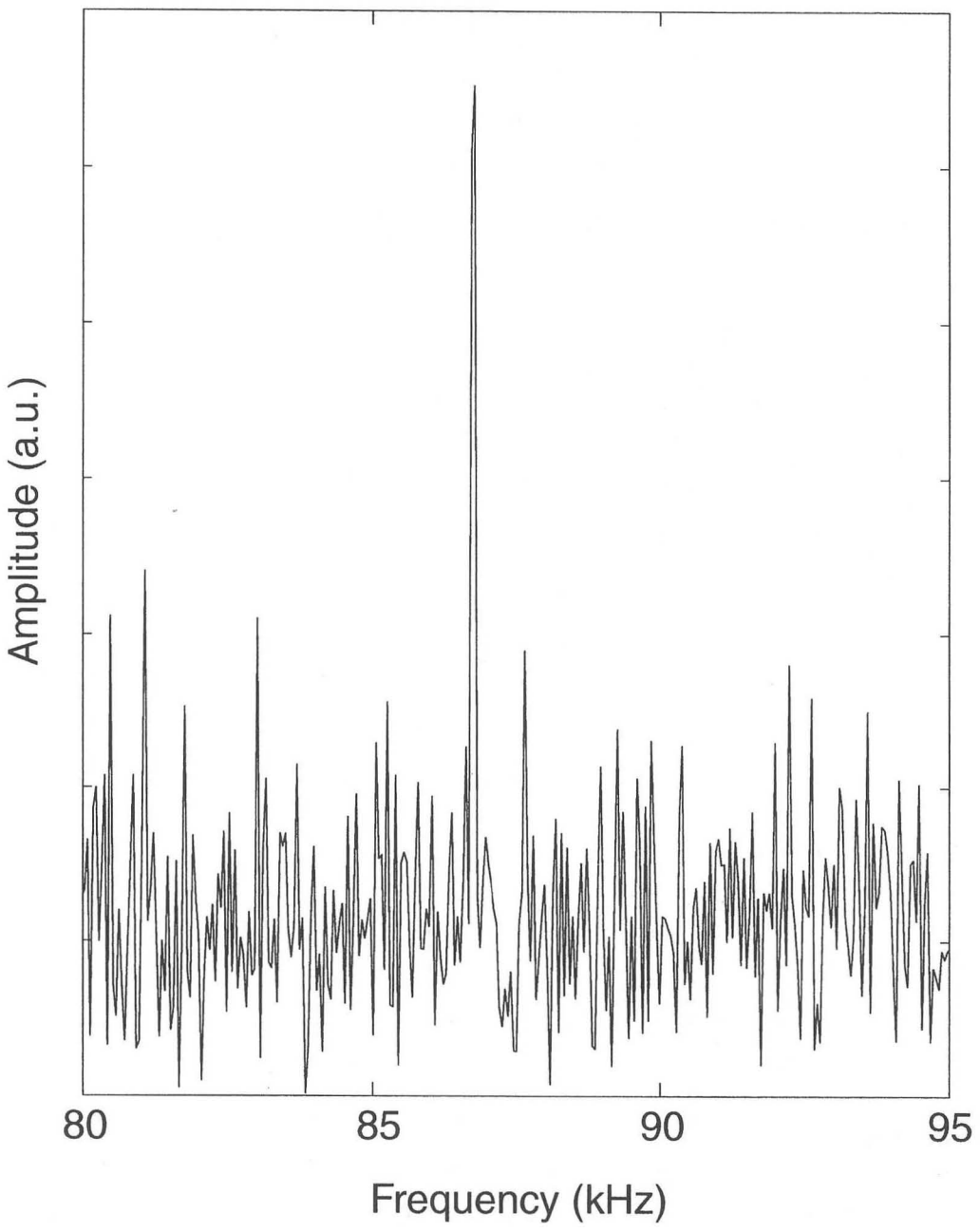

Figure 5.9. ***In vivo*** **Low-Field NMR Proton Spectrum from a Finger.**

the data in time space and uses the 2-D Fourier transform to convolute the data and produce the image. The second method combines the data in frequency space (requiring first the individual Fourier transforms of each of the spectra) and then adds the projections together.

The linear backprojection procedure involved first Fourier transforming all of the FIDs and finding the centers of each of the 1-D images—which should all have been at the same central NMR resonance frequency unless there was drift in the static or gradient fields during the acquisition. Refer to Figure 1.2 in Chapter 1 for a reminder of what 1-D projections look like. Most points of each spectrum were thrown away leaving just the peak (the image) and some of the points directly surrounding it. Each spectrum was transcribed to its appropriate position in a square matrix. Figure 5.10(a) shows two spectra transcribed in matrices, one from a 0° projection and one from a 45° projection. For clarity, two arrays of numbers are used in the figure rather than pictures of the 1-D projections. The next step was to fill the matrix with the particular projection in the directions orthogonal to how each spectrum was placed in the matrix (see Figure 5.10(b)). The bottom matrix of the 45° projection is partially empty to make it easier to see how the matrix was filled. The empty boxes were not automatically filled by backprojecting the diagonal array, so they needed to be filled by averaging the four (or three) boxes around each empty box. That is where the numbers "5" and "4" come from. The same procedure is done for each spectrum and the matrices are added together to give the final picture, Figure 5.11.

5.5.2 Mineral Oil Images

In the high-T_c system, we used the SQUID as an NMR surface coil, so it was most sensitive to samples with the same area as the coil and with a depth approximately half of the diameter. Since the SQUID "Cartwheel Magnetometer" had a diameter of 7 *mm* we prepared samples that also had diameters of 7 *mm*. The first presentable image we acquired is shown in Figure 5.12. The sample was mineral oil contained in a tube made of 7 *mm* ID Pyrex glass epoxied to

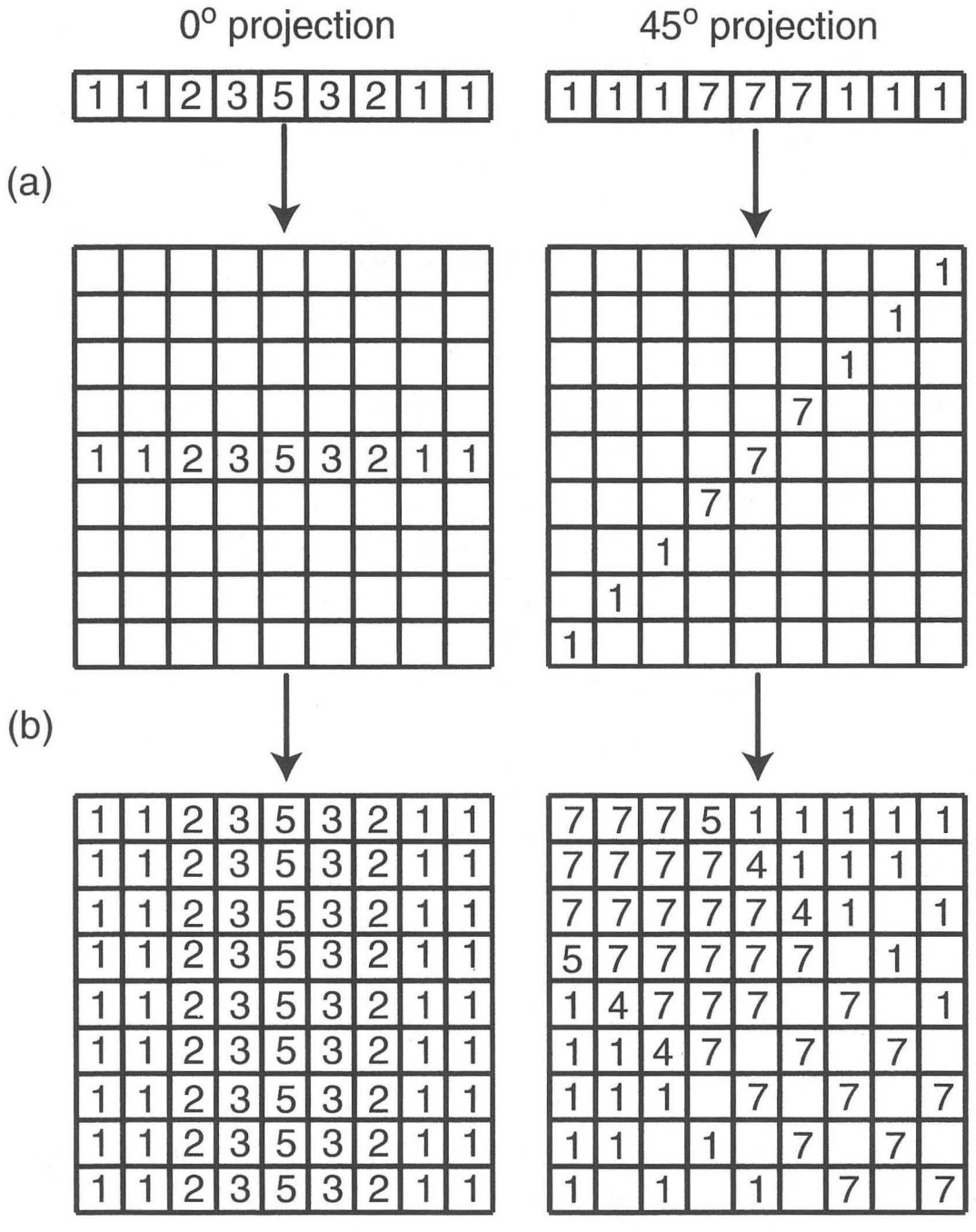

Figure 5.10. Linear Backprojection Steps 1 and 2

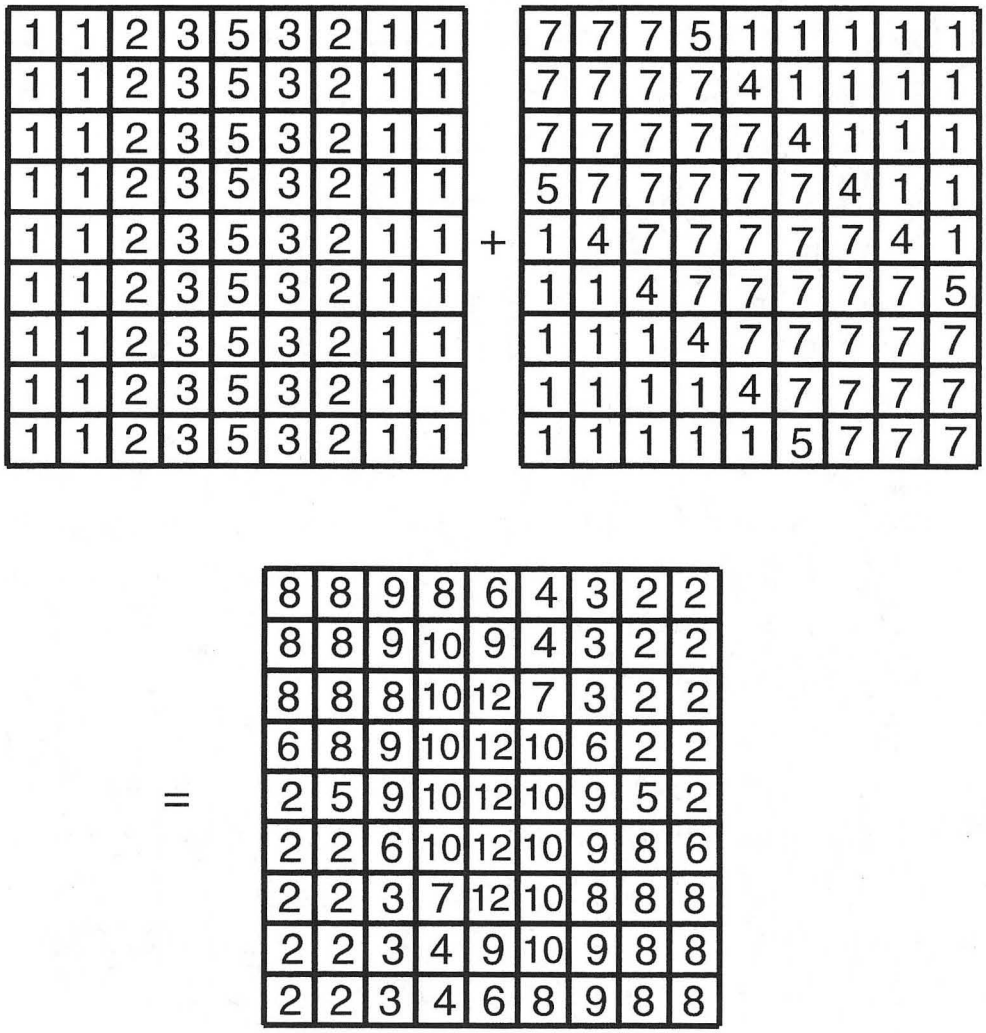

Figure 5.11. Linear Backprojection Step 3

a 1 *mil* quartz slide cover (for optical microscope slides). The thin slide cover helped tremendously in getting the sample as close to the SQUID as possible. The two "eyes" of the round face correspond to two glass rods each with diameters of about 1.5 *mm* glued to the bottom of the cell with a separation of about 2 *mm*. Since they displaced the mineral oil, they show up in the image as missing proton density. Figure 5.12(a) shows the true data pixelated image with an inset depicting the cross section of the sample tube while (b) is the digitally smoothed version. Also imaged was a "smile," Figure 5.13 which was again mineral oil in one of our custom sample cells but with a "C" cut from a tube of plexiglass (Lucite) epoxied to the bottom slide cover.

Confident that we could image glass and plastic phantoms, we decided to try something fancier. The final proton image shows the cross section of a Serrano green chili pepper, Figure 5.14. The pepper slice had an outside diameter of 7 *mm* (to fit in the cells) and a height of 5 *mm*. Due to the poor image quality, the pepper pictures (of which I already show the best) were never published. And color interpolation made them look even worse. Nevertheless, the broad features like the pepper pockets are visible in the image, proving that non-mineral oil samples could be imaged as well. Figure 5.14(a) is a picture of the actual pepper cross section; (b) is the proton MRI.

Each of these images was taken in a static magnetic field $B_o = 2.037\ mT$, corresponding to a proton Larmor frequency $\nu = 86.72\ kHz$. We pulsed on resonance at 86.7 kHz with a pulse width of 120 μs and magnetic field magnitude of 58.6 μT. This corresponded to a 54° tipping angle, which allowed us to pulse at a rate of 25 Hz (pulse delay of 40 ms) rather than wait the rule-of-thumb 5 times T_1 after a 90° pulse. We used a single pulse sequence (rather than a two pulse spin echo) and had a dead time of 200 μs after the pulse before we could acquire signal. All of these images were also taken using a single gradient and rotation of the sample. The gradient was in the z direction (on axis with the static field) and had a strength $\frac{dB_z}{dz} = 0.02\ mT/cm$. Each image was composed of 24 1-D projections obtained by sequential rotation of the sample in 15° increments. Each projection was a composite of 30,000 averages. We oversampled by two times just as we had

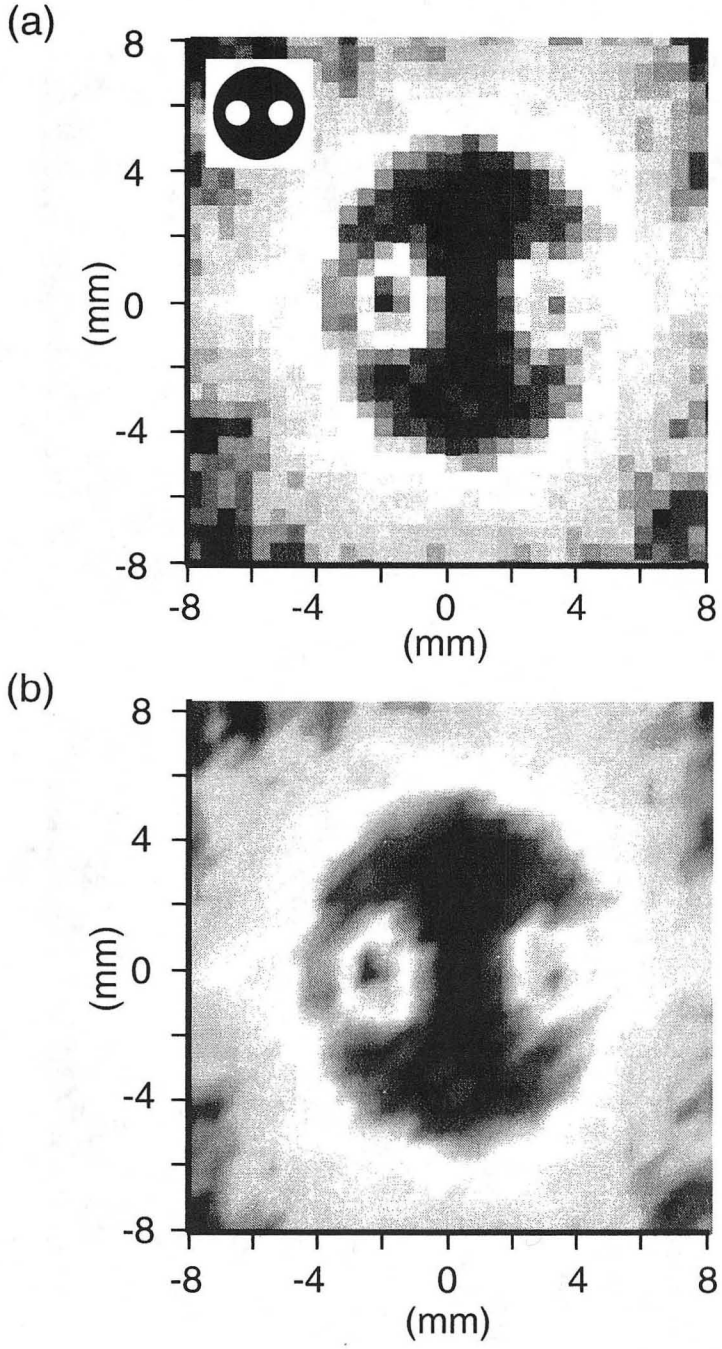

Figure 5.12. "The Proton Face." MRI of mineral oil in sample tube with two glass rods displacing the mineral oil.

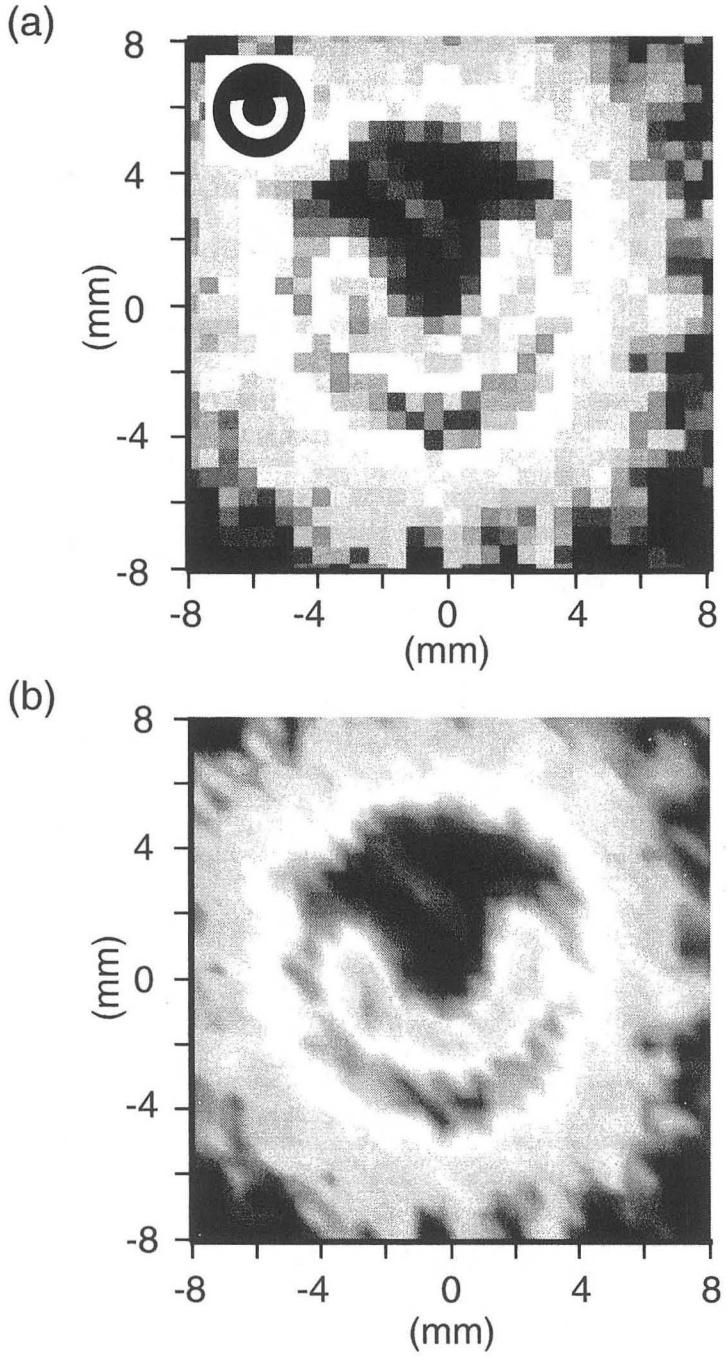

Figure 5.13. "The Proton Smile." MRI of mineral oil in sample tube with a plastic "C" displacing the mineral oil.

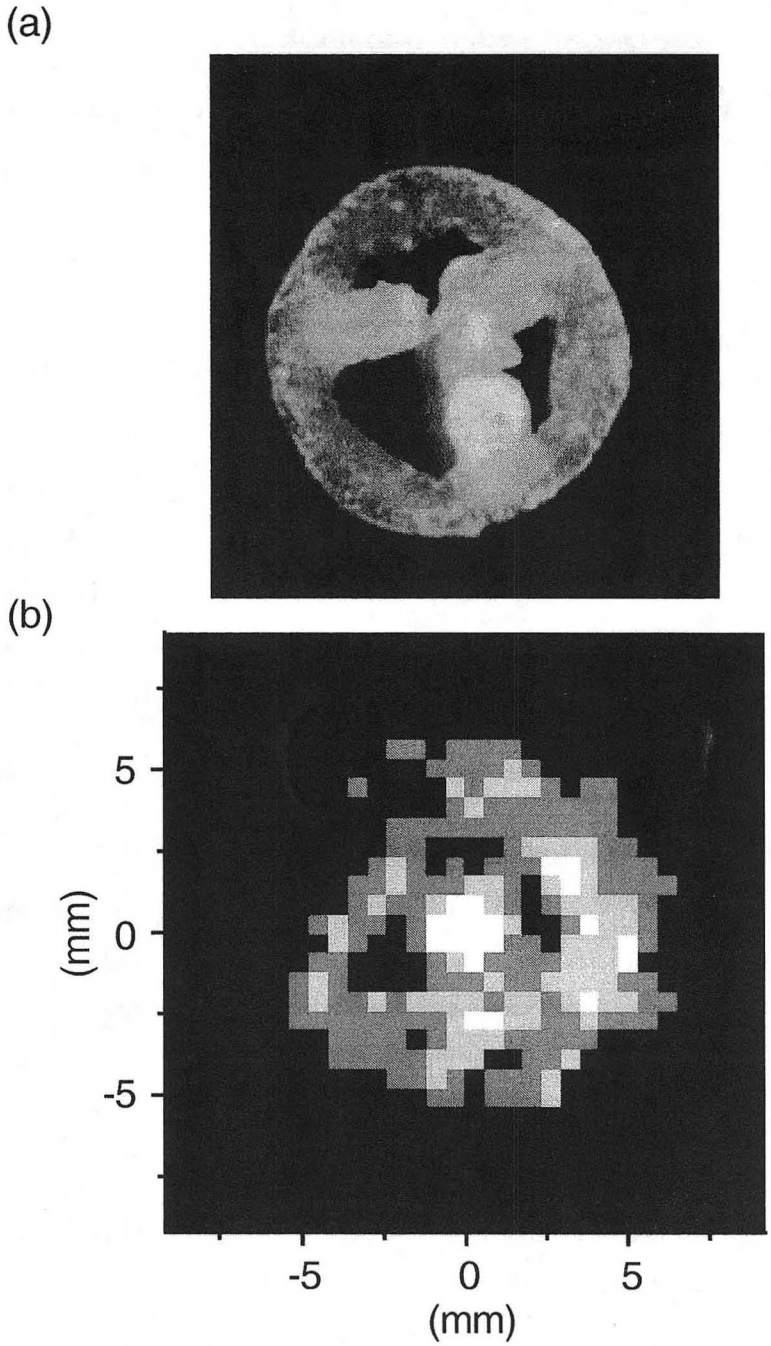

Figure 5.14. "Chili Pepper." (a) Actual pepper cross section. (b) MRI image of the pepper.

for the low temperature xenon image. In this case, however, it was necessary to do so as we noticed an asymmetry (usually a dip in each of the spectra) that seemed to be an artifact of our equipment since it seemed to be independent of sample orientation. We had to cancel the asymmetry by oversampling and combining all of the spectra. Total time required to obtain each picture was approximately 12 *hours*.

5.6 Pulsed Gradients

Having to rotate the sample to obtain MRI pictures was a pretty crude method, so we were eager to modify our MRI machine for 3-axis pulsed gradients. Unfortunately, as we would learn, applying pulsed gradients to a sample with the SQUID right beneath it would require extra patience on our part. The first step towards multi-axis gradients was building a new set of gradient coils. Figure 5.15 shows a photograph of the gradient coils. These Golay coils were composed of a simple Maxwell pair to provide the on-axis gradient $\frac{dB_z}{dz}$ while each of the off-axis gradients $\frac{dB_z}{dx}$ and $\frac{dB_z}{dy}$ was generated by four coils. The coil form was made of clear plexiglass with a diameter of 13 cm and length of 35 cm. The coils were wrapped with 30 turns (per gradient) of 24 *gauge* insulated copper magnet wire. The static field coils and audiofrequency pulse coils fit inside the Golay frame. The static field coils were an Helmholtz pair with an outer diameter of 12 cm and separation of 5.5 cm. They could produce a field of 2.26 mT per *Ampere* of current. The transmitter coils were also a Helmholtz pair and produced a field of 13 μT for 100 mA of current, giving a $\frac{\pi}{2}$ pulse time of 250 μs for xenon and 69 μs for protons. Figures 5.16 and 5.17 are a schematic and photograph, respectively, of the Golay coils (with static and pulse coils) mounted on the SQUID dewar.

Along with new coils we also needed a new console with a pulsed gradient controller. We bought a TecMag Orion with DAC-18 Gradient Controller. The control software was NTNMR version 1.3 running on a Pentium II-300 PC with Windows NT 4.0 with Service Pack 3. We used Techron 7780 Gradient Amplifiers in current feedback mode to drive the coils. They were certainly overkill and killed

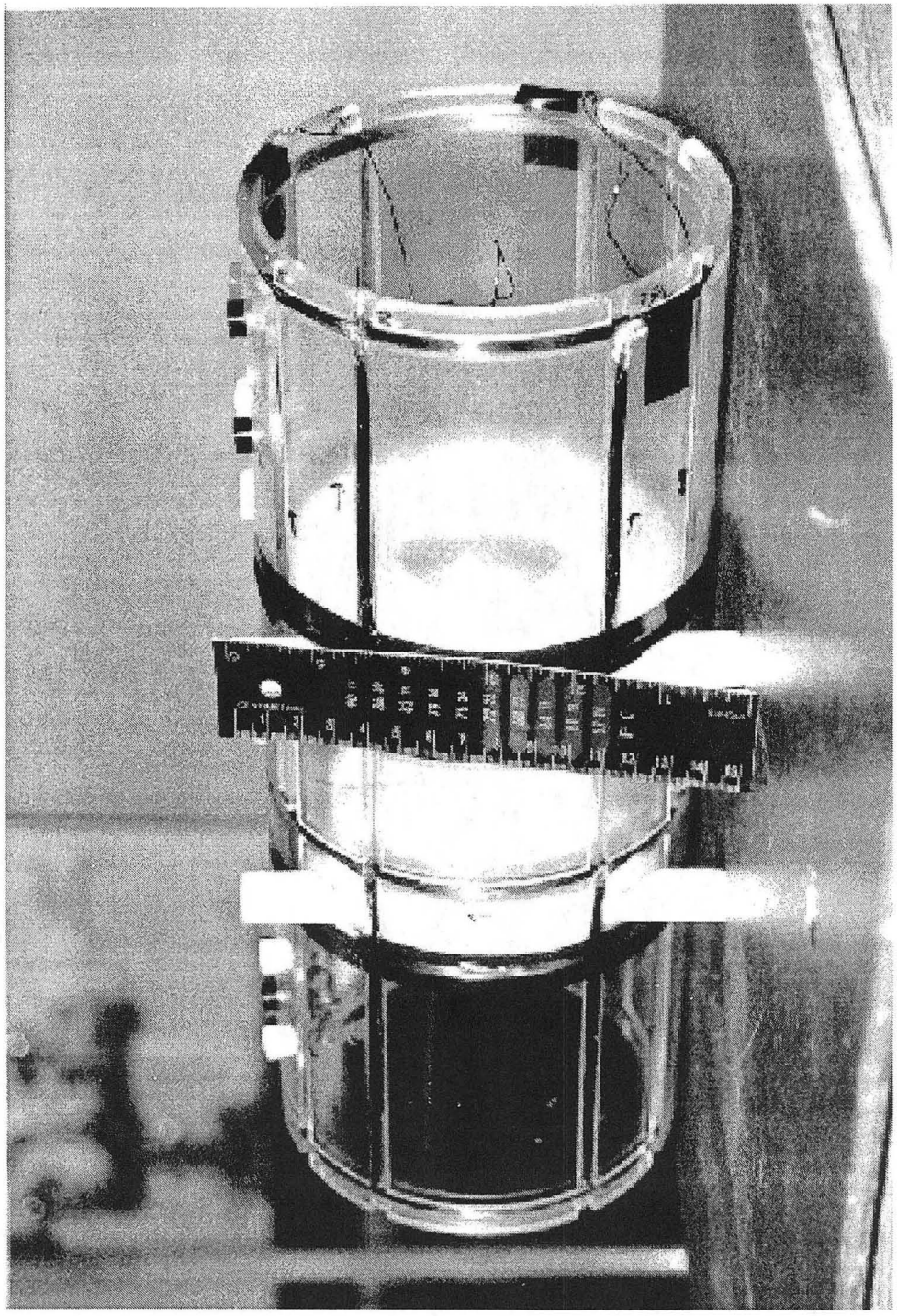

Figure 5.15. Photograph of Golay Coils

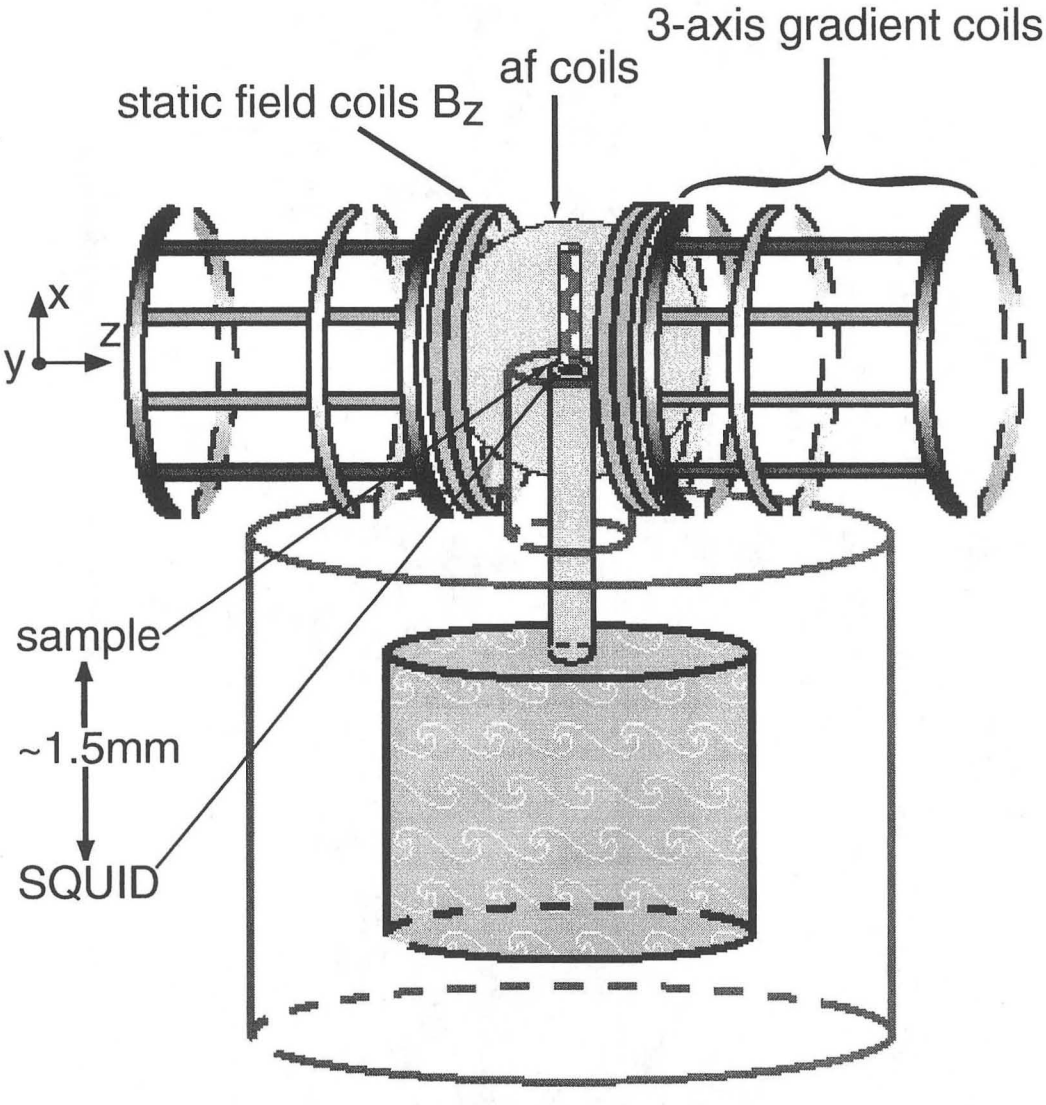

Figure 5.16. Schematic of Golay coils mounted on SQUID dewar

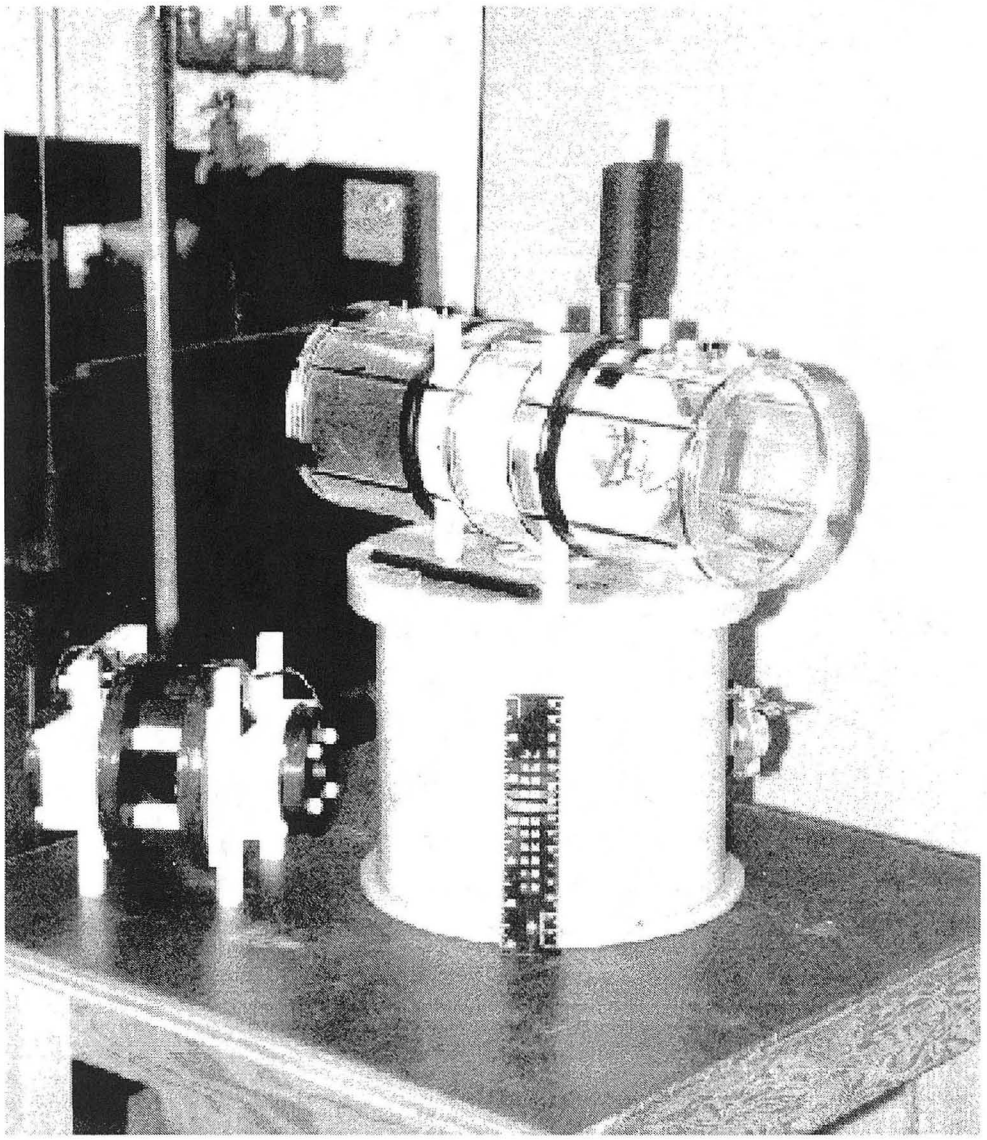

Figure 5.17. Photograph of Golay coils mounted on SQUID dewar

our coils on more than one occasion. However, they were the best bipolar power amplifiers (to drive current both positive and negative) on the market and were purchased with the notion that we would eventually need them for microimaging or imaging big things, like people.

We made two improvements that helped cut the noise from the gradient circuits. The first was a triggered blanking circuit connected at the output of the amplifiers before the coils. The circuit diagram is sketched in Figure A.1 in Appendix A. A TTL signal from the pulse programmer turned on the two transistors in the circuit which then dumped the current from the amplifiers at the input of the circuit to ground before the current could get to the gradient coils. The crossed diodes insured that the low voltages due to the amplifier noise got grounded out rather than sent to the coils.

The second modification was the set of baseline correction circuits placed at the output of the DAC-18 gradient controller and before the inputs to the gradient amplifier. We found that small offsets in voltage from the gradient controller on the order of 1 mV resulted in a sizable current from the amplifiers on the order of 10 mA passing through the gradient coils. There was an offset potentiometer inside the gradient controller box for each of the channels x, y, and z. However the resolutions of these variable resistors were not fine enough to cancel the offset satisfactorily. Also there was always drift of the baseline voltage during the course of any long acquisition, due possibly to changes in temperature. So it was necessary to build external circuits to cancel the drift. The circuits were simple unity gain adding amplifiers which added a manually controlled, variable voltage from an internal battery to the output of the gradient controller, see Figure A.2 also in the Appendix. These baseline correction circuits also proved to be necessary to accurately set the current amplitude of the phase encoding gradient pulse. The TecMag system did not provide fine enough control of the small currents that we were using.

5.7 Hyperpolarized Xenon

Figure 5.18 is a spectrum of hyperpolarized xenon in a static magnetic field of 1.27 mT, giving a resonance frequency of 14.9 kHz. The sample of naturally abundant xenon with a pressure of 2 atm was contained in a sample tube 1.4 cm long and 0.5 cm in diameter. It was optically pumped using the setup described in Section 4.2.5 to a polarization of approximately 2%. With a single $\frac{\pi}{2}$ pulse we obtained a large signal-to-noise ratio (SNR) of almost 100. Unfortunately, we could never reproduce this result. Out of the dozens of attempts, we were able to observe only a few spectra. There are still many unanswered questions as to why we were so unsuccessful: was the optical pumping not successful or was the polarization lost and where was it lost? There were too many variables involved in pumping sample in Hildebrand D-60 (the old Gamma room), freezing the sample from the pumping cell into a suitable sample cell, running the xenon down to Hildebrand D-45 (the old SQUID room), defrosting the sample, transferring it through the mu-metal shield through the SQUID coils, and finally taking an NMR scan. We needed a method to consistently polarize and deliver the xenon to the SQUID. So we built a flowing xenon, continuous optical pumping system.

5.7.1 Recirculated Flow Optical Pumping

One of the limitations that most hyperpolarized noble gas NMR and MRI systems suffer from (including our previous SQUID imager) is the non-recoverable nature of optically pumped nuclei. Since the gas is prepared in a non-equilibrium state, the completion of one NMR or MRI scan using a $\frac{\pi}{2}$ pulse destroys the enhanced polarization. In this so-called "batch" pumping mode, a volume (typically on the order of 100 mL at 100 $mTorr$) of optically pumped gas is prepared in about 20 $minutes$. Since it is inconvenient to wait one third of an hour between scans while more gas is being polarized, it is possible to collect and store a large volume of hyperpolarized gas for later use, since it retains a high polarization for about a day if kept in a strong magnetic field. However, unless you have hired

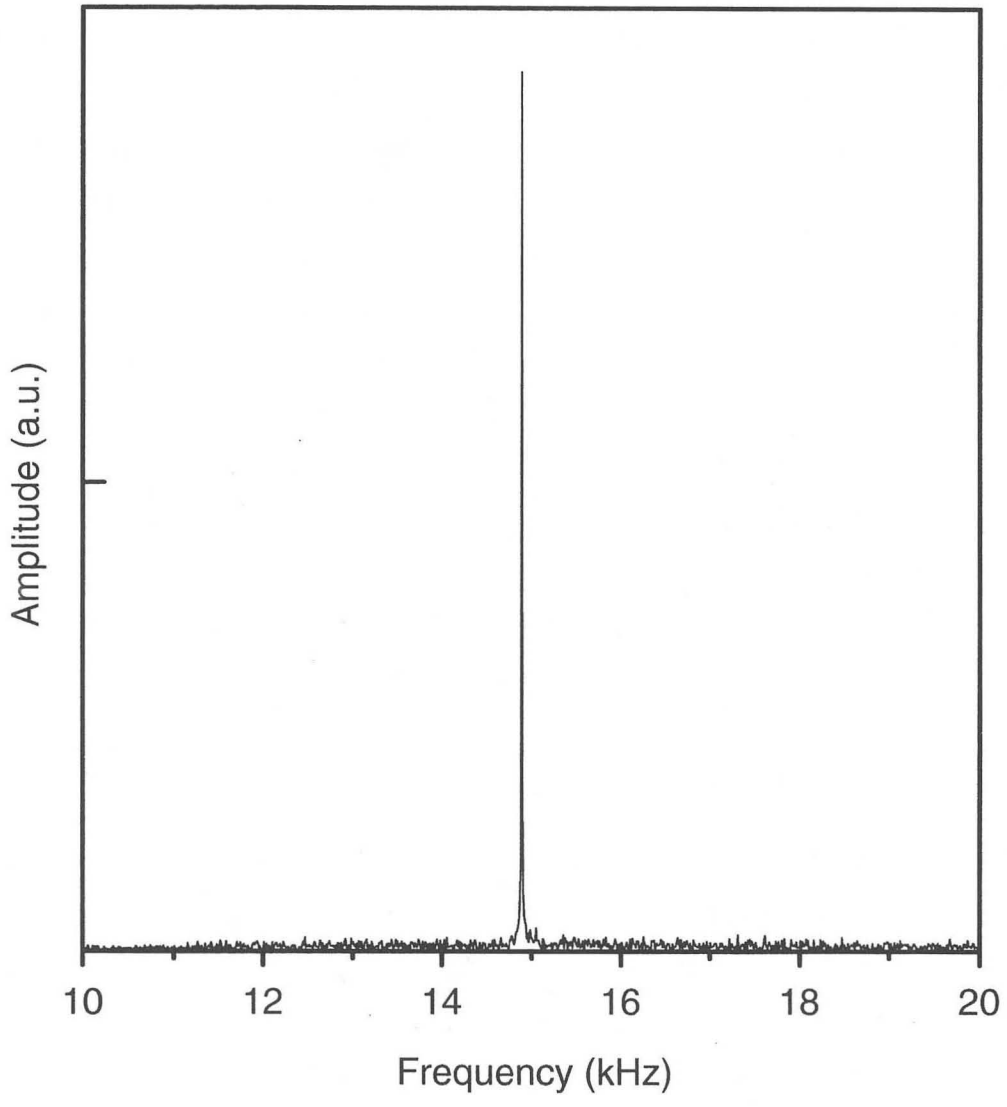

Figure 5.18. Single scan of hyperpolarized xenon in a field of 1.27 mT.

someone just to polarize gas for you, you are still spending a great deal of time preparing the gas. Alternatively, if the sample is large and detection equipment is very sensitive, a number of scans can be collected using small tip angle pulses. The latter is possible in certain cases at higher frequencies or with our low transition temperature SQUID system, but this batch mode becomes a serious restriction for high resolution MRI or microscopy, especially at low fields where maximum possible signal strength is critical.

On the other hand a circular flow [154, 155, 156, 157, 158] optical pumping system provides a continuous, stable, and infinite source of hyperpolarized xenon—making possible the use of large tip angle pulses and signal averaging. In fact, this ability to signal average using a circular flow hyperpolarized xenon setup was critical in enabling Kaiser *et al.* [159] to obtain MRI images with 100 μm resolution with a 4.2 $Tesla$ imaging system.

In Figure 5.19 we schematically show our optical pumping apparatus. The centerpiece was the Pyrex glass pumping cell composed of parts (B), (C), and (D). A photo of the pumping cell is shown in Figure 5.20. The rubidium reservoir (B) supplied rubidium atoms to the irradiation bulb (C) where they absorbed circularly polarized light and collided with xenon, transferring the laser light angular momentum. The water jacket (D) then cooled the gases and condensed out the rubidium. Parts (B) and (C) were mounted inside of an air-heated oven (not shown) made of aluminum with a 3.2 mm thick quartz window. The oven was built into the center of a pair of 23 cm diameter, air-cooled Helmholtz coils (A) (only one of the pairs shown for clarity) that produced a field of 8 mT with an applied current of 10 A. A photograph of the coils, oven, and pumping cell is shown in Figure 5.21. The xenon was circulated between the pumping cell and the sample using a completely sealed, maintenance free, high pressure circulation pump manufactured by Brey, Inc (G). It was capable of a range of gas flow rates depending on the input voltage. The sample cell (E) was a flat-bottomed, stoppered Pyrex glass cylinder with an inner diameter of 1 cm and capacity of almost 1 mL. It had 1/4 in Pyrex glass delivery tubes on opposite sides of the cell. The stopper could be easily unscrewed to gain access to the sample. (F) was the SQUID detector. All

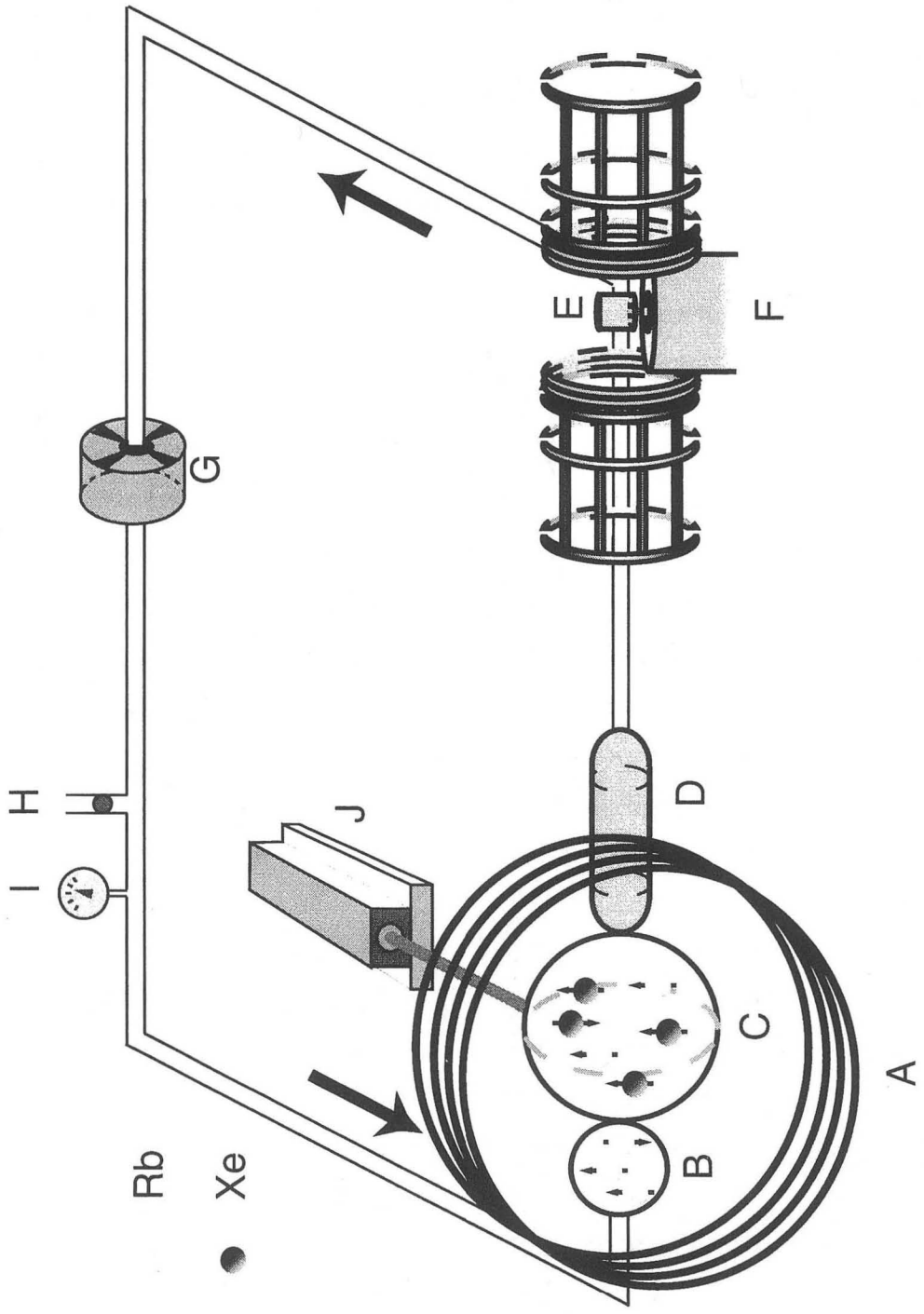

Figure 5.19. Schematic of the Circular Flow Optical Pumping System

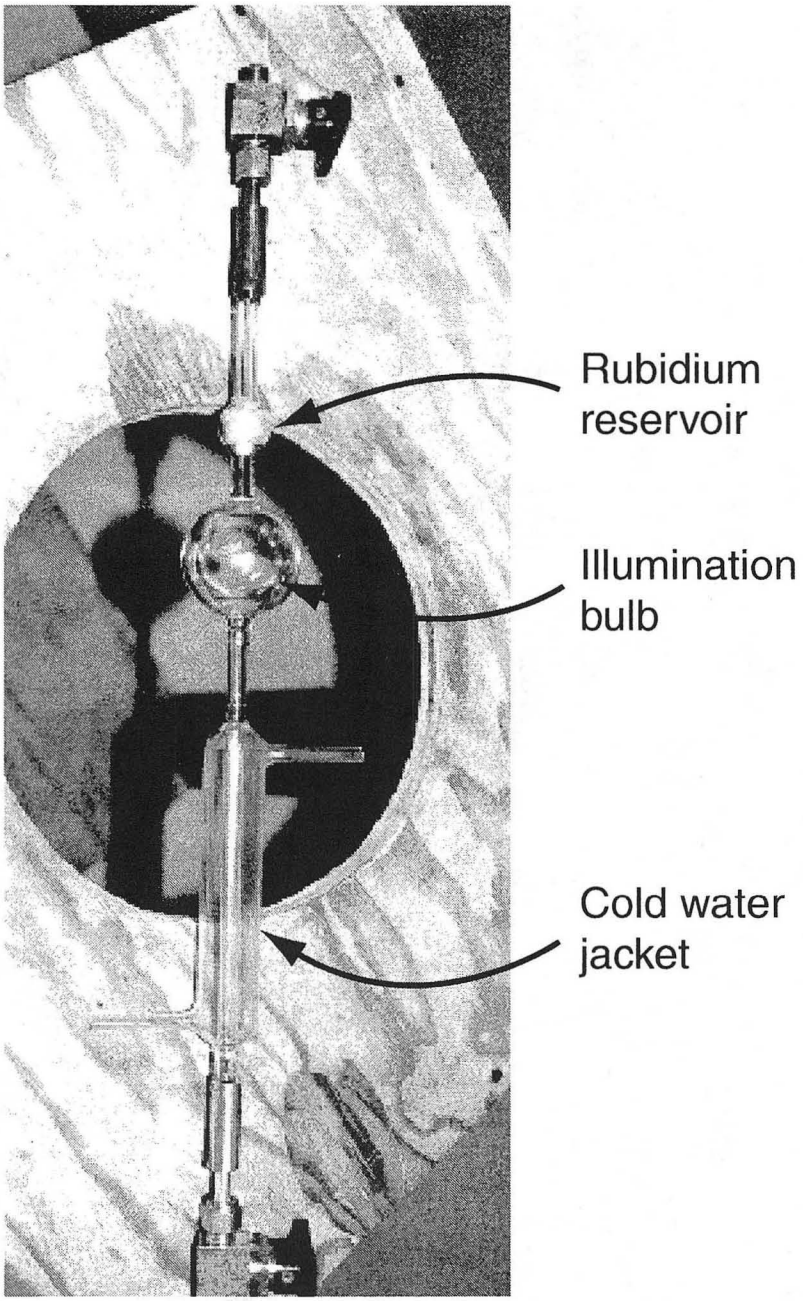

Figure 5.20. Photograph of Flowing Xenon Pumping Cell

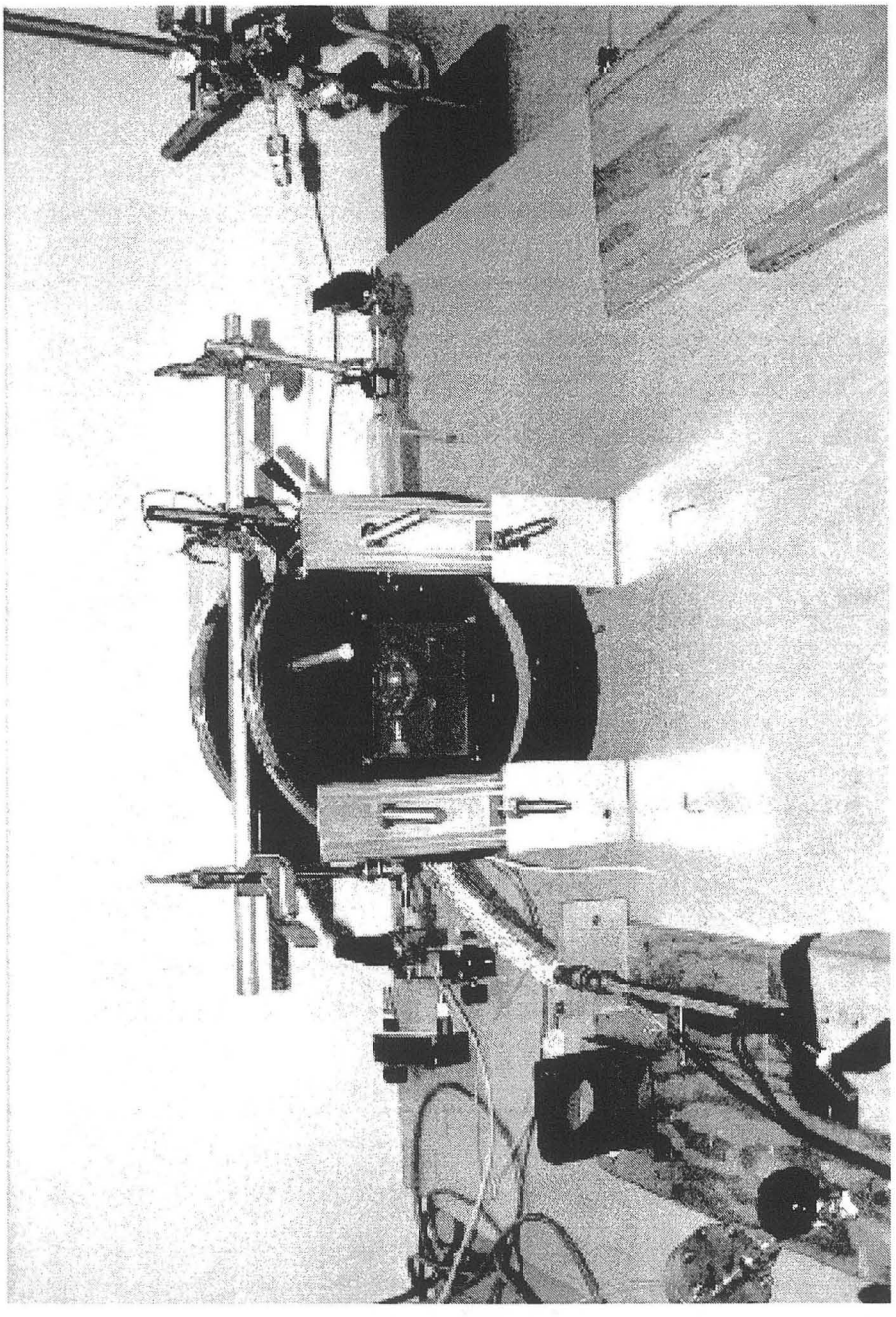

Figure 5.21. Photograph of Optical Pumping Setup

connections between components of the gas lines were made using standard 1/8 *in* or 1/4 *in* teflon tubing and 1/8 *in* or 1/4 *in* brass Swagelok fittings. Permanent brass ferrules were used for all brass/teflon tubing connections, and teflon ferrules were used for the brass/glass connections at the ends of the optical pumping cell and the ends of the sample cell. Finally the laser (J) was a 120 $Watt$ diode laser made by Opto Power operating at the near-infrared wavelength of 795 nm. At first we used the Opto Power Corp. Model OPC-A100-FC/RB water-cooled diode laser but switched to the more reliable OPC-A150-795-RPPS. The light from the diode array was piped through fiber-optic cable, through a quarter-wave circular polarizer (part of the laser head) and into the pumping cell (C). At full power, we found that the beam was intense enough to melt the Pyrex glass cell, so we regularly operated with only half of the laser power simply by turning off four of the eight diodes. (H) and (I) were the gas inlet valve and pressure gauge respectively.

We typically used 1 atm of natural abundance xenon, 1 atm of nitrogen gas, and 5 atm of helium. For all of our experiments we circulated the gases at a constant flow rate of about 0.3 $cfh = 2.4\ mL/s$. The oven was heated to 143 $^{\circ}C$, giving us a rubidium vapor pressure of 0.41 Pa. The sample cell was kept at room temperature. The xenon polarization stayed constant over a 14 *hour* period and averaged 1-2 % on any given day. We found that this high pressure, high flow continuous pumping method generally yielded lower xenon polarization than batch methods; however, its advantages of "instant" and unlimited gases outweighed the few percent loss in polarization.

5.8 Flowing Xenon with SQUID Detection

Figure 5.22 displays two spectra comparing the signal from mineral oil to hyperpolarized xenon produced in our circular flow system. The static field applied to the protons was 0.62 mT and 2.3 mT for xenon, meaning the Larmor frequency was 27 kHz in both cases. Using our SQUID-based spectrometer 1 mL of mineral oil provides a proton NMR signal-to-noise of 2-3 after 80,000 scans. In contrast, the same volume of hyperpolarized xenon gas at a pressure of 1 atm (roughly 10,000

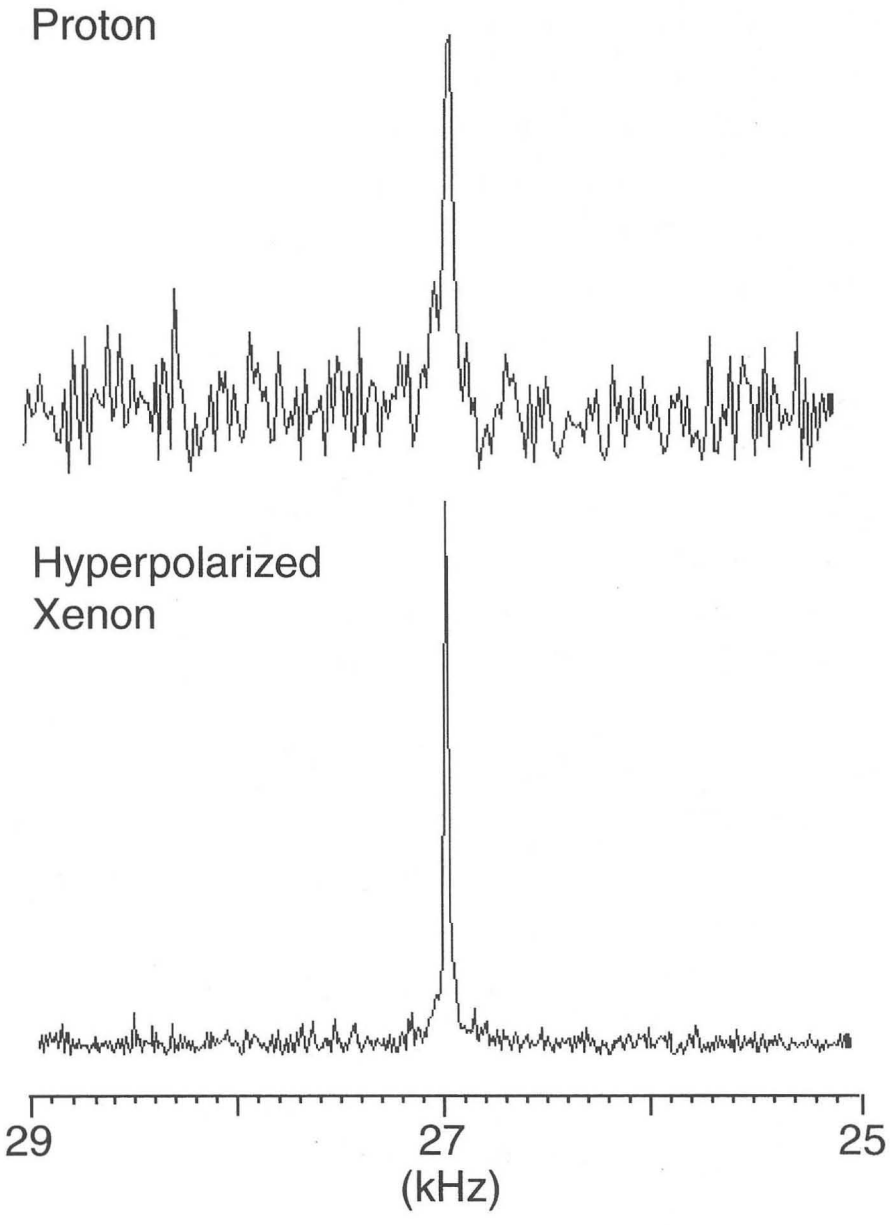

Figure 5.22. **Proton versus Hyperpolarized Flowing Xenon. The resonance frequency was tuned to 27 kHz in both cases. The proton spectrum required 80,000 scans and only 100 scans with a much better SNR for the xenon.**

times fewer nuclei), yields an SNR of 25-30 after only 100 scans. This corresponds to a xenon polarization of approximately 1%, 7 orders of magnitude higher than the thermal polarization. With the new circular flow optical pumping system, we were able to acquire xenon signal with full $\frac{\pi}{2}$ pulses, and the time required for collection was only a few seconds. In contrast, the small mineral oil NMR signal required approximately 2 hours.

5.8.1 Spin Warp Imaging

Two dimensional images were obtained using the standard 2D "spin warp" pulse sequence [11]. Recall from Section 1.4 that there are two ways to traverse the one dimensional (for 1-D projections) k space:

$$\vec{k} = \frac{\gamma \vec{G} t}{2\pi} \tag{5.1}$$

by stepping the gradient (phase encoding) or by stepping the time (frequency encoding). Spin-warp takes advantage of this in order to step through a 2-dimensional k space for 2-dimensional imaging. In one gradient direction, say z, the information is phase encoded while information from the second direction, i.e. x, is frequency encoded. The pulse sequence is shown in Figure 5.23. The z-gradient pulse (G_z) looks like a "ladder" because it represents the fact that this gradient is incremented (starting from a large negative amplitude) each time the sequence is run. The AF pulse and the x gradient (G_x) are the same for each acquisition. The switched negative to positive amplitude of the x gradient gives the "gradient echo" signal shape in the acquisition (ACQ). A walkthrough of what happens to the nuclear magnetization due to this pulse sequence is as follows (neglecting local effects like chemical shift or static field inhomogeneity): first the AF pulse tips the net magnetic moment from equilibrium along z to the $x-y$ plane where the moment precesses at the Larmor frequency. The z-gradient is then turned on causing the individual nuclear spins to precess at different frequencies depending on their location in space along the z-axis. The distribution of resonance frequencies causes the spins to dephase relative to each other, and the stronger the gradient, the greater the dephasing

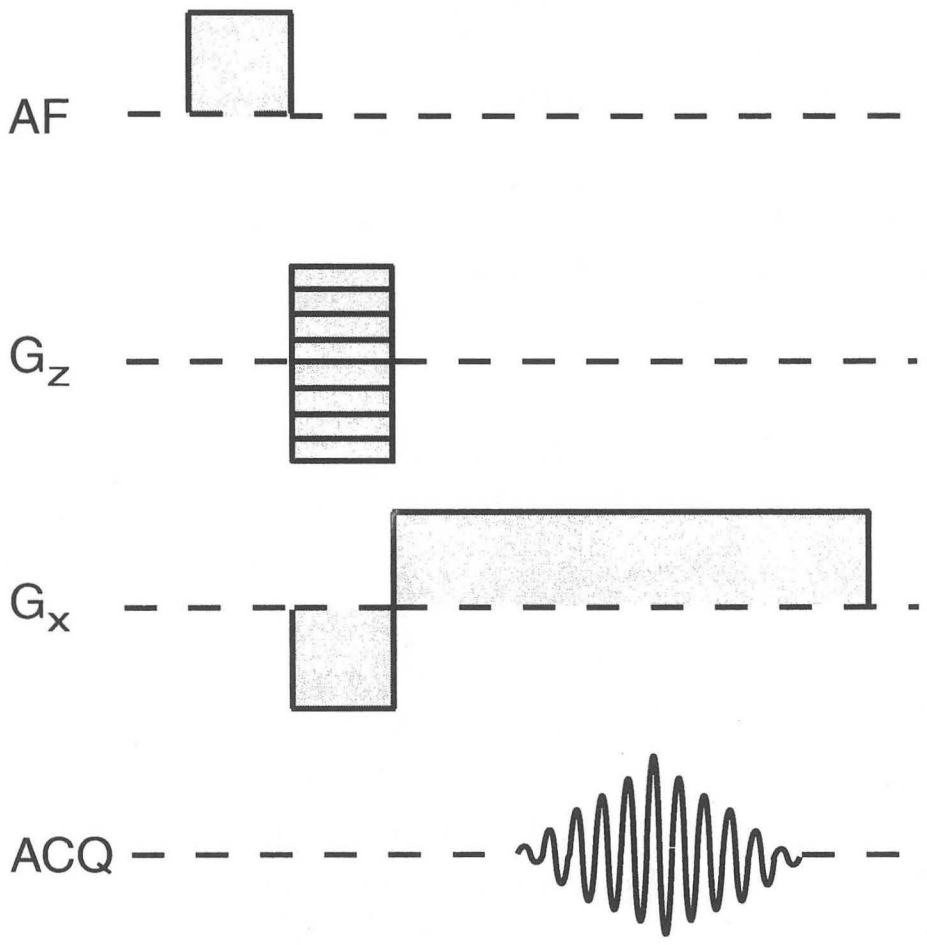

Figure 5.23. Spin warp pulse sequence

for a given amount of time. But also during the phase encoding gradient, the x gradient is turned on. It has the same effect as the z gradient except it modifies the resonance frequency of spins according to position in the x direction. When the z gradient is switched off, the nuclei will stop dephasing due to their distribution along z. Since the x gradient is now reversed from negative to positive, the nuclei will *re-phase* because the slow nuclei (lower precession frequency) will now be the fast nuclei and vice-versa, allowing the previously "lagging" nuclei to "catch up" to the other spins. This causes the refocusing of the magnetization and the formation of the gradient spin echo. The signal is collected over time with the x gradient at a constant amplitude, giving the frequency encoded information. Each time the sequence is run, the amplitude of the z gradient is set to a different value, causing a different amount of dephasing. The information of z nuclei distribution is encoded in the phase of the magnetization.

A full spin warp MRI collection generates a 2-D data set with time on one axis (the directly detected dimension) and z gradient strength on the other (the indirectly detected dimension). A straightforward 2-D Fourier transform will produce the image, but care must be taken to properly convert the dimensions to end up with distance $\times$ distance. After the Fourier transform, the units of the direct dimension will be frequency (Hz) and of the indirect dimension will be inverse gradient strength (i.e. $\frac{cm}{T}$). The conversion from frequency to distance was already discussed previously. Inverse gradient strength can be converted to distance by multiplication by the nuclear gyromagnetic ratio and the length of time that the gradient was turned on.

$$D(cm) = \frac{1}{G}\left(\frac{cm}{T}\right) \times \gamma\left(\frac{Hz}{T}\right) \times t\left(\frac{1}{Hz}\right) \tag{5.2}$$

It is also necessary to calculate the bandwidth or total spread of the indirect dimension (in units of $\frac{cm}{T}$). This is done simply by calculating the reciprocal of the gradient step size, in other words, the reciprocal of the incremental amplitude of the magnetic gradient. This is completely analogous to time-frequency, where the bandwidth of the frequency domain is calculated by taking the reciprocal of the dwell time (the time step of digitization).

5.8.2 Xenon Pictures

Throughout this thesis, as well as my graduate school career, I had always advertised our "Hyperpolarized Xenon, SQUID-detected MRI technique" as being important for medicine. Unfortunately, we were never licensed to work with human or vertebrate subjects, not to mention the fact that our technology never advanced to the point where we could take human or animal MRIs. So the closest that our work ever came to biological subjects was the "finger spectrum" and the poorly resolved chili pepper MRI. All of our work has been for "proof-of-principle." These final MRI pictures are no exception; however, I personally like to think that they have a slight biological aspect to them. Four MRI's are shown in Figures 5.24, 5.25, 5.26(a) and (b). The first two images are of hyperpolarized xenon in, what I like to refer to as, the industrial equivalents of fat and lungs. Figure 5.24 shows xenon in an approximately 1.5 mm thick layer of Dow Corning High Vacuum Grease—a high viscosity, lipophilic lubricant not unlike body fat—coating the bottom of our sample cell. The second image is of xenon in a triangular prism of aerogel. Aerogel is a silicon based, low density, very high surface area, solid foam that was selected as the industrial analog of lungs. Figures 5.26(a) and (b) are visualizations of xenon flowing through a sample cell packed with more synthetic lung material (aerogel).

The heart-shaped blob of vacuum grease is clearly shown in Figure 5.24. The image has a resolution in the x (frequency encoded) dimension of 0.097 cm and 0.072 cm in the z direction. The artery at the bottom of the image is actually the gas delivery tube.

The rough outline of a triangle is demonstrated in Figure 5.25. The rounded corners are due to limits of the resolution which were 0.14 cm and 0.072 cm in the x and z directions, respectively. The distortions in the body of the triangle were due partially to the difficulty in cutting a perfect prism from the very brittle aerogel. Finally, some distortions may also have been due to flow effects of the gas trying to get around the object. Our estimated Reynolds number given the density of the gas and the flow rate was about 100, suggesting that the gas was in

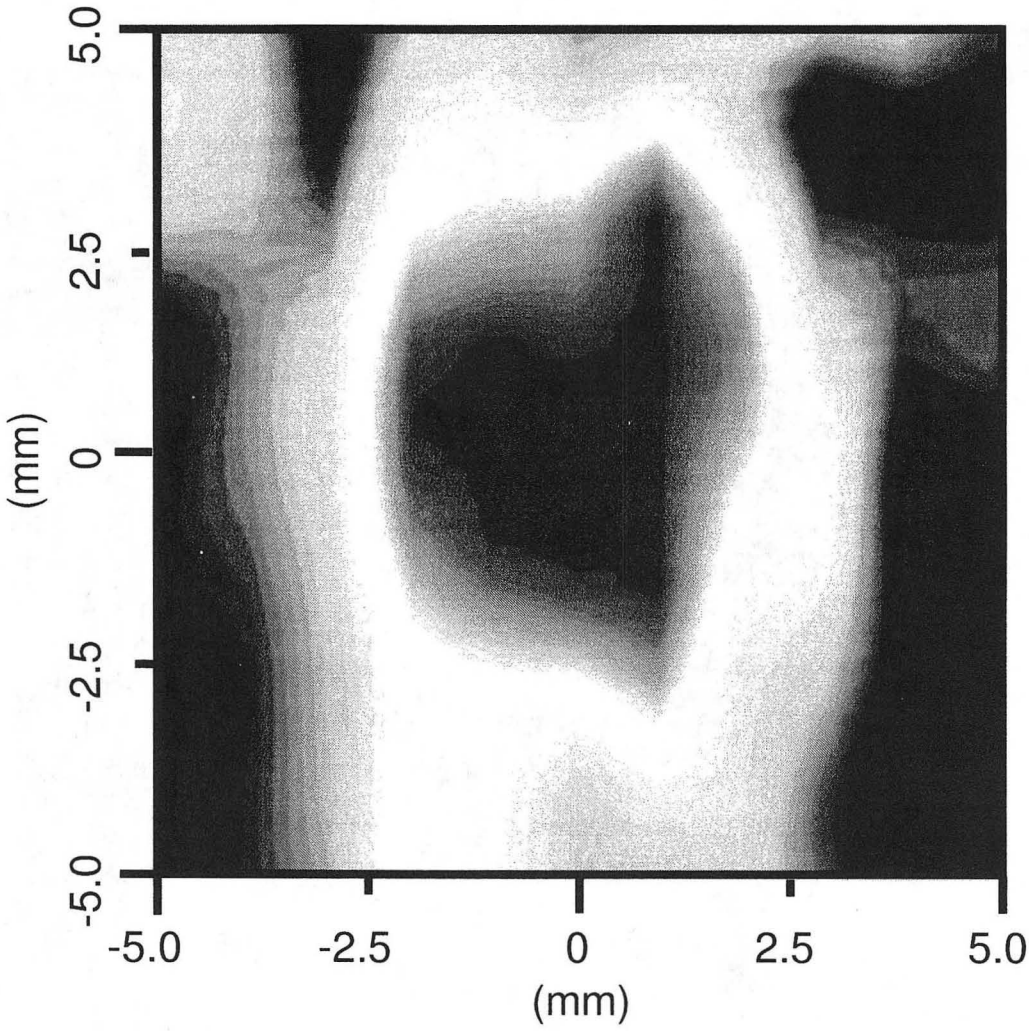

Figure 5.24. Xenon MRI of Vacuum Grease

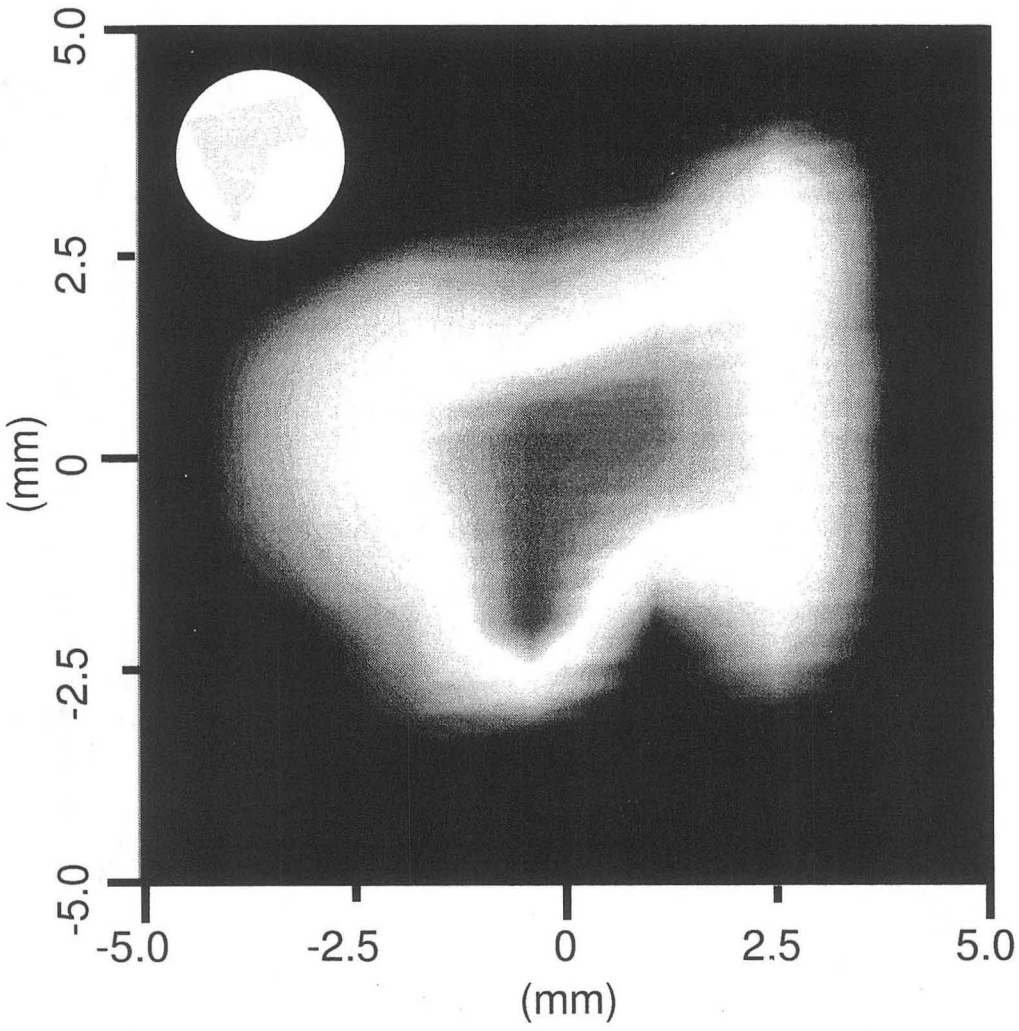

Figure 5.25. Xenon MRI of Triangle of Aerogel

laminar flow. However, the estimate did not take into account the object (aerogel) in the flow path. One interesting point of note is that except for possible flow artifacts, there was no xenon signal from the gas outside of the aerogel. This was due to the xenon adsorbing to the extensive surfaces of the aerogel and effectively increasing the xenon concentration inside the aerogel compared to the surrounding free space. We expect this to happen in real lungs, allowing the differentiation of tissue from large empty pockets without any extra work.

Figures 5.26(a) and (b) are MRIs of xenon flowing through a sample cell packed with aerogel, taken with two different exposure times. This quasi-stroboscopic photography was takes advantage of the non-equilibrium nature of optical pumping. In our spin warp imaging pulse sequence we apply a $\pi/2$ pulse which transfers the xenon magnetization to the transverse plane. After the pulse the enhanced polarization has been used up. Therefore the next $\pi/2$ pulse will only read the new xenon that has entered the sample since the last excitation pulse. Visualization pictures of the xenon flow can be obtained by varying the time between scans (i.e. the recycle delay). Figure 5.26(a) shows the xenon penetration into the aerogel after 0.5 *seconds*. Figure 5.26(b) shows the increased travel of the xenon after 2 seconds. The only difference in imaging procedure between the two pictures is the wait time between scans.

The SQUID used for these experiments was the high noise (160 $\frac{fT}{\sqrt{Hz}}$) "flip chip" magnetometer described in Section 3.5.2. All images were collected in a static field strength of 2.5 mT, corresponding to a xenon Larmor frequency of 29.6 kHz. This resonance frequency was chosen because it was the lowest frequency outside of the SQUID's low frequency intrinsic noise (1/f noise) that was also in a region less inundated with electrical noise from the laboratory surroundings than slightly lower frequencies. The phase encoded gradient was the dB_z/dz gradient, and the frequency encoded dimension was in the x direction. For the first image that we show, Figure 5.24, the magnitude of the x gradient was 8 $\mu T/cm$. The maximum z gradient amplitude was 3 $\mu T/cm$ with a step size of 0.2 $\mu T/cm$. The gradient pulse length was 42 ms. We collected 32 slices of 8192 points with a dwell time of 12.5 μs. Each slice was signal-averaged 400 times with a 2 *second* delay between

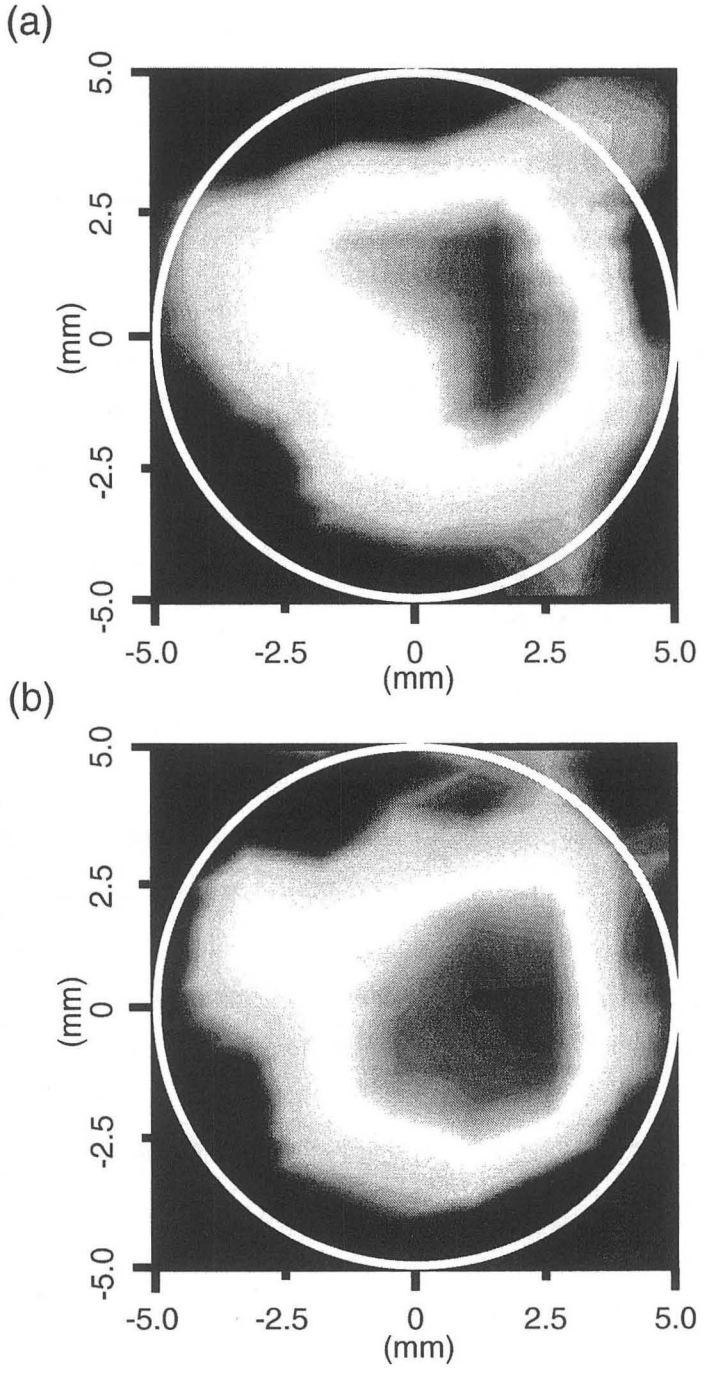

Figure 5.26. Visualization of Xenon Flow through Aerogel

scans. The second image, Figure 5.25, had slightly different collection conditions. The z gradient was the same as the first image, but the x gradient was stronger with a magnitude of .011 mT/cm. We collected 32 slices of 4096 points with a dwell time of 12.5 μs. We averaged 400 scans per slice also with a 2 *second* delay between scans. Finally the last two images were collected with the same settings as the first image except for the scan delay which was 0.5 s for Figure 5.26(a) and 2 s for (b) as previously described.

5.9 The Unfulfilled Promise

Each of the last four xenon images required 8 to 12 *hours* to collect. The long acquisition times were due to the very high noise of the SQUID magnetometer, the long recycle delay, and the high number of averages. Although the bulk gas flow rate would refresh the volume of an empty sample cell in about 500 ms, the presence of the sample effectively slowed the passage of the xenon, and we were forced to use the 2 s delay. Furthermore, we were limited in the magnitude of the z gradient that we could apply. Gradients stronger than 0.003 mT/cm would force a significant amount of magnetic flux through the SQUID, making it difficult to operate. In order to obtain the millimeter resolutions, we increased the gradient pulse length. The consequence of this was a decreased signal amplitude from spin relaxation by the time we were actually collecting signal. Fortunately we had a circular flow system that enabled us to average for as long as we needed to complete the images. The large collection times (as well as the 2 mT static field) do not reflect the true potential of combining circular flow optical pumping with SQUID detection.

Following Greenberg's formalism [160], we can estimate the signal-to-noise ratio of various NMR experiments using standard inductive detection. If one were to use a spectrometer that gives an SNR of 100 in one pulse for 1 mL of water at 1 T, the SNR of the same water sample in 0.05 mT (Earth's field) would be 7 x 10^{-5}, requiring 200 million signal averages just to get an SNR of 1. Now, if one were to take a single NMR scan of 1 mL of 1 atm of gaseous xenon at Earth's field,

one would find that the lower gyromagnetic ratio of xenon coupled with the fewer number of nuclei (gas compared to liquid) would drop the SNR down to around 1.2 x 10^{-10}, requiring a whopping 64 x 10^{18} averages to get an SNR of 1. But, if one were to optically pump the xenon to a polarization of a modest 1% the signal for just a single scan would be 2 billion times larger than the non-hyperpolarized xenon. Unfortunately, that SNR is still only 1/4. That is where better detection equipment could improve the picture.

It is easy to calculate the signal-to-noise ratios for the same cases as above but using a low-T_c SQUID or a good high-T_c SQUID, where a white noise of 1 $fT/Hz^{1/2}$ is achievable, instead of a standard coil. Assuming identical experimental conditions of temperature, sample size, and filling factor, one finds that water at 1 T gives an SNR of about 400. A single pulse on water at Earth's field would give an SNR of 0.04, only 625 scans away from unity SNR. Gaseous xenon thermally polarized at 0.05 mT gives a still miniscule SNR of 1.5 x 10^{-7}, corresponding to 44 x 10^{12} averages to get to an SNR of 1. Using xenon hyperpolarized to 1% again increases the signal by a factor of 2 billion, meaning a SQUID would see an SNR of 300 in only one scan. That is better at Earth's field than the 1 *Tesla* proton imagers in hospitals today.

5.10 High-T_c SQUID Spectroscopy

This final section describes some of the successful spectroscopy accomplished with the high-T_c SQUID instrument. These include NMR signal from phosphorous-31 in phosphoric acid as well as proton and fluorine signal detected simultaneously from a sample of trifluoroacetic acid. We were also able to observe a dynamic nuclear polarization (DNP) enhanced proton signal, and finally I present the first ultra low field observation of chemical shift. In a static field of only 2.54 mT we were able to resolve (hyperpolarized) gaseous xenon from xenon adsorbed to polypropylene. The chemical shift of about 200 *ppm* is only 4.6 Hz compared to the free gas xenon Larmor frequency of 30.07 kHz.

5.10.1 Thermally Polarized Nuclei

One of the distinct advantages of our low field NMR system with SQUID detection was that we could change the strength of the static magnetic field by a quick turn of the knob on the power supply that charged the coils. Furthermore, the SQUID magnetometer was a broadband, untuned detector that allowed us to work with different nuclei without modifying our setup. Previously shown spectra included thermally polarized proton signal and optically polarized xenon signal. Figure 5.27 is a spectrum of thermally polarized ^{31}P in 1 mL of phosphoric acid. The static field of 2.35 mT corresponded to a Larmor frequency of 40 kHz. The peak had a low SNR of about 2:1 and already required 400,000 signal averages.

Figure 5.28 is an NMR spectrum of 1 mL of 2.67 M deuterated trifluoroacetic acid in water. We were able to excite both the ^{1}H and ^{19}F nuclei with a pulse whose frequency was centered between the resonance frequencies of the two nuclei. We were also able to then simultaneously detect both nuclei. The static field of 1.98 mT gave resonance frequencies for the protons and the fluorines of 84.3 kHz (left) and 79.3 kHz (right) respectively. 40,000 scans were acquired to produce the spectrum.

5.10.2 Dynamic Nuclear Polarization

Figure 5.29 shows two proton spectra. Although they are of the same sample, in the same static magnetic field and with the same number of averages, the spectra have different peak amplitudes. Figure 5.29(a) shows the NMR signal from thermally polarized protons in mineral oil, whereas (b) demonstrates the signal enhancement from a technique known as dynamic nuclear polarization (DNP). DNP takes advantage of the fact that the electron gyromagnetic ratio is roughly three orders of magnitude larger than nuclear gyromagnetic ratios; therefore, the thermal equilibrium electron polarization is larger than nuclear spin polarizations by the same amount. This larger polarization can be partially transferred to nuclear spins simply by exciting the electronic spins. As the excited free electrons in the sample relax to equilibrium, they cause spin flips in the "nuclear lattice"

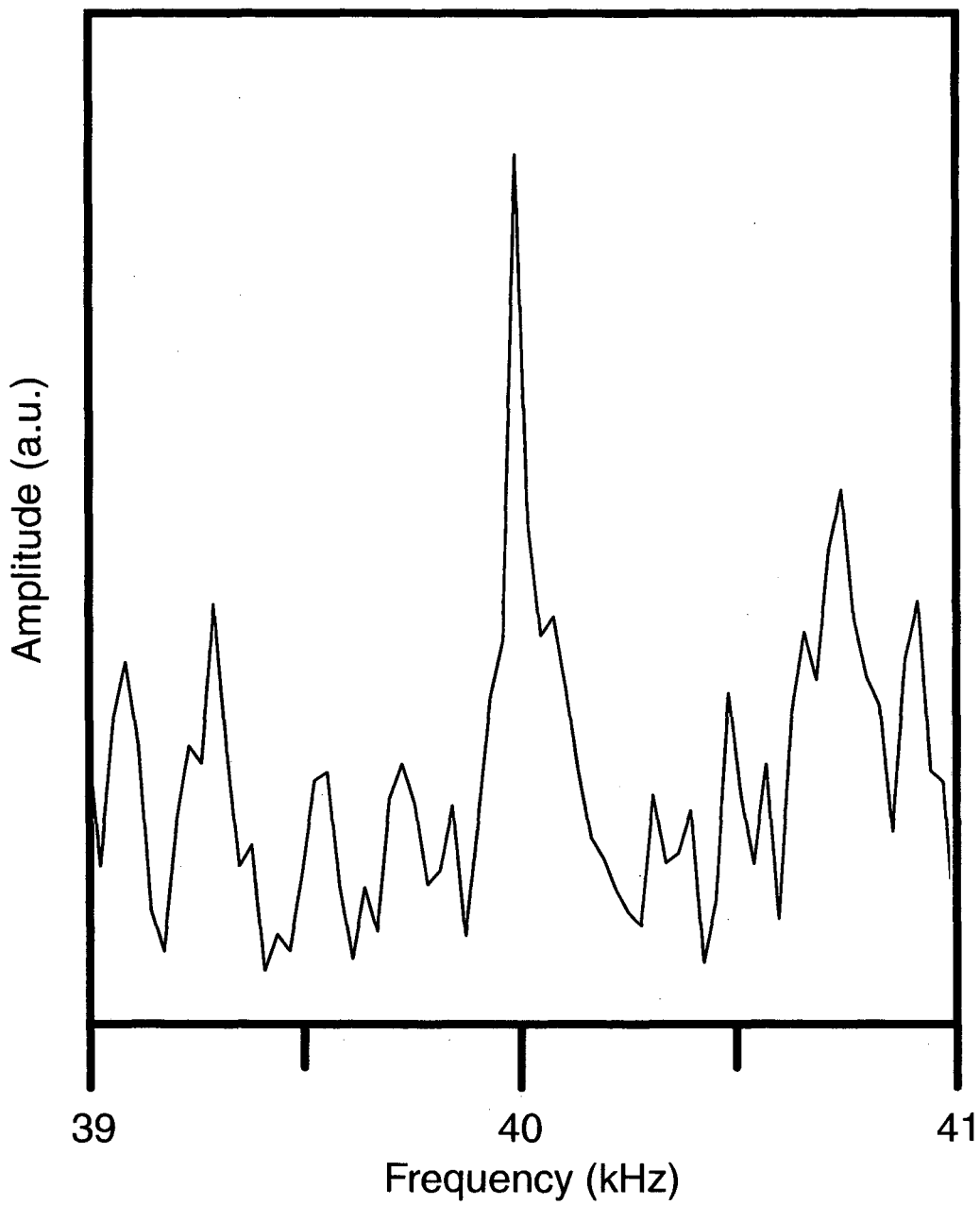

Figure 5.27. Phosphorous-31 NMR in Phosphoric Acid

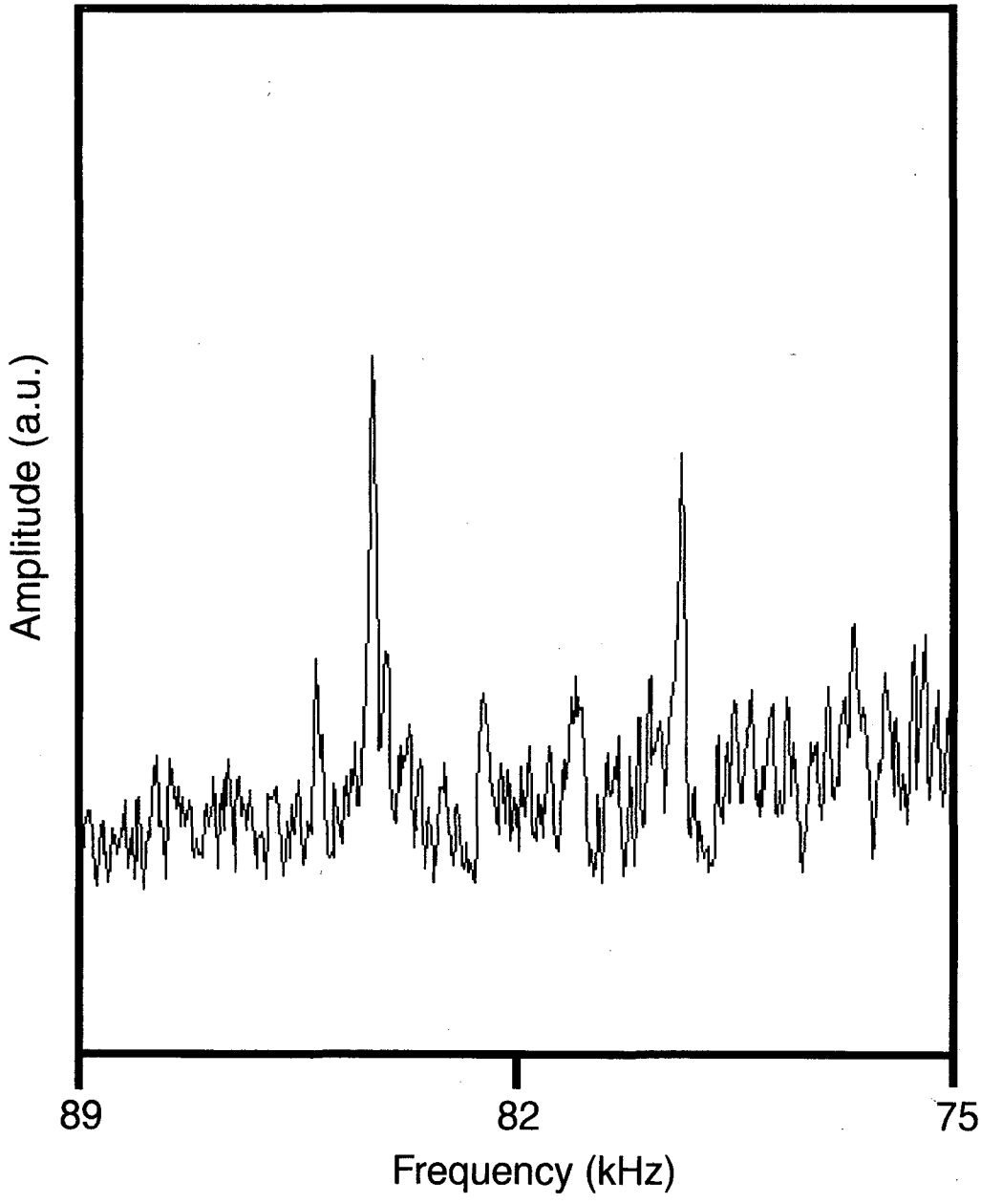

Figure 5.28. Simultaneous Proton and Fluorine NMR

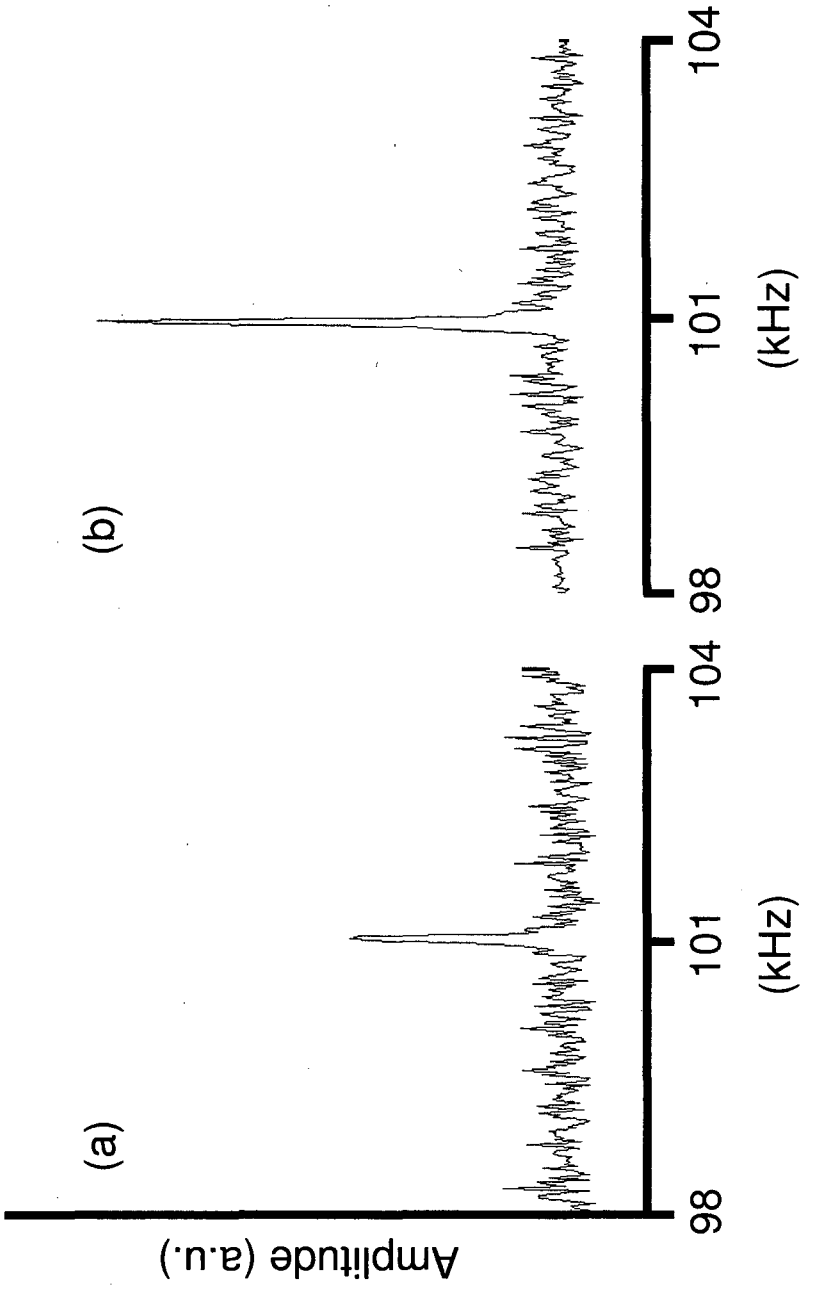

Figure 5.29. **Dynamic Nuclear Polarization Enhancement. (a) show non-enhanced proton signal. (b) DNP enhanced proton signal.**

that they are coupled to. This transfer of electronic spin polarization to nuclear spin polarization via the relaxation of the excited electronic spins is known as the Overhauser effect [161, 162, 8].

DNP is actually similar in some respects to spin exchange optical pumping in that polarization is transferred from excited electronic spins to nuclear spins. The big differences are first in the method of electronic excitation and secondly in the coupling between the electrons and the nuclei. Spin exchange optical pumping excites the valence electrons in an alkali metal electrically and magnetically by light absorption; whereas, DNP excites unpaired electrons only magnetically by manipulating the electron spin resonance (ESR) by radiofrequency pulses (or higher frequency microwave pulses) the same way that nuclear spins are excited in NMR. The other difference between OP and DNP is that DNP's spin cross relaxation Overhauser effect relies on electron-nuclear spin flip-flops by dipole-dipole coupling, scalar (j) coupling or a combination of the two. OP relies on the Fermi contact hyperfine coupling during the collision between the alkali metal and the noble gas; since the polarization transfer is still due to relaxation of the electrons, this is still the Overhauser effect, but with a more specific mechanism. Optical pumping can produce much higher polarizations than DNP, but DNP is useful since only a few systems can be optically pumped efficiently.

The sample we used was a 10 mM solution of 4-amino 2,2,6,6-tetramethyl-1-piperdinyloxyl (TEMPO, a stable free radical commonly used in ESR) in mineral oil. In a static magnetic field of 2.37 mT, the proton resonance frequency was 101.5 kHz and the π_{16} ESR transition [163] was at 116.4 MHz. We excited the electron resonance with a transmitter coil built expressly for this purpose. It was a Helmholtz pair 9.5 cm in diameter and separation of 4.75 cm placed adjacent to the nuclear excitation coils. It was tuned to 116 MHz by addition of a 30 pF Polyflon tuning capacitor soldered in series. The input circuit to the coils contained a PTS-500 frequency synthesizer gated to form pulses by mixing the continuous wave with a TTL pulse from the TecMag Orion using a simple MiniCircuits ZAD-1H mixer. The RF pulses were fed to an ENI 5100L RF Power Amplifier and then to the excitation coil. To obtain the DNP enhanced signal, the electrons of the TEMPO

were excited just before the NMR signal was collected. For the factor of 2 gain in signal, only 1 *watt* of power was applied to the electrons. More power will in general provide larger signal enhancements. However, any more than 1 *watt* of power pulsed to the RF coils caused the SQUID detector to become unstable and unusable.

5.10.3 Ultra Low Field Chemical Shift

Finally Figure 5.30 presents the first observed chemical shift in the weak static field of 2.54 mT. Chemical shift is one of the most important pieces of analytical chemical information for NMR spectroscopists. However, no one has previously detected an NMR chemical shift in the weak fields that we operate in. One of the reasons is that the natural linewidth (due to transverse relaxation, in other words T_2) of the most commonly studied NMR nuclei, protons and carbon, is larger than the chemical shift range of these nuclides in the majority of molecules (not to rule out extraordinary samples) at such low fields. What allowed us to see ultra low field chemical shift was the use of xenon, and in particular, flowing hyperpolarized xenon. First of all, xenon has a wide chemical shift range due to its large and polarizable electron cloud, see for example reference [37]. Being a noble gas, xenon generally has a long relaxation time since it interacts only weakly with most materials. The narrow natural linewidth (from the slow relaxation) in conjunction with the large chemical shift range make xenon uniquely suited for low field NMR spectroscopy. However, the low fields also mean small polarizations and signals, but the long relaxation times make signal averaging impractical. This was another situation where the circular flow optical pumping apparatus really proved its usefulness. Not only was signal enhanced by the optical pumping, but signal averaging was possible since the hyperpolarized gas was constantly replenished. Figure 5.30 features a respectable signal-to-noise in only 2000 scans on a small sample volume of 0.03 mL. The Larmor frequency of the free xenon was 30.070 kHz while the resonance frequency of the xenon adsorbed to the powdered polypropylene was about 30.075 kHz. This corresponds to a 200 ppm chemical shift.

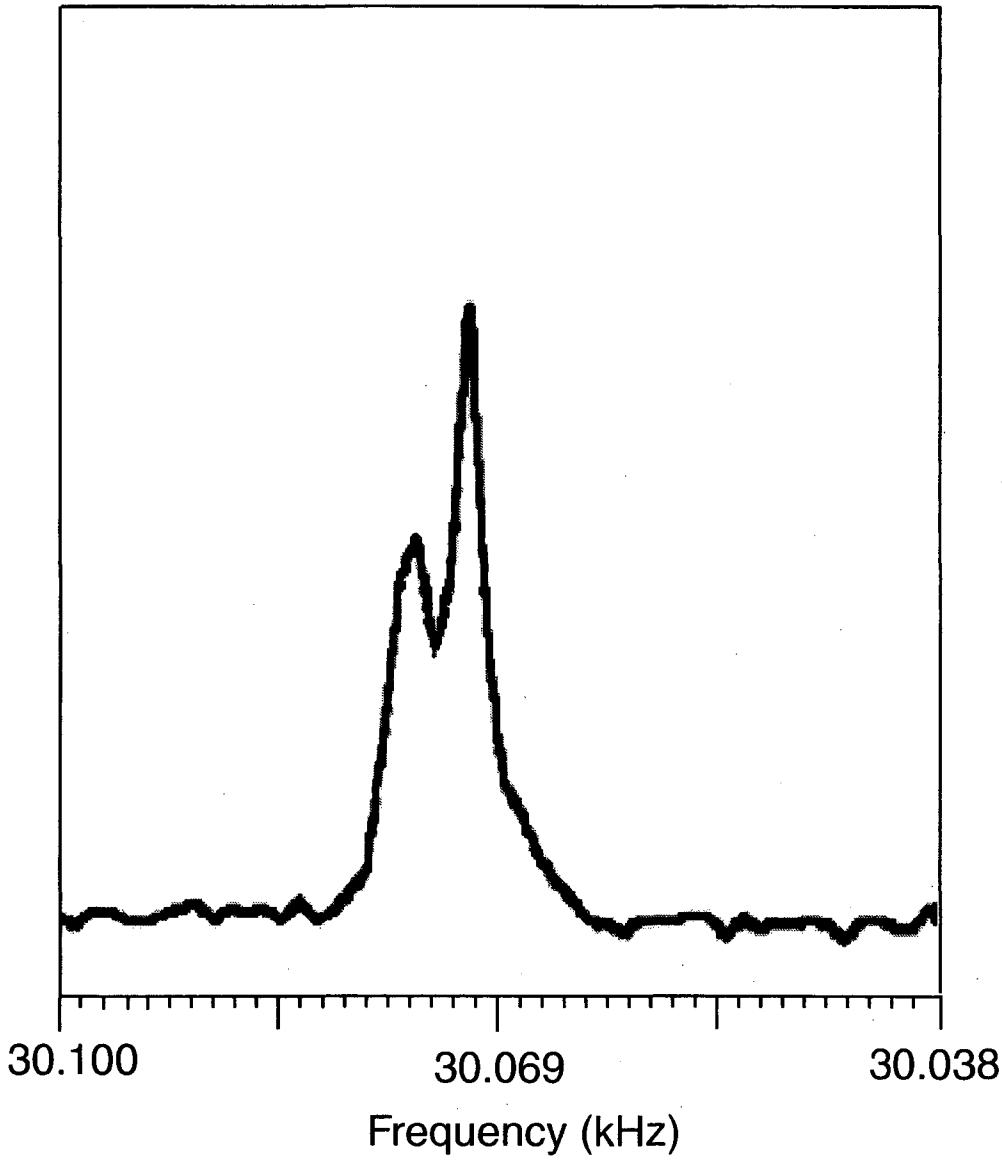

Figure 5.30. **Ultra low field xenon NMR showing chemical shift. The lower frequency peak is from free xenon while the higher frequency peak is from xenon adsorbed to polypropylene.**

One might ask the question, "Besides zero field NQR, why bother with NMR spectroscopy in low fields?" Stronger fields provide larger magnetizations, better spectrometer sensitivity, and higher spectral resolution. Magnetic resonance imaging in low fields might be useful but not magnetic resonance spectroscopy. Perhaps ultra low field NMR cannot compete with high field NMR spectroscopy. But low field MRI can only become a more beneficial technique if analytical information can be gained with the same equipment and at the same time. The ability to distinguish between different nuclides (like the proton and fluorine) or between xenon in different physiochemical environments during an MRI scan would be incredibly powerful. The possibilities include not only nuclide selective or chemical shift selective imaging but perhaps *in vivo* diagnostics and immunoassays as well.

Bibliography

[1] E. Fukushima and B.W. Roeder. *Experimental Pulse NMR: A Nuts and Bolts Approach.* Addison-Wesley Pub. Co., Advanced Book Program, Reading, MA, 1981.

[2] E.L. Hahn. Spin echoes. *Physical Review*, 80(4):580–594, 1950.

[3] T.P. Das and E.L. Hahn. *Nuclear Quadrupole Resonance Spectroscopy*, volume 1 of *Solid State Physics. Supplement.* Academic Press, New York, 1958.

[4] A. Abragam. *Principles of Nuclear Magnetism.* Oxford University Press, 1961.

[5] M. Mehring. *High Resolution NMR Spectroscopy in Solids.* Springer, Berlin, 2nd edition, 1983.

[6] R.R. Ernst, G. Bodenhausen, and A. Wokaun. *Principles of Nuclear Magnetic Resonance in One and Two Dimensions.* Oxford, 1994.

[7] L. Emsley, D.D. Laws, and A. Pines. Lectures on pulsed NMR. In B. Maraviglia, editor, *Proceedings of the International School of Physics "Enrico Fermi"*, Magnetic Resonance and Brain Function: Approaches from Physics, pages 45–210. Societa Italiana di Fisica, 3rd edition, 1999.

[8] C.P. Slichter. *Principles of Magnetic Resonance.* Springer-Verlag, Berlin, 3rd edition, 1996.

[9] P.C. Lauterbur. Image formation by induced local interactions–examples employing nuclear magnetic resonance. *Nature*, 242(5394):190–191, 1973.

[10] P. Mansfield and P.K. Grannell. NMR diffraction in solids. *Journal of Physics C–Solid State Physics*, 6(22):L422–L426, 1973.

[11] P.T. Callaghan. *Principles of Nuclear Magnetic Resonance Microscopy.* Oxford, 1991.

[12] P.C. Lauterbur. Magnetic resonance zeugmatography. *Pure and Applied Chemistry*, 40(1–2):149–157, 1974.

[13] A.N. Garroway, P.K. Grannell, and P. Mansfield. Image formation in NMR by a selective irradiative process. *Journal of Physics C–Solid State Physics*, 7(24):L457–L462, 1974.

[14] G.L. Brownell, T.F. Budinger, P.C. Lauterbur, and P.L. McGeer. Positron tomography and nuclear magnetic resonance imaging. *Science*, 215(4533):619–626, 1982.

[15] D.G. Gadian. *Nuclear Magnetic Resonance and its Application to Living Systems.* Oxford University Press, Oxford, 1982.

[16] P. Mansfield and P.G. Morris. *NMR Imaging in Biomedicine.* Academic Press, New York, 1982.

[17] T.F. Budinger and P.C. Lauterbur. Nuclear magnetic resonance technology for medical studies. *Science*, 226(4672):288–298, 1984.

[18] P.C. Lauterbur. NMR images of microscopic flow. *Nature*, 336(6197):310, Nov 1988.

[19] F.W. Wehrli. From NMR diffraction and zeumatography to modern imaging and beyond. *Prog. NMR Spectrosc.*, 28:87–135, 1995.

[20] T.M. de Swiet. Diffusive edge enhancement in imaging. *Journal of Magnetic Resonance*, 109(1):12–18, Oct 1995.

[21] Y.Xia. Contrast in NMR imaging and microscopy. *Concepts in Magnetic Resonance*, 8:205–225, 1996.

[22] W.S. Price. NMR imaging. *Annual Reports on NMR Spectroscopy*, 35:140–191, 1998.

[23] A. Mohoric, J. Stepisnik, M. Kos, and G. Planinsic. Self-diffusion imaging by spin echo in Earth's magnetic field. *Journal of Magnetic Resonance*, 136(1):22–26, Jan 1999.

[24] M. Gatzke, G.D. Cates, B. Driehuys, D. Fox, W. Happer, and B. Saam. Extraordinarily slow nuclear-spin relaxation in frozen laser-polarized Xe-129. *Physical Review Letters*, 70(5):690–693, Feb 1993.

[25] A. Kastler. Quelques suggestions concernant la production optique et la detection optique dune inegalite de population des niveaux de quantification spatiale des atomes–application a lexperience de stern et gerlach et a la resonance magnetique. *Journal de Physique et le Radium*, 11(6):255–265, 1950.

[26] J. Brossel, A. Kastler, and J. Winter. Creation optique dune inegalite de population entre les sous-niveaux zeeman de letat fondamental des atomes. *Journal de Physique et le Radium*, 13(12):668, 1952.

[27] J. Brossel, B. Cagnac, and A. Kastler. Resonance magnetique sur des atomes orientes optiquement. *Journal de Physique et le Radium*, 15(1):6–8, 1954.

[28] A. Kastler. Optical methods of atomic orientation and of magnetic resonance. *Journal of the Optical Society of America*, 47(6):460–465, 1957.

[29] A. Kastler. Methodes optiques de production et de detection des moments magnetiques longitudinaux Mz et transversaux Mt dune collection datomes. *Physica*, 33(1):73, 1967.

[30] R.J. McNeal. Disorientation cross sections in optical pumping. *The Journal of Chemical Physics*, 37, 1962.

[31] R.M. Herman. Noble-gas-induced rubidium spin disorientation. *Physical Review*, 136(6A):A1576–A1582, 1964.

[32] R.M. Herman. Theory of spin exchange between optically pumped rubidium and foreign gas nuclei. *Physical Review*, 137(4A):A1062–A1065, 1965.

[33] C.C. Bouchiat, M.A. Bouchiat, and L.C. Pottier. Evidence for Rb-rare-gas molecules from the relaxation of polarized Rb atoms in a rare gas. Theory. *Physical Review*, 181(1):144–165, May 1969.

[34] M.A. Bouchiat, J. Brossel, and L.C. Pottier. Evidence for Rb-rare-gas molecules from the relaxation of polarized Rb atoms in a rare gas. Experimental results. *The Journal of Chemical Physics*, 56(7):3703–3714, Apr 1972.

[35] M.A. Bouchiat, T.R. Carver, and C.M. Varnum. Nuclear polarization in He-3 gas induced by optical pumping and dipolar exchange. *Physical Review Letters*, 5(8):373–375, 1960.

[36] B.C. Grover. Noble-gas NMR detection through noble-gas-rubidium hyperfine contact interaction. *Physical Review Letters*, 40(6):391–392, Feb 1978.

[37] T. Pietrass and H.C. Gaede. Optically polarized ^{129}Xe in NMR spectroscopy. *Advanced Materials*, 7(10):826–838, 1995.

[38] Y.Q. Song, B.M. Goodson, and A. Pines. NMR and MRI using laser-polarized xenon. *Spectroscopy*, 14(7):26–33, Jul 1999.

[39] B.M. Goodson. Using injectable carriers of laser-polarized noble gases for enhancing NMR and MRI. *Concepts in Magnetic Resonance*, 11(4):203–223, 1999.

[40] B.M. Goodson. *Nuclear Magnetic Resonance of Laser-Polarized Noble Gases in Molecules, Materials, and Organisms.* PhD thesis, University of California, Berkeley, 1999.

[41] F.D. Colegrove, L.D. Schearer, and G.K. Walters. Polarization of He-3 gas by optical pumping. *Physical Review*, 132(6):2561–2572, 1963.

[42] R.L. Gamblin and T.R. Carver. Polarization and relaxation processes in He-3 gas. *Physical Review*, 138(4A):A946, 1965.

[43] M. Leduc, F. Laloe, and J. Brossel. Optical pumping of Ne-21. *Comptes Rendus Hebdomadaires des Seances de L'Academie des Sciences Serie B*, 271(5):342, 1970.

[44] A. Noel, M. Leduc, and F. Laloe. Orientation of excited levels of Ne-21 by optical pumping in a discharge. *Comptes Rendus Hebdomadaires des Seances de L'Academie des Sciences Serie B*, 274(1):77, 1972.

[45] S.E. Barrett, R. Tycko, L.N. Pfeiffer, and K.W. West. Directly detected nuclear magnetic resonance of optically pumped GaAs quantum wells. *Physical Review Letters*, 72:1368–1372, 1994.

[46] R. Tycko and J.A. Reimer. Optical pumping in solid state nuclear magnetic resonance. *Journal of Physical Chemistry*, 100:13240–13250, 1996.

[47] T. Pietrass, A. Bifone, T. Room, and E.L. Hahn. Optically enhanced high-field NMR of GaAs. *Physical Review B*, 53:4428–4433, 1996.

[48] R. Tycko. Optical pumping in indium phosphide: P-31 NMR measurements and potential for signal enhancement in biological state NMR. *Solid State Nuclear Magnetic Resonance*, 11:1–9, 1998.

[49] T. Pietrass and M. Tomaselli. Optically pumped NMR in CdS single crystals. *Physical Review B*, 59:1986–1989, 1999.

[50] J.C. Camparo, R.P. Frueholz, and C.H. Volk. Inhomogeneous light shift in alkali-metal atoms. *Physical Review A*, 27(4):1914–1924, 1983.

[51] H.W. Long. *Applications of Highly Spin-Polarized Xenon in NMR.* PhD thesis, University of California, Berkeley, 1993.

[52] W. Happer, E. Miron, S. Schaefer, D. Schreiber, W.A. van Wijngaarden, and X. Zeng. Polarization of the nuclear spins of noble-gas atoms by spin-exchange with optically pumped alkali-metal aroms. *Physical Review A*, 29(6):3092–3110, 1984.

[53] N.D. Bhaskar, W. Happer, and T. McClelland. Efficiency of spin exchange between rubidium spins and Xe-129 nuclei in a gas. *Physical Review Letters*, 49(1):25–28, 1982.

[54] T.G. Walker and W. Happer. Spin-exchange optical pumping of noble-gas nuclei. *Reviews of Modern Physics*, 69(2):629–642, April 1997.

[55] B. Larson, O. Hausser, P.P.J. Delheiji, D.M. Whittal, and D. Thiessen. Optical pumping of Rb in the presence of high-pressure He-3 buffer gas. *Physical Review A*, 44(5), Sep 1991.

[56] G.D. Cates, R.J. Fitzgerald, A.S. Barton, P. Bogorad, M.Gatzke, N.R. Newbury, and B. Saam. Rb-^{1}29Xe spin-exchange rates due to binary and three-body collisions at high Xe pressures. *Physical Review A*, 45(7):4631–4639, Apr 1992.

[57] T.G. Walker. Estimates of spin-exchange parameters for alkali-metal noble-gas pairs. *Physical Review A*, 40(9):4959–4963, Nov 1989.

[58] R.C. Jaklevic, J. Lambe, A.H. silver, and J.E. Mercereau. Quantum interference effects in Josephson tunneling. *Physical Review Letters*, 12:159–160, 1964.

[59] E.P. Day. Detection of NMR using a Josephson-junction magnetometer. *Physical Review Letters*, 29:540, 1972.

[60] R.V. Chamberlin, L.A. Moberly, and O.G. Symko. High-sensitivity magnetic resonance by SQUID detection. *Journal of Low Temperature Physics*, 35(3/4):337–347, 1979.

[61] J. Clarke. Superconducting quantum interference devices for low frequency measurements. In B. Schwartz and S. Foner, editors, *Superconductor Applications: SQUIDs and Machines*, chapter 3, pages 67–124. Plenum Press, New York, 1977.

[62] T. Van Duzer and C.W. Turner. *Principles of Superconductive Devices and Circuits.* Elsevier North Holland, New York, 1981.

[63] T. Ryhänsen, H. Seppä, R. Ilmoniemi, and J. Knuutila. SQUID magnetometers for low-frequency applications. *Journal of Low Temperature Physics*, 76:287–386, 1989.

[64] A. Barone, editor. *Principles and Applications of Superconducting Quantum Interference Devices.* World Scientific Publishing Company, Singapore, 1992.

[65] H. Weinstock and R.W. Ralston, editors. *The New Superconducting Electronics.* Kluwer Academic Publishers, Dordrecht, 1993.

[66] H. Weinstock, editor. *SQUID Sensors: Fundamentals, Fabrication and Applications.* Kluwer Academic Publishers, Netherlands, 1996.

[67] J. Bardeen, L.N. Cooper, and J.R. Schrieffer. Microscopic theory of superconductivity. *Physical Review*, 106(1):162–164, 1957.

[68] J. Bardeen, L.N. Cooper, and J.R. Schrieffer. Theory of superconductivity. *Physical Review*, 108(5):1175–1204, 1957.

[69] E.A. Lynton. *Superconductivity.* John Wiley and Sons Inc., New York, 1962.

[70] R.P. Feynman, R.B. Leighton, and M. Sands. *The Feynman Lectures on Physics*, volume III. Addison-Wesley, Reading, MA, 1963.

[71] M. Tinkham. *Introduction to Superconductivity.* McGraw-Hill, New York, 1975.

[72] F. London. *Superfluids*, volume I. John Wiley and Sons, Inc., New York, 1950.

[73] B.D. Josephson. Possible new effects in superconductive tunneling. *Physics Letters*, 1:251–253, 1962.

[74] B.D. Josephson. Supercurrents through barriers. *Advances in Physics*, 14:419–451, 1965.

[75] B.D. Josephson. Weakly coupled superconductors. In R.D. Parkes, editor, *Superconductivity*, volume I. Marcel Dekker, New York, 1969.

[76] V. Ambegaokar and A. Baratoff. Tunneling between superconductors. *Physical Review Letters*, 10:486–491, Jun 1963.

[77] V. Ambegaokar and A. Baratoff. Tunneling between superconductors. *Physical Review Letters*, 11, Jul 1963.

[78] J. Clarke. SQUID Fundamentals. In H. Weinstock, editor, *SQUID Sensors: Fundamentals, Fabrication and Applications*, pages 1–62. Kluwer Academic Publishers, Netherlands, 1996.

[79] D.M. TonThat. *DC SQUID Spectrometers for Nuclear Quadrupole and Low Field Nuclear Magnetic Resonance Spectroscopy.* PhD thesis, University of California, Berkeley, 1998.

[80] M.B. Ketchen and J.M. Jaycox. Ultra-low noise tunnel junction dc SQUID with a tightly coupled planar input coil. *Applied Physics Letters*, 40:736–738, 1982.

[81] J.M. Jaycox and M.B. Ketchen. Planar coupling scheme for ultra low noise dc SQUIDs. *IEEE Transactions on Magnetism*, MAG-17:400–403, 1981.

[82] H.H. Zappe and B.S. Landman. Experimental investigation of resonances in low-Q Josephson interferometer devices. *Journal of Applied Physics*, 49(7):4149–4154, 1978.

[83] K. Enpuku, S. Kohjiro, and K. Yoshida. Noise characteristics of a dc SQUID with a resistively shunted inductance. *Journal of Applied Physics*, 60(12):4218–4223, 1986.

[84] S. Kohjiro, K. Enpuku, K. Yoshida, and K. Yamafuji. Experimental study of noise characteristics of large-β dc SQUID with resistively shunted inductance. *Japanese Journal of Applied Physics*, 27(10):1871, 1988.

[85] J.E. Zimmerman. Sensitivity enhancement of superconducting quantum interference devices through the use of fractional-turn loops. *Journal of Applied Physics*, 42:4483–4487, 1971.

[86] F. Ludwig, E. Dantsker, R. Kleiner, D. Koelle, J. Clarke, S. Knappe, D. Drung, H. Koch, N.M. Alford, and T.W. Button. Integrated high T_c multiloop magnetometer. *Applied Physics Letters*, 66(11):1418–1420, Mar 1995.

[87] F. Ludwig, E. Dantsker, D. Koelle, R. Kleiner, A.H. Miklich, D.T. Nemeth, J. Clarke, D. Drung, S. Knappe, and H. Koch. High-T_c multilayer magnetometers with improved 1/f noise. *IEEE Transactions on Applied Superconductivity*, 5(2):2919–2922, Jun 1995.

[88] F. Ludwig, D. Koelle, E. Dantsker, D.T. Nemeth, A.H. Miklich, J. Clarke, and R.E. Thomson. Low noise $YBa_2Cu_3O_{7-x}$ / $SrTiO_3$ / $YBa_2Cu_3O_{7-x}$ multilayers for improved superconducting magnetometers. *Applied Physics Letters*, 66(3):373–375, 1995.

[89] J.E. Zimmerman, P. Thiene, and J.T. Harding. Design and operation of stable rf-based superconducting point-contact quantum devices, and a note on the properties of perfectly clean metal contacts. *Journal of Applied Physics*, 41:1572–1580, 1970.

[90] D. Drung, R. Cantor, M. Peters, H.J. Scheer, and H. Koch. Low-noise high-speed dc superconducting quantum interference device magnetometer with

simplified feedback electronics. *Applied Physics Letters*, 57(4):406–408, Jul 1990.

[91] D. Drung, H. Matz, and H. Koch. A 5-MHz bandwidth SQUID magnetometer with additional positive feedback. *Review of Scientific Instruments*, 66(4), Apr 1995.

[92] G.N. Hounsfield. Computerized transverse axial scanning (tomography). 1. description of system. *British Journal of Radiology*, 46(552):1016–1022, 1973.

[93] M.S. Albert, G.D. Cates, B. Driehuys, W. Happer, B. Saam, C.S. Springer, and A. Wishnia. Biological Magnetic-Resonance-Imaging using laser polarized Xe-129. *Nature*, 370(6486):199–201, July 1994.

[94] Y.Q. Song, H.C. Gaede, T. Pietrass, G.A. Barrall, G.C. Chingas, M.R. Ayers, and A. Pines. Spin-polarized Xe-129 gas imaging of materials. *Journal of Magnetic Resonance*, 115(1):127–130, Jul 1995.

[95] H. Middleton, R.D. Black, B. Saam, G.D. Cates, G.P. Cofer, R. Guenther, W. Happer, L.W. Hedlund, G.A. Johnson, K. Juvan, and J. Swartz. MR-imaging with hyperpolarized He-3 gas. *Magnetic Resonance in Medicine*, 33(2):271–275, Feb 1995.

[96] P. Bachert, L.R. Schad, M. Bock, M.V. Knopp, M. Ebert, T. Grossman, W. Heil, D. Hoffmann, R. Surkau, and E.W. Otten. Nuclear magnetic resonance imaging of airways in humans with use of hyperpolarized He-3. *Magnetic Resonance in Medicine*, 36(2):192–196, Aug 1996.

[97] G. Navon, Y.Q. Song, T. Room, S. Appelt, R.E. Taylor, and A. Pines. Enhancement of solution NMR and MRI with laser-polarized xenon. *Science*, 271(5257):1848–1851, Mar 1996.

[98] M.S. Albert and D. Balamore. Development of hyperpolarized noble gas MRI. *Nuclear Instrments and Methods in Physics Research Section A*, 402:441–453, 1998.

[99] H.C. Seton, D.M. Bussell, J.M.S. Hutchison, and D.J. Lurie. Use of a dc-SQUID receiver preamplifier in a low-field MRI system. *IEEE Transactions on Applied Superconductivity*, 5(2):3218–3221, Jun 1995.

[100] H.C. Seton, J.M.S. Hutchison, and D.M. Bussell. A 4.2 K receiver coil and SQUID amplifier used to improve the SNR of low-field magnetic resonance images of the human arm. *Measurement Science & Technology*, 8(2):198–207, Feb 1997.

[101] H.C. Seton, J.M.S. Hutchison, and D.M. Bussell. A tuned SQUID amplifier for MRI based on a DOIT flux locked loop. *IEEE Transactions on Applied Superconductivity*, 7(2):3213–3216, Jun 1997.

[102] M. P. Augustine, A. Wong-Foy, J. L. Yarger, M. Tomaselli, D. M. TonThat, J. Clarke, and A. Pines. Low field magnetic resonance images of polarized noble gases obtained with a dc superconducting quantum interference device. *Applied Physics Letters*, 72(15):1908–1910, 1998.

[103] B. Saam, N. Drukker, and W. Happer. Edge enhancement observed with hyperpolarized He-3. *Chemical Physics Letters*, 263(3–4):481–487, Dec 1996.

[104] C.H. Tseng, G.P. Wong, V.R. Pomeroy, R.W. Mair, D.P. Hinton, D. Hoffmann, R.E. Stoner, F.W. Hersman, D.G. Cory, and R.L. Walsworth. Low-field MRI of laser polarized noble gas. *Physical Review Letters*, 81(17):3785–3788, Oct 1998.

[105] M. Albert, A. Venkatesh, A. Zhang, C.H. Oh, F. Jolesz, L. Kubatina, and D. Balamore. Vey low-field hyperpolarized noble gas MRI *in vivo*. In *41st Experimental Nuclear Magnetic Resonance Conference, Asilomar, CA*, number Poster 205 in Biomedical, Apr 2000.

[106] M.P. Augustine and K.W. Zilm. Optical pumping magnetic resonance in high magnetic fields: Characterization of nuclear relaxation during pumping. *The Journal of Chemical Physics*, 105(8):2998–3011, 1996.

[107] M.P. Augustine and K.W. Zilm. Optical pumping magnetic resonance in high magnetic fields: Characterization of the optical properties of Rb-Xe mixtures. *Molecular Physics*, 89(3):737–752, 1996.

[108] M.P. Augustine and K.W. Zilm. Optical pumping magnetic resonance in high magnetic fields: Measurement of high field spin exchange cross sections. *Chemical Physics Letters*, 280(1–2):24–30, 1997.

[109] D.M. TonThat, M. Ziegeweid, Y.Q. Song, E.J. Munson, S. Appelt, A. Pines, and J. Clarke. SQUID detected NMR of laser-polarized xenon at 4.2 K and at frequencies down to 200 Hz. *Chemical Physics Letters*, 272(3–4):245–249, Jun 1997.

[110] W.A. Nierenberg, N.F. Ramsey, and S.B. Brody. Measurements of nuclear quadrupole moment interactions. *Physical Review*, 70:773, 1946.

[111] I.I. Rabi, S. Millman, P. Kusch, and J.R. Zacharias. The molecular beam resonance method for measuring nuclear magnetic moments. *Physical Review*, 55:526, 1939.

[112] M. Bloom and R.E. Norberg. Transient nuclear induction signals associated with pure quadrupole interactions. *Physical Review*, 93:638–639, 1954.

[113] E.L. Hahn and B. Herzog. Anisotropic relaxation of quadrupole spin echoes. *Physical Review*, 93:639–640, 1954.

[114] M. Bloom, E.L. Hahn, and B. Herzog. Free magnetic induction in nuclear quadrupole resonance. *Physical Review*, 97(6):1699–1709, 1954.

[115] A.G. Anderson. Nonresonant nuclear spin absorption in lithium, sodium, and aluminum. *Physical Review*, 115(4):863–868, 1959.

[116] N.F. Ramsey and R.V. Pound. Nuclear audiofrequency spectroscopy by resonant heating of the nuclear spin system. *Physical Review*, 81:278–280, 1951.

[117] R.V. Pound. Nuclear electric quadrupole interactions in crystals. *Physical Review*, 79(4):685–702, 1950.

[118] A.G. Redfield. Pure nuclear electric quadrupole resonance in impure copper. *Physical Review*, 130(2):589–595, 1963.

[119] R.E. Slusher and E.L. Hahn. Sensitive detection of nuclear quadrupole interactions in solids. *Physical Review*, 166(2):332–347, 1968.

[120] J.C. Koo. PhD thesis, University of California, Berkeley, 1969.

[121] J. Koo and Y.-N. Hsieh. ^{14}N nuclear quadrupole coupling constants in imidazole. *Chemical Physics Letters*, 9(3):238–241, 1971.

[122] D.T. Edmonds. Nuclear quadrupole double resonance. *Physics Reports*, 29(4):234–290, 1977.

[123] D.P. Weitekamp, A. Bielecki, D. Zax, K. Zilm, and A. Pines. Zero-field nuclear magnetic resonance. *Physical Review Letters*, 50(22):1807–1810, 1983.

[124] D.B. Zax. *Fourier Transform Zero Field NMR and NQR.* PhD thesis, University of California, Berkeley, 1984.

[125] D.B. Zax, A. Bielecki, K. Zilm, A. Pines, and D.P. Weitekamp. Zero field NMR and NQR. *The Journal of Chemical Physics*, 83:4877–4905, 1985.

[126] R. Tycko. Zero field nuclear magnetic resonance in high field–the untruncation of dipole-dipole couplings by coherent averaging. *Physical Review Letters*, 60:2734, 1988.

[127] R. Tycko. Zero field nuclear magnetic resonance in high field. *The Journal of Chemical Physics*, 92(10):5776–5793, 1990.

[128] C. Hilbert, J. Clarke, T. Sleator, and E.L. Hahn. Nuclear quadrupole resonance detected at 30 MHz with a dc superconducting quantum interference device. *Applied Physics Letters*, 47(6):637–639, 1985.

[129] J. Chang, C. Connor, E.L. Hahn, H. Huber, and A. Pines. Direct detection of Al-27 resonance with a SQUID spectrometer. *Journal of Magnetic Resonance*, 82(2):387–391, Apr 1989.

[130] C. Connor, J. Chang, and A. Pines. Aluminum and boron nuclear quadrupole resonance with a direct current superconducting quantum interference device. *The Journal of Chemical Physics*, 93(11):7679–7646, Dec 1990.

[131] C. Connor, J. Chang, and A. Pines. Magnetic resonance spectrometer with a dc SQUID detector. *Review of Scientific Instruments*, 61(3):1059–1063, 1990.

[132] N.Q. Fan and J. Clarke. Low-frequency nuclear magnetic resonance and nuclear quadrupole resonance spectrometer based on a dc superconducting quantum interference device. *Review of Scientific Instruments*, 62(6):1453–1459, Jun 1991.

[133] M.D. Hurlimann, C.H. Pennington, N.Q. Fan, J. Clarke, A. Pines, and E.L. Hahn. Pulse fourier-transform NQR of ^{14}N with a dc SQUID. *Physical Review Letters*, 69(4), Jul 1992.

[134] B. Black. *Methyl Quantum Tunneling and Nitrogen-14 NQR NMR Studies Using a SQUID Magnetic Resonance Spectrometer.* PhD thesis, University of California, Berkeley, 1993.

[135] U. Werner, B. Black, M. Ziegeweid, and A. Pines. SQUID-NQR of nitrogen-14 in amino acids and small peptides. *Chemical Physics Letters*, 209(1–2):17–21, 1993.

[136] U. Werner-Zwanziger, M. Ziegeweid, B. Black, and A. Pines. Nitrogen-14 SQUID NQR of l-ala-l-his and of serine. *Zeitschrift fur Naturforschung Section A–A Journal of Physical Sciences*, 49(12):1188–1192, 1994.

[137] J.P. Yesinowski, M.L. Buess, A.N. Garroway, M. Ziegeweid, and A. Pines.

Detection of N-14 and Cl-35 in cocaine base and hydrochloride using NQR. *Analytical Chemistry*, 67(13):2256–2263, 1995.

[138] D.M. TonThat and J. Clarke. Direct current superconducting quantum interference device spectrometer for pulsed nuclear magnetic resonance and nuclear quadrupole resonance at frequencies up to 5 MHz. *Review of Scientific Instruments*, 67(8):2890–2893, Aug 1996.

[139] M.P. Augustine, D.M. TonThat, and J. Clarke. SQUID detected NMR and NQR. *Solid State Nuclear Magnetic Resonance*, 11:139–156, 1998.

[140] H.C. Seton, D.M. Bussell, J.M.S. Hutchison, I. Nicholson, and D.J. Lurie. DC SQUID-based NMR detection from room-temperature samples. *Physics in Medicine and Biology*, 37(11):2133–2138, Nov 1992.

[141] S. Kumar, B.D. Thorson, and W.F. Avrin. Broad-band SQUID NMR with room-temperature samples. *Journal of Magnetic Resonance*, 107(3):252–259, Jun 1995.

[142] S. Kumar, W.F. Avrin, and B.R. Whitecotton. NMR of room temperature samples with a flux-locked dc SQUID. *IEEE Transactions on Magnetics*, 32(6):5261–5264, Nov 1996.

[143] S. Kumar, R. Matthews, S.G. Haupt, D.K. Lathrop, M. Takigawa, J.R. Rozen, S.L. Brown, and R.H. Koch. Nuclear magnetic resonance using a high temperature superconducting quantum interference device. *Applied Physics Letters*, 70(8):1037–1039, Feb 1997.

[144] K. Schlenga, R.F. McDermott, J. Clarke, R.E. de Souza, A. Wong-Foy, and A. Pines. High T_c squids for low-field NMR and MRI of room temperature samples. In *IEEE Transactions on Applied Superconductivity*, volume 9 of *Part 3*, pages 4424–4427, Jun 1999.

[145] R.E. de Souza, K. Schlenga, A. Wong-Foy, R. McDermott, A. Pines, and J. Clarke. NMR and MRI obtained with high transition temperature dc

SQUIDs. *Journal of the Brazilian Chemical Society*, 10(4):307–312, Jul–Aug 1999.

[146] K. Schlenga, R.F. McDermott, J. Clarke, R.E. de Souza, A. Wong-Foy, and A. Pines. Low-field magnetic resonance imaging with a high-T_c dc superconducting quantum interference device. *Applied Physics Letters*, 75(23):3695–3697, Dec 1999.

[147] A. Wong-Foy, S. Saxena, A.J. Moulé, H.L. Bitter, J.A. Seeley, J. Clarke, and A. Pines. Hyperpolarized ^{129}Xe NMR and MRI at ultra low fields. *to be submitted*, 2001.

[148] S. Saxena, A. Wong-Foy, A.J. Moulé, J.A. Seeley, R.F. McDermott, J. Clarke, and A. Pines. Resolution of xenon-129 chemical shifts at ultralow magnetic fields. *to be submitted*, 2001.

[149] T.S. Lee, E. Dantsker, and J. Clarke. High-transition temperature superconducting quantum interference device microscope. *Review of Scientific Instruments*, 67(12):4208–4215, Dec 1996.

[150] D. Drung and H. Koch. An integrated dc SQUID magnetometer with variable additional positive feedback. *Superconducting Science Technology*, 7:242–245, 1994.

[151] D. Drung, E. Dantsker, F. Ludwig, H. Koch, R. Kleiner, J. Clarke, S. Krey, D. Reimer, B. David, and O. Doessel. Low noise $YBa_2Cu_3O_{7-x}$ SQUID magnetometers operated with additional feedback. *Applied Physics Letters*, 68(13):1856–1858, Mar 1996.

[152] M. Packard and R. Varian. Free nuclear induction in the Earth's magnetic field. *Physical Review*, 93(4):941, 1954.

[153] A.K. Jain. *Fundamentals of Digital Image Processing.* Prentice Hall information and systems sciences series. Prentice Hall, Englewood Cliffs, NJ, 1989.

[154] B. Driehuys, G.D. Cates, E. Miron, K. Sauer, D.K. Walter, and W. Happer. High-volume production of laser-polarized Xe-129. *Applied Physics Letters*, 69(12):1668–1670, Sep 1996.

[155] M. Haake, A. Pines, J.A. Reimer, and R. Seydoux. Surface-enhanced NMR using continuous-flow laser-polarized xenon. *Journal of the American Chemical Society*, 119(48):11711–11712, Dec 1997.

[156] E. Brunner, R. Seydoux, M. Haake, A. Pines, and J.A. Reimer. Surface NMR using laser-polarized Xe-129 under magic angle spinning condition. *Journal of Magnetic Resonance*, 130:145–148, 1998.

[157] R. Seydoux, A. Pines, M. Haake, and J.A. Reimer. NMR with a continuously circulating flow of laser-polarized Xe-129. *Journal of Physical Chemistry B*, 103(22):4629–4637, 1999.

[158] E. Brunner, M. Haake, L. Kaiser, A. Pines, and J.A. Reimer. Gas flow MRI using circulating laser-polarized xenon-129. *Journal of Magnetic Resonance*, 138:155–159, 1999.

[159] L.G. Kaiser, T. Meersmann, J.W. Logan, and A. Pines. Visualization of gas flow and diffusion in porous media. *Proceedings of the National Academy of Sciences of the United States of America*, 97(6):2414–2418, 2000.

[160] Y.S. Greenberg. Application of superconducting quantum interference devices to nuclear magnetic resonance. *Reviews of Modern Physics*, 70(1):175–222, Jan 1998.

[161] A.W. Overhauser. Paramagnetic relaxation in metals. *Physical Review*, 89(4):689–700, 1953.

[162] A. Abragam. Overhauser effect in nonmetals. *Pysical Review*, 98(6):1729–1735, 1955.

[163] G. Planinsic, T. Guiberteau, and D. Grucker. Dynamic nuclear polarization imaging in very low magnetic fields. *Journal of Magnetic Resonance, Series B*, 110(2):205–209, 1996.

Appendix A

Ancillary Figures

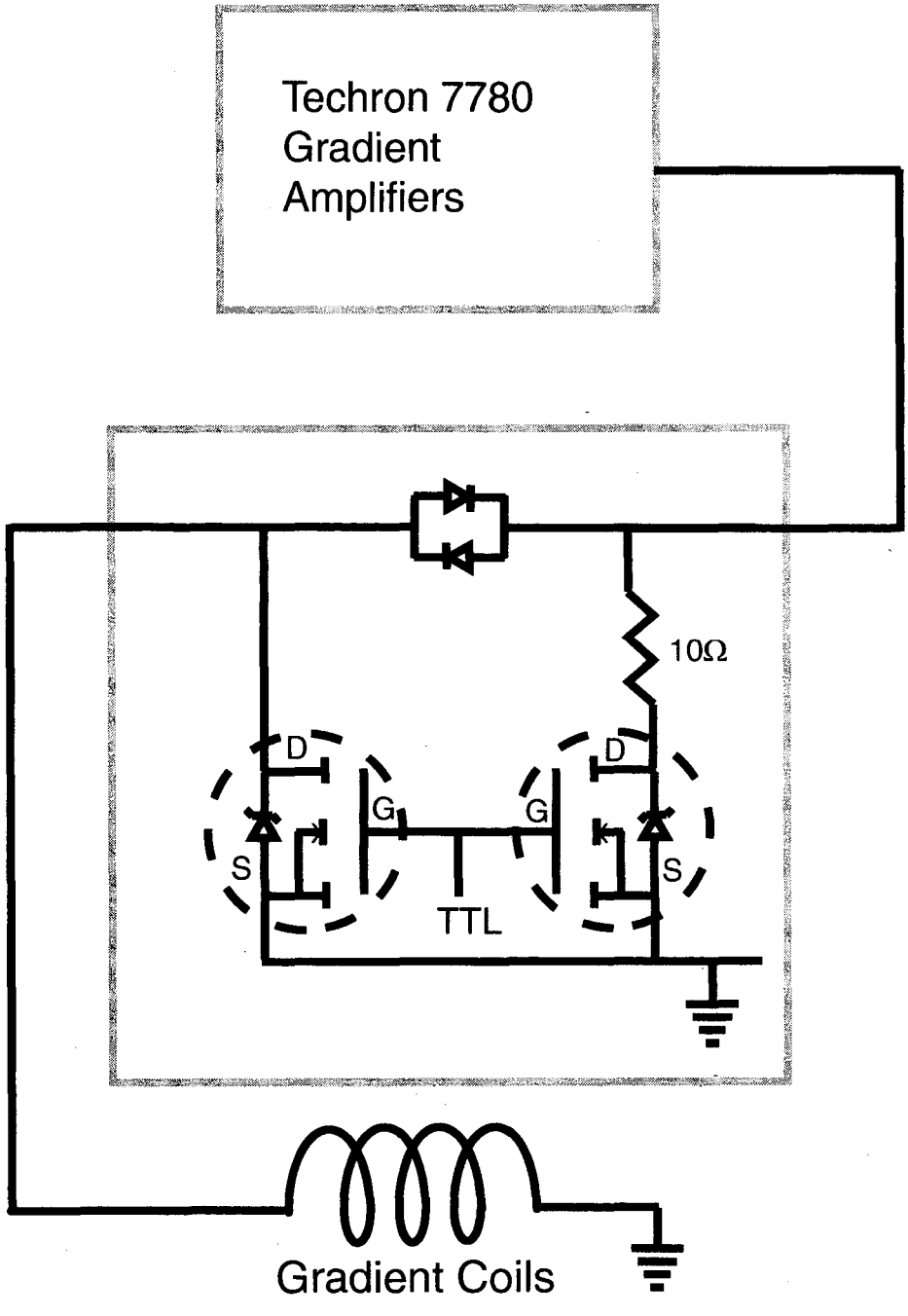

Figure A.1. Gradient Amplifier Blanking Circuit

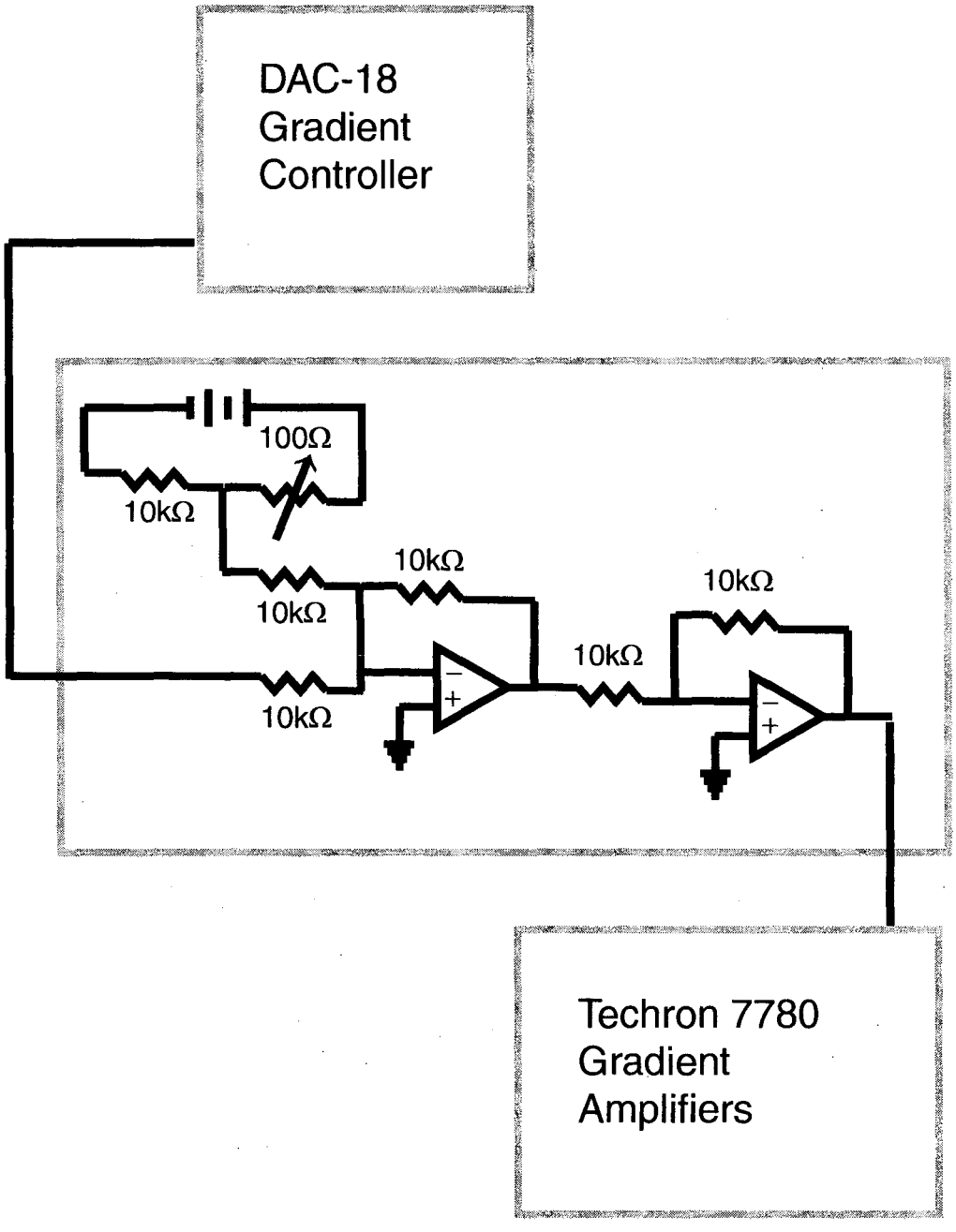

Figure A.2. Unity gain adding amplifiers for gradient controller offset.

Ernest Orlando Lawrence Berkeley National Laboratory
One Cyclotron Road | Berkeley, California 94720

Prepared for the U.S. Department of Energy under Contract No. DE-AC03-76SF00098